UNIVERSITY OF CALIFORNIA, SAN DIEGO

Radar Remote Sensing of the Lower Atmosphere

A dissertation submitted in partial satisfaction of the
requirements for the degree
Doctor of Philosophy

in

Electrical Engineering
(Signal and Image Processing)

by

Ali Karimian

Committee in charge:

William S. Hodgkiss, Chair
William A. Coles
Peter Gerstoft
Robert Hecht-Nielsen
William Kuperman
Bhaskar Rao
Caglar Yardim

2012

The dissertation of Ali Karimian is approved, and it is acceptable in quality and form for publication on microfilm and electronically:

Chair

University of California, San Diego

2012

DEDICATION

To maman Roya and baba Farid. They have had a hard life, but made everything easy for us. I always want to make them proud.

To Tina, my wife, who is a perfect combination of love and ambition.

To Floria, Tina's mom, whose memory will always stay with us.

TABLE OF CONTENTS

Signature Page iii

Dedication iv

Table of Contents v

List of Figures vii

Acknowledgements xii

Vita and Publications xiii

Vita xiii

Abstract of the Dissertation xiv

Chapter 1 Introduction 1

Chapter 2 Refractivity Estimation from Sea Clutter: An invited Review . . . 7
- 2.1 Introduction 7
- 2.2 Marine ducts 11
  - 2.2.1 Evaporation ducts 12
  - 2.2.2 Surface-based ducts 13
  - 2.2.3 Elevated ducts 15
- 2.3 Electromagnetic theory and forward modeling 17
  - 2.3.1 Wave propagation modeling 18
  - 2.3.2 Sea surface reflectivity models 24
- 2.4 Inverse problem framework 26
  - 2.4.1 Likelihood function 27
  - 2.4.2 An inversion example 29
  - 2.4.3 Bayesian approach 31
  - 2.4.4 Alternative RFC formulations 35
- 2.5 Conclusion and future directions 36

Chapter 3 Multiple Grazing Angle Sea Clutter Modeling 38
- 3.1 Introduction 38
- 3.2 sea clutter at low grazing angles 40
  - 3.2.1 Modified GIT model 40
- 3.3 Angular spectral estimation 41
  - 3.3.1 Wentzel-Kramers-Brillouin-Jeffreys approximation to wave propagation 43
  - 3.3.2 Curved wave spectral estimation 45

3.3.3 Plane wave spectral estimation 47
3.4 Multiple Grazing Angle Clutter 50
3.5 Examples 52
3.5.1 Evaporation Ducts 53
3.5.2 Surface-Based Ducts 54
3.5.3 SPANDAR 1998 Measured Refractivity 57
3.6 Conclusion 57

Chapter 4 Estimation of radio refractivity using a multiple angle clutter model 62
4.1 Introduction 62
4.2 Sea clutter at low grazing angles 63
4.2.1 Grazing angle independent clutter model 64
4.2.2 Range-dependent single grazing angle clutter 64
4.2.3 Range-dependent multiple grazing angle clutter . . . 65
4.3 Performance analysis for RFC estimation 71
4.3.1 Surface-based ducts 71
4.3.2 Range-dependent evaporation duct 73
4.3.3 SPANDAR 1998 dataset 75
4.4 Conclusion 77

Chapter 5 Towards assimilation of atmospheric surface layer using weather prediction and radar clutter observations 80
5.1 Introduction 80
5.2 Dependence of refractivity index on atmospheric parameters 82
5.3 Refractivity from clutter 85
5.3.1 Sea clutter model 85
5.3.2 Refractivity profile inversion and bulk-parameters for evaporation ducts 86
5.4 Numerical weather prediction 90
5.5 Integration of radar observations and weather prediction . . 93
5.6 Conclusion 100

Chapter 6 Conclusion and Future Research 103

LIST OF FIGURES

Figure 1.1: Propagation diagram of a (a) weak evaporation duct, (b) surface-based duct (high intensity: bright). Radar PPI screen showing clutter map (dB) during the 1998 SPANDAR experiment resulting from a (c) weak evaporation duct, (d) surface-based duct. 2

Figure 2.1: Propagation diagram of a (a) weak evaporation duct, (b) surface-based duct (high intensity: bright). Radar PPI screen showing clutter map (dB) during the 1998 SPANDAR experiment resulting from a (c) weak evaporation duct, (d) surface-based duct. 9

Figure 2.2: Parameters of simplified duct geometries: (a) evaporation duct, (b) surface-based duct, (c) surface-based duct with an evaporation layer, and (d) elevated duct. 12

Figure 2.3: (a) A measured profile from the 1998 SPANDAR and its trilinear approximation. (b) propagation loss (dB) of the measured profile at 3 GHz. Propagation loss difference of the measured profile and the trilinear approximation at (c) 3 GHz, (d) 10 GHz. Clutter power comparison of the profile and its trilinear approximation at (e) 3 GHz, (f) 10 GHz. 16

Figure 2.4: (a) Refractivity profile of surface-based duct used for (b) determination of grazing angles by ray trace (solid) and final maximum angles (dashed lines) used for computing $\alpha_{h,v}$. 23

Figure 2.5: Reflectivity vs. grazing angle for several sea surface reflectivity models at (a) 3 GHz, and (b) 9.3 GHz. 25

Figure 2.6: (a) Range-dependent refractivity profile recorded by an instrumented helicopter along the $150°$ azimuth. (b) Average of the first 45 km of the measured profile compared to the inverted profiles of $150°$ clutter (solid) and the MAP profile of 142–166° (shaded). (c) observed and modeled clutter power of the inverted profile. 30

Figure 2.7: Propagation loss: (a) MAP estimate of the refractivity profile given the clutter power at 150° azimuth of SPANDAR Run 07, and (b) standard atmosphere. 31

Figure 2.8: Posterior probability distribution of the propagation loss at range 60 km and altitudes of (a) 28 m, and (b) 180 m above the mean sea level, from the inversion of Fig. 2.6. (c) Detection probability given an isotropic target with an RCS of 1 m^2. 34

Figure 3.1: The sensitivity of GIT reflectivity per unit area $\sigma_{0,GIT}$ to grazing angle and wind speed at 3 GHz for horizontal (solid) and vertical (dashed) polarization. 42

Figure 3.2: (a) Power $|u|^2$ (dB) from PE in an arbitrary surface-based duct. (b,c) Geometry of the line array used for the estimation of grazing angles at each range for plane and curved wave spectral estimation. (d) The spatial transfer function of a 200 element Hamming window with inter-element spacing of 5.7λ. (e) Normalized angular power spectrum $|B_{\text{CWS},1}(\theta)|^2$ for an arbitrary range (65 km) of Panel (a). 46

Figure 3.3: Angular power spectrum for a 24 m evaporation duct, antenna height of 25 m at 10 GHz, using: (a) plane wave spectral estimation $|B_{\text{PWS},1}|^2$ (3.21), (b) curved wave spectral estimation $|B_{\text{CWS},1}|^2$ (3.19), (c) $|B_{\text{PWS},2}|^2$ (3.22), (d) $|B_{\text{CWS},2}|^2$ (3.20). Dashed lines are grazing angles obtained from the ray theory. Higher angular resolution is obtained when both incident and reflected wavefronts are considered. In each case, the angular power spectrum is normalized by the maximum power over the whole range. 49

Figure 3.4: Grazing angle computed by ray tracing, MUSIC, PWS and CWS for an evaporation duct with duct height of 24 m and antenna height of 25 m at (a) 3 GHz, (b) 10 GHz. The synthetic aperture is 20 m for all cases. 50

Figure 3.5: (a) M-profile of an evaporation duct with $h_d = 24$ m. (b) Propagation factor F in dB for 10 GHz. (c) Output power of CWS normalized by the maximum power over the whole range, compared to the grazing angle computed by ray tracing (solid). (d) Clutter power calculated by maximum ray tracing and the multiple grazing angle model (CWS, PWS). 54

Figure 3.6: (a) M-profile of a surface-based duct. (b) Propagation factor F in dB for 10 GHz. (c) CWS output power normalized by the maximum power over the whole range, overlaid with grazing angles obtained from ray tracing (solid). (d) Clutter power from maximum ray tracing and the multiple grazing angle model. 56

Figure 3.7: Discontinuity in clutter power when grazing angle is obtained from ray tracing. Similar refractivity profile and conditions as in Fig. 3.6 except that antenna height and frequency are 45 m and 3 GHz. (a) CWS output power normalized by the maximum power over the whole range, overlaid with grazing angle obtained from ray tracing (solid). (b) Multiple angle clutter power based on CWS and single angle clutter based on ray tracing. 57

Figure 3.8: (a) M-profile of a surface-based duct. (b) Propagation factor F in dB for 10 GHz. (c) CWS output power normalized by the maximum power over the whole range, overlaid with grazing angles obtained from ray tracing (solid) and maximum of ray traces (dashed). (d) Clutter power from maximum ray tracing and the multiple grazing angle model based on CWS. 58

Figure 3.9: (a) M-profile measured during the SPANDAR 1998 experiment. (b) Propagation factor F in dB for 3 GHz. (c) CWS output power normalized by the maximum power over the whole range, overlaid with grazing angles obtained from ray tracing (dark line). (d) Clutter power from maximum ray tracing and the multiple grazing angle model. 59

Figure 4.1: (a) Power $|u|^2$ (dB) from the parabolic equation (PE) propagation model in an arbitrary surface-based duct similar to the profile of Fig. 4.2c. (b) Geometry of the line array used for the estimation of grazing angles at each range for curved wave spectral estimation. (c) Angular spectral power (contour plot), grazing angle from ray tracing (solid), the maximum angle from ray tracing (dashed). . . . 67

Figure 4.2: Left panels: refractivity profile, right panels: corresponding clutter power at 3 GHz using various clutter models: multiple grazing angle, angle independent, and maximum angle from ray tracing. . . 70

Figure 4.3: Inverted surface based duct parameters using various clutter models: (a) multiple angle, (b) maximum angle from ray tracing, and (c) angle-independent. The simulated clutter power is modeled by the multi angle clutter model and include random components of the sea surface reflectivity and noise floor in the receiver. Vertical lines are the actual parameters of this synthetic example. 72

Figure 4.4: (a) Propagation factor (dB) corresponding to the refractivity profile in Fig. 4.2c. (b-d): The difference between the propagation factors of the original profile and inversion of noisy signals using multiple angle, maximum angle from ray tracing, and angle-independent clutter models respectively. The color scale is identical in (b-d). Profile parameters are obtained from the distribution peaks in Fig. 4.3. 74

Figure 4.5: Inverted range-dependent evaporation duct height parameters using clutter models: (a) multiple angle and (b) angle-independent. Vertical lines denote the actual parameters of this synthetic example. . . 75

Figure 4.6: Histograms of estimated trilinear function parameters for the SPANDAR dataset, Run 07, along azimuth 145–155°. The peaks of parameter distribution (solid lines) are used in Fig. 4.7. Inversions use different clutter models: (a) multiple angle, (b) maximum angle from ray tracing, (c) angle-independent. Dashed lines show inverted parameters only using the clutter at 150°. 77

Figure 4.7: (a) Refractivity profile along the 150° azimuthal line. (b) Average of the first 55 km of measured refractivity profiles compared to the estimated profiles from RFC. Trilinear function parameters are obtained from Fig. 4.6. (c) Observed clutter at 150° azimuth and modeled clutters based on inverted profiles. The shaded area shows the variation of clutter power between 145–155° used in RFC. 78

Figure 5.1: The modified refractivity profile of an arbitrary evaporation duct with $\Delta T = 0$ and duct height $h_d = 24$ m. 83

Figure 5.2: Evaporation duct height versus $\Delta T = T_{12} - T_{12}$ and relative humidity (RH) for wind-speed (u) of 5 m/s and 10 m/s, obtained by NAVSLaM. All atmospheric variables are referenced at 10 m above the sea surface. $T_{12} = 15°$C in (a,c) and $T_{12} = 30°$C in (b,d). . . . 84

Figure 5.3: (a) Modified refractivity profiles, all with duct height of 14 m. The corresponding clutter powers when the radar is located at 10 m, for operational frequencies of (b) 3 GHz, and (c) 10 GHz. $T_{12} = 30°C$, and $u = 5$ m/s. 88

Figure 5.4: (a,c): Modified refractivity profiles, (b,d): Corresponding clutter powers. Radar frequency is 3 GHz and located at 10 m above the sea-surface. $T_{12} = 15°C$, and $u = 5$ m/s. (a,b): $RH = 70\%$, different ΔT conditions. (c,b): $\Delta T = 1°C$, different humidities. . 89

Figure 5.5: Average values (top row) and standard deviation (bottom row) of COAMPS ensemble of wind-speed, air-sea/ground temperature difference and relative humidity at 10 m around the Hawaii Islands for May 7, 2008 at 12 am UTC using 5 km grid spacings. The last column is the observed surface temperature (sea or ground surface) during the same time using buoy and ship data. 91

Figure 5.6: (a) Average and (b) standard deviation of duct heights obtained by running NAVSLaM on the COAMPS ensemble in Fig. 5.5. The geographic locations of cases analyzed in Figs. 5.7–5.9 are marked with white (x). 92

Figure 5.7: Case 1, $\Delta T < 0$ corresponding to 12 am UTC May 7, 2008 at [120, 330] km in Fig. 5.5, (a–c): Scatter plots of ΔT and RH, and their marginal densities obtained by (a) COAMPS ensemble, (b) RFC-ED, (c) joint NWP, RFC-ED. The NWP ensemble mean (□) is used for clutter power simulations. (d): Histogram of duct heights obtained by RFC-ED in (b). 95

Figure 5.8: Case 2, $\Delta T = 0$ corresponding to 3 am UTC July 27, 2008 at [415, 340] km in Fig. 5.5, (a–c): Scatter plots of ΔT and RH, and their marginal densities obtained by (a) COAMPS ensembles, (b) RFC-ED, (c) joint NWP, RFC-ED. The NWP ensemble mean (□) is used for clutter power simulations. (d): Histogram of duct heights obtained by RFC-ED in (b). 96

Figure 5.9: Case 3, $\Delta T > 0$ corresponding to 12 am UTC July 28, 2008 at [150, 450] km in Fig. 5.5, (a–c): Scatter plots of ΔT and RH, and their marginal densities obtained by (a) COAMPS ensembles, (b) RFC-ED, (c) joint NWP, RFC-ED. The NWP ensemble mean (□) is used for clutter power simulations. (d): Histogram of duct heights obtained by RFC-ED in (b). 97

Figure 5.10: Case 4, evolution of the environment after predictions, (a–c): Scatter plots of ΔT and RH, and their marginal densities obtained by (a) COAMPS from Fig. 5.8, (b) RFC-ED, (c) joint NWP, RFC-ED. The square shows the assumed true state used for clutter power simulations, (d): Histogram of duct heights obtained by RFC-ED in (b). 98
Figure 5.11: Duct height (m) as a function of ΔT and RH with $T_{12} = 26°C$ and $u = 8$ m/s, conditions similar to average ensemble in Fig. 5.5. Scattered symbols show inversion results obtained by RFC-ED. Cases 1–4 refer to Figs. 5.7–5.10, respectively. 99
Figure 5.12: The distribution of propagation factor F using NWP, RFC-ED and joint NWP RFC-ED at heights of 10 m and 40 m and range of 25 km from an assumed source. The vertical axis is the empirical probability. (a,b): The example in Fig. 5.7 with $\Delta T < 0$, (c,d): the example in Fig. 5.8 with $\Delta T = 0$, (e,f): the example in Fig. 5.9 with $\Delta T > 0$, (g,h): the biased example in Fig. 5.10. 101

ACKNOWLEDGEMENTS

I would like to thank my advisors Professors William Hodgkiss, Peter Gerstoft, and Caglar Yardim for their invaluable guidance and support in many ways during the past three years. I have many good memories from Peter and his lovely wife Karen, office discussions with Caglar that entailed all possible global issues, and Bill's support of all my decisions. I am also thankful to my thesis committee members Professor William Coles, Professor Robert Hecht-Nielsen, Professor Bhaskar Rao and Professor William Kuperman for being wonderful mentors and supporters. Robert Hecht-Nielsen made me courageous again with his confidence and super positive attitude. Especially I feel blessed by having a really supportive and understanding family. My mother, father, sister, and wife. I love them all.

The contents of Chapter 2 were first published in the Journal of Radio Science as: A. Karimian, C. Yardim, P. Gerstoft, W. .S. Hodgkiss, Amalia Barrios , "Refractivity Estimation from Sea Clutter: An invited Review", *Radio Sci.*, 46, RS6013, 2011. Contents of Chapter 3 were published as: A. Karimian, C. Yardim, P. Gerstoft, W. .S. Hodgkiss, Amalia Barrios, "Multiple grazing angle sea clutter modeling", *IEEE Trans. Antennas Propagat.*, vol. 60, no. 90, pp. 4408-4417, September 2012. Chapter 4 was previously published as: A. Karimian, C. Yardim, P. Gerstoft, W. .S. Hodgkiss, Amalia Barrios, "Estimation of refractivity using a multiple angle clutter model", *Radio Sci.*, 47, RS0M07, 2012. Chapter 5 is submitted to *J. Appl. Meteorol.* as: A. Karimian, C. Yardim, T. Haack, P. Gerstoft, W. .S. Hodgkiss, Ted Rogers, "Towards assimilation of atmospheric surface layer using weather prediction and radar clutter observations".

VITA

2007	B.S. in Electrical Engineering, Sharif University of Technology
2009	M.S. in Electrical Engineering (Signal and Image Processing), University of California, San Diego
2012	Ph.D. in Electrical Engineering (Signal and Image Processing), University of California, San Diego

PUBLICATIONS

A. Karimian, C. Yardim, P. Gerstoft, W. .S. Hodgkiss, Amalia Barrios , "Refractivity Estimation from Sea Clutter: An invited Review", *Radio Sci.*, 46, RS6013, 2011.

A. Karimian, C. Yardim, P. Gerstoft, W. .S. Hodgkiss, Amalia Barrios, "Multiple grazing angle sea clutter modeling", *IEEE Trans. Antennas Propagat.*, vol. 60, no. 90, pp. 4408-4417, 2012.

A. Karimian, C. Yardim, P. Gerstoft, W. .S. Hodgkiss, Amalia Barrios, "Estimation of refractivity using a multiple angle clutter model", *Radio Sci.*, 47, RS0M07, 2012.

A. Karimian, C. Yardim, T. Haack, P. Gerstoft, W. .S. Hodgkiss, Ted Rogers,"Towards assimilation of atmospheric surface layer using weather prediction and radar clutter observations", submitted to *J. Appl. Meteorol.*

ABSTRACT OF THE DISSERTATION

Radar Remote Sensing of the Lower Atmosphere

by

Ali Karimian

Doctor of Philosophy in Electrical Engineering
(Signal and Image Processing)

University of California, San Diego, 2012

William S. Hodgkiss, Chair

Non-standard radio wave propagation in the atmosphere is caused by anomalous changes of the atmospheric refractivity index. These changes, if not accounted for, can cause major problems in detection of the location of flying targets. Direct sensing of the atmospheric refractivity index by measuring humidity and temperature has been the common practice in past. Refractivity from clutter (RFC) was developed in recent years to complement traditional ways of measuring the refractivity profile in maritime environments. The ability to track the refractivity profile in time and space, together with a lower cost and convenience of operations have been the promising factors that brought RFC under consideration. Presented is an overview of the basic concepts, research and achievements in the field of RFC. A multiple angle clutter model is presented that is constructed by angular spectral estimation on the propagating power. This model is shown to perform better than conventional clutter models in remote sensing applications. Examples are either based on synthetically generated radar clutters or a set of S-band radar measurements from Wallops Island, 1998. Finally, an approach for fusing RFC output with evaporation duct characterization based on ensemble forecasts from a numerical weather prediction (NWP) model is examined. Relative humidity at a reference height and air-sea temperature difference (ASTD) are identified as state variables. Probability densities of atmospheric parameters and propagation factors obtained from an NWP ensemble, RFC, and joint inversions are compared. It is demonstrated that characterization of the near surface atmosphere by combining RFC and NWP reduces the estimation uncertainty of the refractivity index structure in an evaporation duct, with respect to using either method alone. Topics that require more attention in future studies also are discussed at the end.

Chapter 1

Introduction

Non-standard radio wave propagation in the atmosphere is caused by anomalous changes of the atmospheric refractivity index. Variations in the vertical refractivity profile can result in entrapment of electromagnetic waves, creating lower atmospheric ducts. Ocean ducting is a common phenomenon in hot and humid areas of the world that result in significant variations in the maximum operational radar range, creation of radar fades where the radar performance is reduced, and increased sea clutter [1]. Knowledge of the refractivity structure enables radar operators to compensate for non-standard atmospheric effects, or at least be aware of the radar limitations in specific locations.

Atmospheric pressure, temperature and humidity affect the refractivity structure, and thus affect radar propagation conditions. The vertical modified refractivity M is defined as the part per million deviation of the index of refraction n from that of a vacuum after transforming the spherical earth propagation into a flat earth problem. Modified refractivity is a function of atmospheric variables with experimental constants for frequencies 0.1–100 GHz [2,3]:

$$\begin{aligned} M(z) &= \frac{77.6P(z)}{T_{\text{air}}(z)} - \frac{5.6e(z)}{T_{\text{air}}(z)} + 3.75 \times 10^5 \frac{e(z)}{T_{\text{air}}^2(z)} \\ &+ 0.1568z, \end{aligned} \tag{1.1}$$

where $P(z)$ and $e(z)$ are the atmospheric pressure and partial pressure of water vapor in (hPa), and $T_{\text{air}}(z)$ is the absolute air temperature (K), all at altitude z in meters. Monin-Obukhov (MO) similarity theory is widely accepted as the means to relate physical quantities and processes in the atmospheric surface layer (ASL) [4]. MO-based models

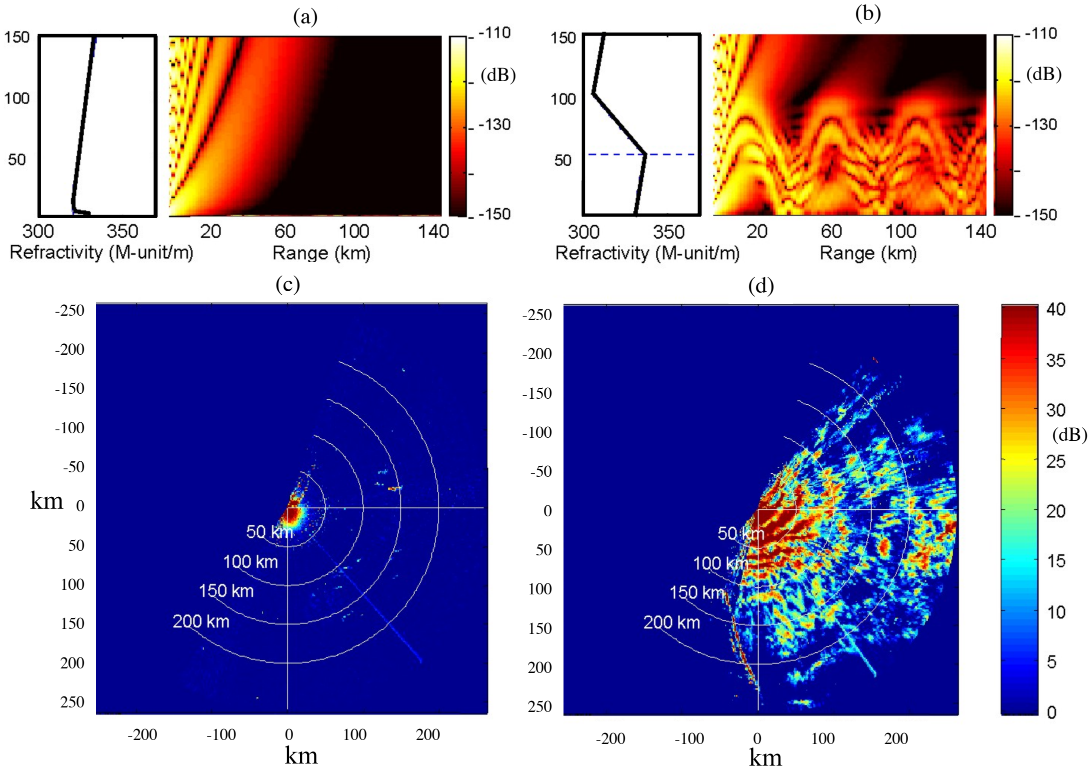

Figure 1.1: Propagation diagram of a (a) weak evaporation duct, (b) surface-based duct (high intensity: bright). Radar PPI screen showing clutter map (dB) during the 1998 SPANDAR experiment resulting from a (c) weak evaporation duct, (d) surface-based duct.

can generate vertical atmospheric profiles given the sea surface temperature (T_{sea}), and values at a reference height of air temperature, wind-speed (u), and relative humidity (RH). Corresponding vertical refractivity profiles subsequently can be obtained using (1.1). Examples of vertical modified refractivity profiles, radar propagation factors, and radar clutter power on the plan position indicator (PPI) screen are shown in Fig. 1.1. Strong surface ducts result in an increase in the interaction of radio waves with the sea-surface which in turn increases the radar clutter. More discussions on this figure are provided in Chapter 2.

Initial remote sensing studies in the radar [5,6] and climatology [7] communities have been directed toward a better estimation of the refractivity profile in the lower atmosphere, less than 100 m above the sea surface. UHF signal measurements have first been used to assess the base height of the trapping layer [8]. Ground-based measurements of global positioning system (GPS) signals subsequently have been used to infer the vertical refractivity profile of the lower atmosphere [9], followed by more recent studies [10,11].

Refractivity From Clutter (RFC) techniques estimate the lower atmospheric refractivity structure surrounding a radar using its sea surface reflected clutter signal. These techniques complement traditional ways of measuring the refractivity profile in maritime environments which rely on direct sensing of the environmental parameters. RFC can be described as a fusion of two disciplines [12–14]: numerical methods for efficient electromagnetic wave propagation modeling and estimation theory. The ability to track the refractivity profile of the ASL in time and space together with a lower cost and convenience of operations are advantages that RFC offers respective to the direct sensing of the atmosphere.

There has been strong correlation between the estimated refractivity profile using an S-band radar and *in situ* measurements by instrumented aircrafts [12,13]. RFC techniques enable the tracking of spatial and temporal changes in the environment [14,15]. There have been attempts to incorporate the worldwide surface meteorological observations database using the environmental library of advanced refractive effects prediction system (AREPS) [16] in the RFC inversion [17]. This method uses regional meteorological duct height statistics as a prior probability density in refractivity profile inversions.

This thesis mainly is a compilation of three papers that are published in the Journals of Radio Science and IEEE Transactions on Antennas and Propagation, and one paper that is submitted for a publication in the Journal of Applied Meteorology and Climatology.

Chapter 2 is a reprint of an invited paper in the Journal of Radio Science [18]. This chapter can serve as a full review of RFC research. The reader of this thesis is referred to this chapter for a comprehensive literature review of marine ducts (evaporation, surface-based and elevated ducts), the electromagnetic theory of wave propagation, sea-surface reflectivity models, and likelihood and Bayesian frameworks for refractivity profile inversion from radar clutter power. Some caveats of RFC techniques are discussed at the end. There has been suggested to incorporate numerical weather prediction (NWP) with RFC solutions to find the refractivity structure above the duct height, and to predict the presence of elevated ducts. This suggestion is later addressed for evaporation ducting conditions in [19], which is reprinted in Chapter 5.

RFC techniques require the clutter power to be as realistically modeled as possible. The occurrence of ducting conditions causes grazing angles to be range-dependent, as the electromagnetic wave is trapped inside the duct. It also might cause multiple grazing angles to be present at each range. The strong dependence of sea surface reflectivity on low grazing angles makes estimation of these angles important. Ray tracing is a common way of finding the grazing angle at the sea surface in the microwave region. However, it fails to account for shadow zones [20]. Hence, angular spectral estimation can be used to obtain the angle of arrival (AOA) as a function of range. Vertical arrays at each range can be generated synthetically with samples of the field obtained from a parabolic equation code [21,22].

The Advanced Propagation Model (APM) software [20] uses the maximum grazing angle obtained from ray tracing for propagation over the ocean, while plane wave spectral estimation (PWS) is used to calculate the dominant grazing angle over land. The Tropospheric electromagnetic parabolic equation routine (Temper) [23] uses the MUSIC algorithm [24] in its automatic mode to obtain the grazing angle when changes of the refractivity index are high. Temper uses ray tracing for evaporation ducts where MUSIC is not reliable. Switching between ray tracing and spectral estimation requires an ad hoc decision rule based on the gradient of the refractivity index along the array [25].

Chapter 3 is a reprint of a paper published in the IEEE Transactions on Antennas and Propagations [26]. A multiple grazing angle clutter model based on curved wave spectral estimation (CWS) is introduced there that incorporates all grazing angles at each range. CWS is a generalization of PWS where curvature of wavefronts due to changes in the refractivity index is considered. Examples demonstrate that the power versus grazing angle obtained by CWS is more accurate than PWS and it does not have the problem of discontinuity in grazing angles introduced by ray tracing.

Chapter 4 is a reprint of a paper published in the Journal of Radio Science [27]. The inversion performance of the multiple angle clutter model is compared to that of other models. Synthetic examples of a range-independent surface-based duct and a range-dependent evaporation duct are investigated for a S-band radar. Finally, a comparison of inversions on one set of experimental measurements from the SPANDAR 1998 dataset is provided, using single and multiple grazing angle clutter models, and the previously used model based on grazing angle independent sea surface reflectivity.

Weather radars and refractivity retrieval algorithms have been used to estimate moisture fields with high temporal and spatial resolution [28–30] with application in understanding thunderstorm initiation [31,32]. Sea clutter predictions based on range-varying ASL characterization from the Coupled Ocean and Atmospheric Mesoscale Prediction System (COAMPS) [33] were shown in [34] to be in agreement with clutter observed by a S-band radar in the lee of the Kauai Island. Mesoscale NWP has improved steadily over time and good agreements with observed ASL values have been reported [35,36].

Chapter 5 is a reprint of a paper that is submitted for publication in the Journal of Applied Meteorology and Climatology [19]. An approach for fusing RFC output under evaporation ducting conditions with an evaporation duct characterization based on ensemble forecasts from a mesoscale NWP model is examined. NWP and RFC can be used jointly in maritime environments to reduce the estimation variance of atmospheric variables near the sea surface. Advantage of NWP (providing prior information to a high altitude) and RFC (real-time tracking of atmospheric parameters) can be utilized jointly to provide a powerful inversion method. Our investigations have focused on RFC for evaporation ducts (RFC-ED) within the atmospheric surface layer. One drawback of RFC is the increased variance in the estimated refractivity above the atmospheric duct [37]. Above the duct, NWP potentially can regularize the RFC solution. On the other hand, RFC inversions potentially are able to reduce the NWP errors by increasing observations from RFC-capable ships.

The impacts of air sea temperature difference (ASTD) on the evaporation duct refractivity profile, atmospheric parameter inversion, and propagation factor distributions are studied. Relative humidity at a reference height and ASTD are identified as state variables in joint inversions that are based on NWP ensemble predictions and radar observations. Probability densities from an NWP ensemble, RFC-ED, and joint inversions are compared all compared. It is demonstrated that characterization of the near surface atmosphere by combining RFC-ED and NWP reduces the estimation uncertainty of ASTD, relative humidity, and subsequently the estimation uncertainty of the propagation factor in an evaporation duct, with respect to using either method alone. Our study opens the way for a full data assimilation framework that assimilates radar observations into NWP initial fields. This is further discussed in Chapter 6.

Chapter 2

Refractivity Estimation from Sea Clutter: An invited Review

2.1 Introduction

Refractivity From Clutter (RFC) techniques estimate the lower atmospheric refractivity structure surrounding a radar using its sea surface reflected clutter signal. The knowledge of the refractivity structure enables radar operators to compensate for non-standard atmospheric effects, or at least be aware of the radar limitations in specific locations. In the last decade, there has been interest in estimation of the environmental refractivity profile using the radar backscattered signals. RFC can be described as a fusion of two disciplines [12–14]: numerical methods for efficient electromagnetic wave propagation modeling and estimation theory.

Variations in the vertical refractivity profile can result in entrapment of the electromagnetic waves, creating lower atmospheric ducts. Ocean ducts are common phenomena that result in significant variations in the maximum operational radar range, creation of radar fades where the radar performance is reduced, and increased sea clutter [1]. Therefore, they greatly alter the target detection performance at low altitudes [38], and result in significant height error for 3–D radars.

RFC techniques find the profile associated with the best modeled clutter match to the observed clutter power. RFC has the advantage of temporal and spatial tracking of the refractivity profile in a dynamically changing environment.

Atmospheric pressure, temperature and humidity affect the refractivity structure, and thus affect the radar propagation conditions. The vertical gradient of the refractivity profile determines the curvature of radar rays [39]. Therefore, radar returns can be used to infer the gradient of refractivity structure near the ground [40].

Atmospheric ducts are more common in hot and humid regions of the world. The Persian Gulf, the Mediterranean and California coasts are examples of such regions with common formation of a ducting layer above the sea surface [17]. Surface based ducts appear on an annual average almost 25% of the time off the coast of South California and 50% in the Persian Gulf [41]. While surface-based ducts appear less common than evaporation ducts, their effect is more prominent on the radar return [1]. They often manifest themselves in a radar plan position indicator (PPI) as clutter rings, see Fig. 2.1d, or height errors in 3–D radars. The height error is due to the trapping of the lowest elevation beams near the surface instead of refracting upward as would be expected in a standard atmosphere.

Fig. 2.1b shows that a surface-based duct increases the radar range significantly inside the duct with respect to a weak evaporation duct (close to the standard atmosphere) by trapping the radar waves just above the ocean surface. Note that the electromagnetic energy is trapped inside the strong surface-based duct which results in an increase in the interaction of the electromagnetic waves with the sea surface. Fig. 2.1(c,d) demonstrates the effect of atmospheric ducts on the radar clutter. The strong ducting case has distinct clutter rings around the radar. This complex clutter structure enables RFC to estimate the atmospheric conditions from the radar returns.

There has been efforts to calculate sea reflections in ducting conditions to find the environmental refractivity profile from radar measurements, as opposed to the traditional way of using bulk sensor measurements [42,43]. The atmospheric refractivity profile is often measured by direct sensing of the environment. Rocketsondes and radiosondes typically are used for sampling of the atmospheric boundary layer [44], although they have limitations regarding mechanical issues and surface conditions [45,46]. For characterization of the surface layer, “bulk” parameters such as pressure, air and sea surface temperature, humidity, and wind speed are measured at a single height, usually with

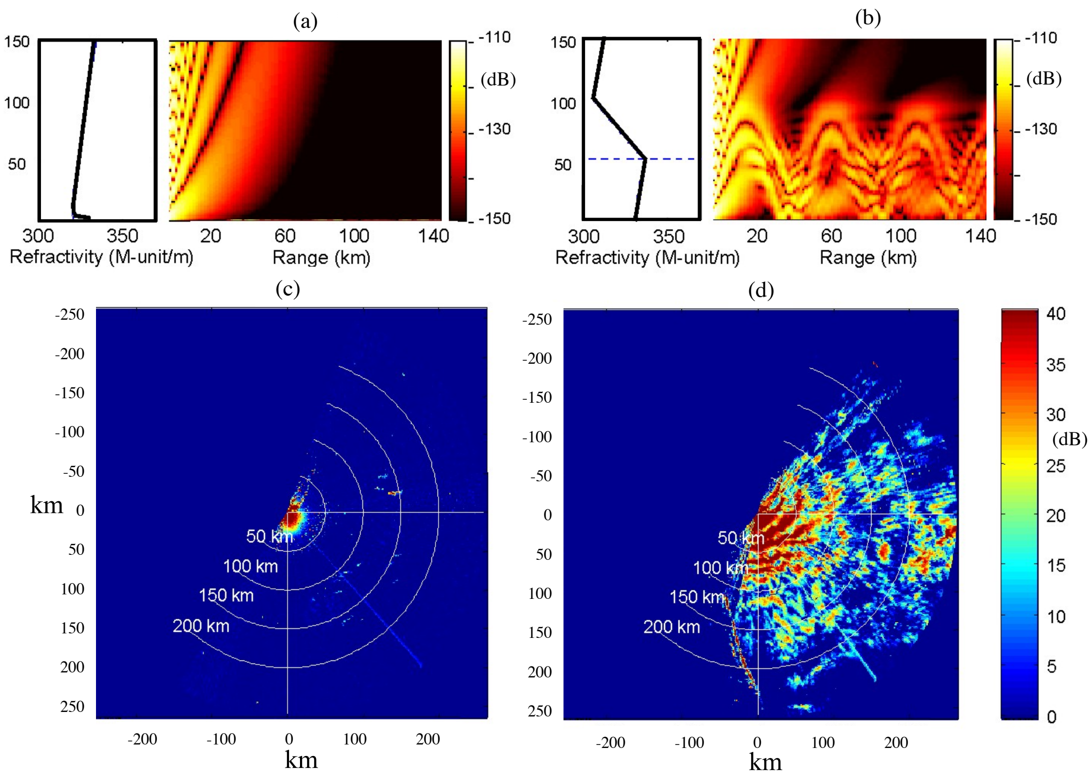

Figure 2.1: Propagation diagram of a (a) weak evaporation duct, (b) surface-based duct (high intensity: bright). Radar PPI screen showing clutter map (dB) during the 1998 SPANDAR experiment resulting from a (c) weak evaporation duct, (d) surface-based duct.

sensors placed on a buoy or platform on the sea surface. These in-situ measurements are then used as inputs to thermodynamic "bulk" models to estimate the near-surface vertical refractivity profile using Monin–Obukhov similarity theory [47–49].

Initial remote sensing studies in the radar [5,6] and climatology [7] communities have been directed toward a better estimation of the refractivity profile in the lower atmosphere, less than 500 m above the sea surface. Hitney demonstrated the capability to assess the base height of the trapping layer from measurements of UHF signal strengths [8]. Anderson inferred vertical refractivity of the lower atmosphere based on ground-based measurements of global positioning system (GPS) signals [9], followed by [10,11]. Estimation of refractivity structure from radio measurements with diversity in frequency and height have been examined in [50]. VHF/ UHF measurements from the VOCAR 1993 experiment have subsequently been used to invert for a three parameter (base height, M deficit and duct thickness) surface duct model [6]. A maximum a posteriori (MAP) approach for RFC inversions was developed by [51]. This work modeled the environment with a three element vector: two elements to describe the vertical structure and one to describe the range dependency of the profile. They later combined prior statistics of refractivity with point-to-point microwave propagation measurements to infer refractivity [52].

Other efforts in indirect sensing of the atmosphere include studies used GPS satellites and LIDARs. Low earth orbit GPS satellites have been used to analyze the occurrence frequency and variation of land and sea ducts on a global scale, during a 10 day period in May 2001 [53]. LIDAR [54,55] has also been used to measure the vertical refractivity profile. However, its performance is limited by the background noise (e.g. clouds) [14].

Weather radars and refractivity retrieval algorithms have been used to estimate moisture fields with high temporal and spatial resolution [28–30] with application in understanding thunderstorm initiation [31,32].

RFC techniques use the radar return signals to estimate the ambient environment refractivity profile. There has been strong correlation between the retrieved refractivity profile using an S-band radar and in-situ measurements by instrumented aircrafts or radiosondes [12,13,29]. RFC techniques make tracking of spatial and temporal changes in the environment possible [14,15,56]. RFC inversions of the environmental profile have been reported at frequencies as low as VHF [6], and as high as 5.6 GHz [57].

The development of RFC initially was inspired by the use of inverse methods in ocean acoustics which also is based on propagating signals in a waveguide. For a review of numerical modeling of the ocean waveguide see [58]. For an introduction to the ocean acoustic inverse problem see [59] and for sequential inverse methods in ocean acoustics see [60].

The remainder of this paper is organized as follows: Section 2.2 introduces the marine ducts and their simplified mathematical models. Section 2.3 summarizes the clutter models used in previous studies and wave propagation approximations that model radio wave propagation efficiently. Section 2.4 summarizes the RFC research and inversion methods that have been used to infer the environmental refractivity parameters. Section 2.5 discusses the shortcomings of the current research and areas that require more attention in the future.

2.2 Marine ducts

One of the first reports of abnormal performance of radar systems in maritime environments was during World War II where British radars on the northwest coast of India commonly observed the coast of the Arabian peninsula 2700 km apart under monsoon conditions [61]. Marine ducts are the result of heat transfer, moisture and the momentum of changes in the atmosphere [62] and entail three general classes: evaporation, surface-based and elevated ducts.

These ducts are characterized by a range and height dependent environmental refractivity index. Although a refractivity profile has a complex structure in nature, it can be approximated by a bilinear or trilinear function for surface-based ducts and by an exponential function for evaporation ducts in modeling wave propagation [13,63,64].

The simplified atmospheric duct geometries used in most RFC works are shown in Fig. 2.2. The modified refractive index M is defined as the part per million deviation of the refractive index from that of a vaccum:

$$M(z) \cdot 10^{-6} = n(z) - 1 + z/r_e, \tag{2.1}$$

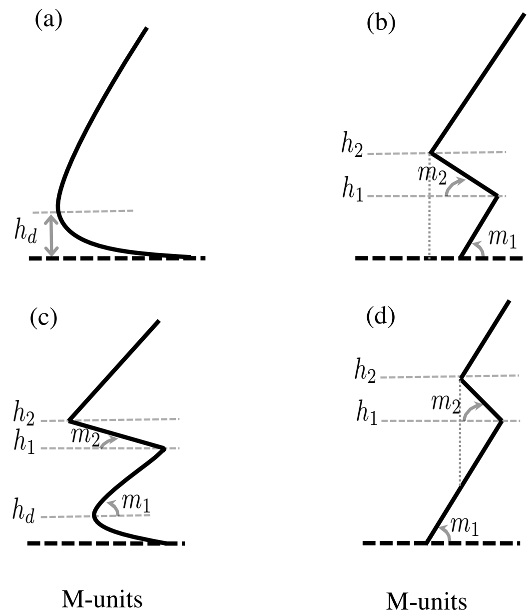

Figure 2.2: Parameters of simplified duct geometries: (a) evaporation duct, (b) surface-based duct, (c) surface-based duct with an evaporation layer, and (d) elevated duct.

which maps the refractivity index n at height z to a flattened earth approximation with earth radius $r_e = 6370$ km. The advantage of working with the modified refractive index is to transform a spherical propagation problem into a planar one. This transformation maps a spherically stratified medium over a spherical earth to a planar stratified medium above a flat earth. This transformation results in less than 1% error for ranges of less than $r_e/3$, independent of the wavelength [65]. However, this transformation to compute the height–gain function breaks down in centimeter wavelengths and elevation of more than 300 m. The error gets worse with increasing frequency [65].

2.2.1 Evaporation ducts

Katzin was the first to suggest the existence of evaporation ducts in 1947 [66]. Because of the difficulties in directly measuring the evaporation duct, various bulk models have been used to estimate the near-surface refractivity profile for several decades [47,67–69]. An evaporation duct model that assumes horizontally varying meteorological conditions has been suggested by [70]. Examples of such conditions are reported to frequently happen in the Persian Gulf [71]. One of the more widely accepted high fidelity evaporation duct models which has been used in various evaporation duct research studies is the model developed by the Naval Postgraduate School [72]. A 4-parameter model for range independent evaporation ducts that controls the duct height, M–deficit and slope has been suggested by [73].

The Paulus–Jeske (PJ) evaporation duct model is more commonly used operationally due to its empirical correction for spuriously stable conditions. The PJ model is based on the air and sea surface temperatures, relative humidity, wind speed with sensor heights at 6 m and the assumption of a constant surface atmospheric pressure [47,68,69]. For the neutral evaporation duct, where the empirical stability functions approach a constant, the PJ model is simplified to [12]:

$$M(z) = M_0 + c_0(z - h_d \ln \frac{z + z_0}{z_0}), \tag{2.2}$$

in which M_0 is the base refractivity, $c_0 = 0.13$ M-unit/m corresponding to the neutral refractivity profile as described by [74], z_0 is the roughness factor taken as 1.5×10^{-4} m, and h_d is the duct height. The exact choice of M_0 (usually taken in the interval [310–360] M-units/m) does not affect the propagation pattern since it is the derivative of M that dictates wave propagation in the medium [75,76].The assumption of neutral stability implies that the air and sea-surface temperature difference is nearly zero, and wind speed is no longer required. It was found in [77] that propagation estimates based on a neutral-stability bulk model performed well relative to other more sophisticated bulk models for the measurement sets under consideration. This is an important point as all RFC-estimated evaporation duct heights, and subsequently evaporation duct profiles given in (2.2), are based on neutral conditions.

2.2.2 Surface-based ducts

Surface ducts typically are due to the advection of warm and dry coastal air to the sea. The trilinear approximation of the M-profile, as shown in Fig. 2.2b, is represented by:

$$M(z) = M_0 + \begin{cases} m_1 z & z \leqslant h_1 \\ m_1 h_1 + m_2(z - h_1) & h_1 \leqslant z \leqslant h_2 \\ m_1 h_1 + m_2(h_2 - h_1) & h_2 \leqslant z \\ \ +m_3(z - h_1 - h_2) & \end{cases} \tag{2.3}$$

where $m_3 = 0.118\,$M-units/m, consistent with the mean over the United States. Since profiles are upward refracting, clutter power is not very sensitive to m_3 [13].

A surface duct, schematically shown in Fig. 2.2c, has also been used by [13,78], which includes an evaporation duct layer beneath the trapping layer:

$$M(z) = M_0 + \begin{cases} M_1 + c_0 \left(z - h_d \ln \frac{z+z_0}{z_0} \right) & z \leqslant z_d \\ m_1 z & z_d \leqslant z \leqslant h_1 \\ m_1 h_1 - M_d \frac{z-h_1}{z_{\text{thick}}} & h_1 \leqslant z \leqslant h_2 \\ m_1 h_1 - M_d + m_3(z - h_2) & h_2 \leqslant z \end{cases} \tag{2.4}$$

where $c_0 = 0.13$, m_1 is the slope in the mixed layer, $m_3 = 0.118\,$M-units/m, h_1 is the trapping layer base height, and z_d is the evaporation duct layer height determined by:

$$z_d = \begin{cases} \frac{h_d}{1-m_1/c_0} & 0 < \frac{1}{1-m_1/c_0} < 2 \\ 2h_d & \text{Otherwise} \end{cases} \tag{2.5}$$

subject to $z_d < h_1$. $h_1 = 0$ simplifies (2.4) to a bilinear profile and $h_2 = 0$ implies standard atmosphere. z_{thick} is the thickness of the inversion layer, and $h_2 = h_1 + z_{\text{thick}}$. M_1 is determined by $M_1 = c_0 h_d \ln \frac{z_d+z_0}{z_0} + z_d(m_1 - c_0)$, and M_d is the M-deficit of the inversion layer. Gerstoft *et. al.* used an 11 parameter model for the environmental refractivity profile [13]: five paremeters for the vertical structure as in (2.4), and six to model the range variations of the profile. They assumed that the trapping layer height h_2 is range dependent and used principle components of h_2 as a Markov process with respect to range.

Most of the RFC studies including [14,37,79] have used a four parameter surface based duct. However, the frequency range of the validity of a trilinear approximation to the surface duct refractivity structure is arguable. As Fig. 2.3 demonstrates, the trilinear approximation to complex refractivity profile structures gets worse for modeling wave propagation at higher frequencies. Propagation loss and clutter power of a measured profile and its trilinear approximation are shown in this figure.

The profile is from the SPANDAR 1998 dataset (Run 07, range 50 km) measured by an instrumented helicopter along the 150° azimuth shown in Fig. 2.1 [12]. Panel (a) shows the trilinear approximation obtained by minimizing the l_2 norm of the difference of the approximated and real profiles given that the slope of the third line is fixed and equal to 0.12 M-units/m. Panel (b) shows the propagation loss of the measured profile with antenna height of 25 m, frequency of 3 GHz, beamwidth of 0.4° and wind speed of 5 m/s. The propagation loss is obtained from the Advanced Propagation Model [20] which uses a parabolic equation code [80]. The clutter power is obtained from a multiple angle clutter model [26]. Panels (c) and (d) show that the error of the trilinear approximation for a complicated structure increases with frequency. Here, the average absolute error of the propagation loss inside the duct increases from 4.9 dB at 3 GHz to 6.7 dB at 10 GHz. The absolute value of the clutter power difference due to the measured refractivity profile and its trilinear approximation increases from the average of 8.2 dB at 3 GHz to 13.3 dB at 10 GHz. However, experimental measured profiles show that the trilinear approximation is sufficient for most of the surface-based ducts, especially when propagation is to be modeled at 3 GHz and lower frequencies [13].

A wavelet representation of the conductivity profile was suggested in the similar inverse scattering problems arising in geophysical prospecting [81,82]. Generalized Karhunen–Loeve transform [83] was used by [84] to find the the tropospheric refractivity basis vectors of VOCAR 1993 profiles measured off the coast of California. Both of these approaches are capable of representing environmental profiles in more detail with additional complexity in inversions.

2.2.3 Elevated ducts

Elevated ducts, schematically shown in Fig. 2.2d, are unstable atmospheric conditions that are primarily observed over the land but may also be formed across the seashore when cool air flows over a warmer sea [62,85,86]. The effects from these types of ducts are not visible on a radar screen since radar beams get trapped in the elevated layer above the ocean level. Elevated ducts might be predicted from the nature of heat absorbing and radiating boundaries and the cloud cover [62].

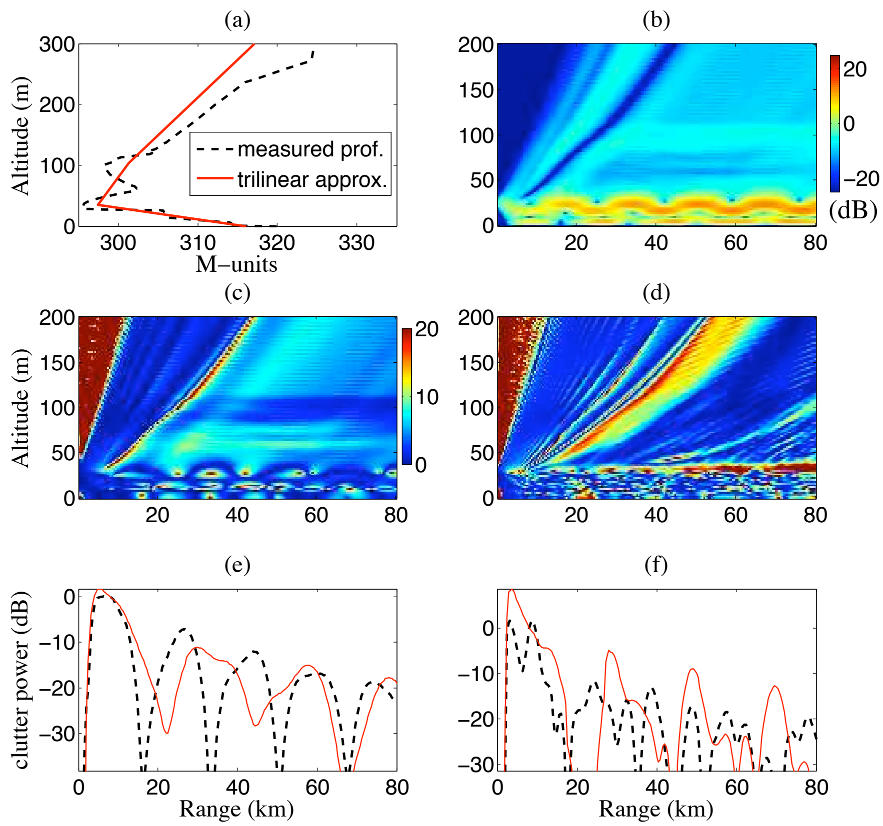

Figure 2.3: (a) A measured profile from the 1998 SPANDAR and its trilinear approximation. (b) propagation loss (dB) of the measured profile at 3 GHz. Propagation loss difference of the measured profile and the trilinear approximation at (c) 3 GHz, (d) 10 GHz. Clutter power comparison of the profile and its trilinear approximation at (e) 3 GHz, (f) 10 GHz.

2.3 Electromagnetic theory and forward modeling

Given a refractivity structure $\mathbf{m}$ in a maritime environment, the expected clutter power is obtained as a function of radar and environmental parameters. Assuming that electromagnetic waves hit the surface at a single grazing angle at range r, the received radar power is [1,87]:

$$P_r(r) = \frac{P_t G A_e \sigma F^4(r, \mathbf{m})}{(4\pi)^2 r^4 L} \ , \tag{2.6}$$

where P_t is the transmitter power, G the antenna gain, A_e the antenna effective aperture, σ the effective cross section of the scatterer, L the total assumed system losses, and F is the propagation factor at the sea surface. The pattern propagation factor F is defined as the ratio of the magnitude of the electric field at a given point under specified conditions to the magnitude of the electric field under free-space conditions [61]: $F(r) = \frac{|E(r)|}{|E_{fs}(r)|}$. F is a function of range r and the refractivity structure $\mathbf{m}$ at each location. The antenna effective aperture is obtained as a function of the wavelength λ, $A_e = \frac{\lambda^2 G}{4\pi}$. The clutter cross-section σ becomes $\sigma = A_c \sigma_0$ where σ_0 is the clutter cross section per unit area and A_c is the area of the radar cell [1]:

$$A_c = r\theta_B (c\tau/2) \sec\left(\theta(r, \mathbf{m})\right) \ , \tag{2.7}$$

with θ_B the antenna pattern azimuthal beamwidth, c the propagation speed, τ the pulse width, and θ is the grazing angle which is a function of range and the environmental refractivity. From this point on, $F(r, \mathbf{m})$ and $\theta(r, \mathbf{m})$ are shown as F and θ for simplicity. Thus, the clutter power at the range r is obtained as:

$$P_c(r) = \frac{P_t G^2 \lambda^2 \theta_B c \tau \sigma_0 \sec(\theta) F^4}{2(4\pi r)^3 L} \ . \tag{2.8}$$

The propagation factor F is calculated by numerical solutions to the wave propagation problem (Section 2.3.1). The sea surface-reflectivity per unit area σ_0 is calculated from semi-empirical models that fit the experimental measurements to a function of system parameters (Section 2.3.2).

The angle with which electromagnetic waves hit the ocean surface θ varies with range. However, the dependence of the clutter model on grazing angle has been neglected at far distances from the radar in [12–15,78,84,88–91]. The $\sec(\theta)$ term also is a weak function of θ at low angles. Thus, normalization of the clutter power by the power at range r_0 yields the approximation:

$$\frac{P_c(r)}{P_c(r_o)} \simeq \left(\frac{r_o}{r}\right)^3 \frac{F^4(r)}{F^4(r_o)} \, . \tag{2.9}$$

The dependence of the sea-surface reflectivity on grazing angle in an evaporation duct has been considered in [12] and concluded that $\sigma_0 \propto \theta^0$ given that the clutter cells are far enough from the radar. They also investigated the existence of a minimum wind speed under which radar return is not reliable for duct height inversion. The minimum wind speed (usually less than is 2 m/s) depends on the radar parameters and sensitivity. To overcome the problem of uncertainty of σ_0, geometrical ray tracing and rank correlation was used by [57] for inversion of surface-based ducts.

The assumption that there is a single grazing angle θ at each range is not always valid, especially in strong surface-based ducts where multiple electomagnetic waves with different angles hit the surface at each location. Karimian *et. al.* suggested a clutter model that depends on all grazing angles proportional to their relative powers [26]:

$$P_c(r) = \frac{\alpha_c(r) F^4(r)}{\int_\theta \gamma(\theta) d\theta} \int_\theta \frac{\sigma_{0,GIT}(\theta) \sec(\theta) \gamma(\theta)}{F^4_{std}(\theta)} d\theta \, , \tag{2.10}$$

where $\alpha_c(r) = \frac{P_t G^2 \lambda^2 \theta_B c \tau}{2(4\pi r)^3 L}$ includes all grazing angle independent terms, $\sigma_{0,GIT}$ is the sea surface reflectivity from the GIT model (discussed in Section 2.3.2), $\gamma(\theta)$ is the relative energy of incident wavefronts at each grazing angle obtained from a curved wave beamformer, and $F_{std}(\theta)$ is the propagation factor of a standard atmosphere at a range with the same grazing angle. An analysis of the performance of different clutter models in RFC inversions is provided in [27].

2.3.1 Wave propagation modeling

From the early days of wave propagation modeling, a divergence arose due to the distinct differences in applications emphasizing environmental effects over terrain versus over the oceans. Due to the advances in computer processing as well as innovative mathematical techniques for numerically intensive problem solving, the most popular techniques for Radio Frequency (RF) propagation modeling have converged such that these same methods are well suited for both land and water propagation paths. Since the emphasis of this paper is on the estimation of refractive conditions over the ocean, this section will describe only those RF propagation modeling techniques and algorithms as they pertain to modeling anomalous propagation effects on over-water paths.

One of the first radiowave propagation models that took into account the effects of both evaporation ducts and surface-based ducts was based on the techniques described in [61] and [92]. The model determines the coherent sum of the direct and surface-reflected fields within the optical interference region, also accounting for divergence and non-perfect reflection by use of a modified Fresnel reflection coefficient [93]. Modeling refractive effects is limited since within this region, the use of an effective earth radius factor is employed to account for non-standard conditions. For diffraction effects beyond the radio horizon, ducting effects are based on a single mode model where an empirical fit to waveguide solutions are used to modify Kerr's standard diffraction method [75].

For modeling of height-varying refractive conditions, waveguide models offer a much higher fidelity solution and have been in use since the early 1900s [94]. Waveguide models employ normal mode theory and are well suited when refractive conditions do not change along the path. Due to the high computational requirements for mode searches, another caveat is that normal mode models are typically used beyond the radio horizon where far fewer modes are needed for a solution [43,75].

One of the more popular techniques for RF propagation modeling is the parabolic equation (PE) method, also known as the paraxial approximation method. Originally used by [95], the PE method allows for propagation conditions to vary in both height and range. However, the PE method was not in practical use until [96] developed a technique called the split-step Fourier (SSF) method, initially applied to underwater acoustic propagation. The SSF method took advantage of fast Fourier transforms that led to extremely efficient numerical solutions of the PE. [97,98] modified the underwater acoustic SSF PE to model radiowave propagation in the troposphere. Since that time many improvements and mathematical techniques have been introduced in the SSF PE algorithm for applications to RF propagation in the troposphere. For an excellent treatise on the development of many of these techniques, the reader is referred to [22].

Due to its efficiency and accuracy the SSF PE algorithm is now widely used in many radiowave propagation models, including the model used here to obtain results presented in this paper. A general description of the SSF PE algorithm is given in the following, with more details provided on specific implementation of the model used here. Applying the simple assumption of a slowly varying medium, Maxwells equations can be reduced to the scalar two-dimensional (Cartesian) elliptical Helmholtz equation:

$$\frac{\partial^2\psi(x,z)}{\partial x^2} + \frac{\partial^2\psi(x,z)}{\partial z^2} + k_0^2 n^2 \psi(x,z) = 0 \;, \tag{2.11}$$

where $\psi(x,z)$ is a function of the electric or magnetic field, depending on the polarization of the radiated field; and n is the refractive index of the medium (implicitly also a function of x and z). The usual starting point for the derivation of the PE is substituting the function $\psi(x,z) = e^{jk_0x}u(x,z)$ in (2.11), then factor the result into, respectively, forward and backward pseudo-differential equations:

$$\frac{\partial u(x,z)}{\partial x} + jk_0 \left[1 - \sqrt{\frac{1}{k_0^2}\frac{\partial^2}{\partial z^2} + n^2}\right] u(x,z) = 0 \;, \tag{2.12}$$

$$\frac{\partial u(x,z)}{\partial x} + jk_0 \left[1 + \sqrt{\frac{1}{k_0^2}\frac{\partial^2}{\partial z^2} + n^2}\right] u(x,z) = 0 \;. \tag{2.13}$$

This substitution effectively removes the rapid phase variation in ψ, leaving $u(x,z)$ a slowly varying function in range. In most PE models used for long range radiowave tropospheric propagation, only the forward propagating term (2.12) is solved, and the backward propagating term is ignored.

Initial PE algorithms incorporated simple approximations to (2.12), resulting in the standard PE (SPE). The limitation with using the SPE is that it is a narrow-angle approximation and leads to larger errors when propagating at large angles, typically greater than $10°$ for microwave frequencies. [99] developed the wide-angle PE (WAPE) for propagation within optical fibers, by using an alternative approximation of the square-root operator. Later, [100] quantified the error associated with the use of various approximations to the square-root operator, concluding that the WAPE propagator developed by Feit and Fleck was a substantial improvement in reducing phase errors at large propagation angles necessary for their work in underwater acoustic propagation. More recently, [101] analyzed the differences between the SPE and WAPE and offered yet a further improvement for the WAPE and wide-angle sources.

The Leontovich surface impedance boundary condition must then be applied to obtain a solution for the WAPE:

$$\left.\frac{\partial u}{\partial z}\right|_{z=0} + \alpha u\big|_{z=0} = 0 \ , \tag{2.14}$$

where the complex α is given by

$$\alpha_{h,v} = jk_0 \sin\theta \left[\frac{1-\Gamma_{h,v}}{1+\Gamma_{h,v}}\right] \ . \tag{2.15}$$

Here, θ is the grazing angle of the radiated field at the surface, Γ is the Fresnel reflection coefficient - also dependent on the grazing angle, and the subscripts h and v refer to horizontal and vertical polarization respectively. The discrete mixed Fourier transform (DMFT) formulation provided by [21] implements the impedance boundary condition and derives the new split-step solution entirely in the discrete domain. The DMFT method has the added advantage that it retains numerical efficiency due to requiring only sine transforms. Further refinement of the DMFT was presented by [102] where they applied various difference formulations for (2.14) to arrive at an improved DMFT algorithm, reducing much of the numerical instabilities associated with the quantity $\alpha_{h,v}$ when $Re(\alpha_{h,v})$ approaches zero.

The propagation model used for the results presented in this paper implements the WAPE and the DMFT algorithm as described in [21,101,102] and is called the Advanced Propagation Model (APM). The handling of range-varying vertical refractive profiles is described in [103] and a general description of the APM is provided in [104].

Pertinent to the RFC methodology is the accuracy of the forward scattered field, which is subsequently dependent on how $\alpha_{h,v}$ is modeled. Typically, the boundary condition is modeled such that a constant impedance is assumed within each range step, dependent on a single grazing angle associated with the dominant mode of propagation for the specified refractive environment. We apply the Kirchoff approximation and model the sea surface boundary by determining an effective impedance described by a reduction, ρ, to the smooth surface Fresnel reflection coefficient, Γ_0, based on the

Miller-Brown-Vegh (MBV) model [105]:

$$\Gamma_{h,v} = \rho\Gamma_{0h,v} \tag{2.16}$$

$$\rho = e^{-2(2\pi\gamma)^2} I_0 \left[2(2\pi\gamma)^2\right] \tag{2.17}$$

$$\gamma = \frac{h_w \sin\theta}{\lambda} \tag{2.18}$$

I_0 is the modified Bessel function of the first kind, and h_w is the rms wave height from the Phillips ocean wave spectrum [106]:

$$h_w = 0.0051 v_w^2\ , \tag{2.19}$$

where v_w is the wind speed in m/s. Within APM, ρ is approximated according to [107] by the expression

$$\rho = \frac{1}{\sqrt{3.2\chi - 2 + \sqrt{(3.2\chi)^2 - 7\chi + 9}}}\ , \tag{2.20}$$

$$\chi = 8\pi^2\gamma^2\ . \tag{2.21}$$

Next is to determine the grazing angle at each PE range step to compute the effective reflection coefficient and subsequent impedance. Grazing angles at the sea surface can easily be found using a geometric ray trace based on small angle approximations to Snell's law [25]. The caveat is that for surface-based ducting conditions, there will be multiple grazing angles within a given range interval/step, as shown in Fig. 2.4. Figure 2.4(a) shows the refractivity profile of a 300 m surface-based duct, and the corresponding grazing angles are shown in Fig. 2.4b. Notice that beyond the skip zone, at ranges beyond 80 km, there are multiple grazing angles (i.e., multiple modes) present within a given range interval. The challenge is determining the proper grazing angle associated with the dominant mode of propagation at a particular range. Geometric ray tracing techniques offer no further information, therefore, spectral estimation techniques have also been used [21,24,104] in combination with geometric ray trace methods to obtain the appropriate angle at a given range particularly useful in complex environments where the propagation path is a combination of sea, land, and a range-dependent atmosphere.

Of course, one of the caveats of modeling the impedance in this way is that for surface-based ducting environments it ignores the many, equally dominant, modes propagating within the duct at multiple grazing angles within a range step. The advantage

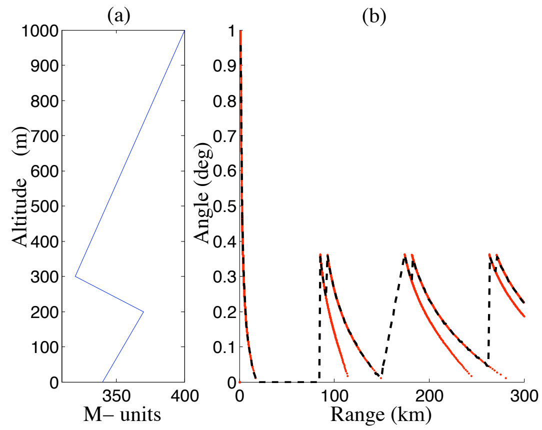

Figure 2.4: (a) Refractivity profile of surface-based duct used for (b) determination of grazing angles by ray trace (solid) and final maximum angles (dashed lines) used for computing $\alpha_{h,v}$.

of using the MBV method to modify the surface impedance is that it is easy to implement and for the most part has been shown to perform very well for range-independent evaporation duct environments where the incident field can be described, to a very good approximation, by a single grazing angle beyond the interference region [12,38].

A more rigorous, albeit conventional, approach has been provided by [108] to model a non-constant impedance that directly takes into account effects of the angle-dependent reflection coefficient present at all grazing angles. However, in keeping with the more numerically efficient SSF PE approach, and considering the design toward operational applications, the maximum grazing angle (shown by the dashed line in Fig. 2.4b) is used in computing $\alpha_{h,v}$ to model rough surface effects. This results in maximum, or worst-case, clutter values and will in general over-estimate sea clutter.

Finally, a recent approach to more accurately model the various field strengths at the surface, and subsequently, clutter power described by multiple grazing angles, has been provided by [26] that takes all grazing angles and their relative powers at each range-step into account.

For the RFC application, the propagation factor, F, in the clutter equation (2.8–5.2) is a function of the complex PE field and the range (note that range is shown by r in the clutter equations and by x in this section, since Maxwell's equations are solved in

Cartesian coordinates):

$$F = |u(x, z_{\text{eff}})|\sqrt{x}\ , \tag{2.22}$$

where z_{eff} is the effective scattering height, taken as 0.6 times the mean wave height [42], or approximately 1 m above the ocean for most situations [12,104]. Theoretically, F should be computed from the incident field at the sea surface. However, PE approximations yield the propagation factor due to the total field which is close to zero at the sea surface and high frequencies. [109] showed that the clutter power using the total field propagation factor at the effective scattering height is proportional to the clutter power using the incident propagation factor.

2.3.2 Sea surface reflectivity models

Proper characterization of the quantity $\sigma_0 F^4$ in (2.8) is key to providing reasonable clutter predictions to perform RFC. The difficulty is that the surface reflectivity is implicitly dependent on the forward propagation effects defined by F. They are inherently coupled yet these two quantities are commonly treated separately to get an estimate of the return clutter. Most sea surface reflectivity models, therefore, are semi-empirical and are based on site-specific propagation data, typically with no corresponding meteorological measurements.

There are several semi-empirical models for the average sea surface reflectivity per unit area that fit the experimental sea clutter data to a function of radar frequency, grazing angle, beam width, wind speed, radar look direction with respect to the wind, and polarization. This quantity, represented by σ_0, is also referred to as the normalized radar reflectivity [110].

A hybrid model by [111] and the Georgia Institute of Technology (GIT) model [112] are among the classic sea surface reflectivity models for low grazing angles that are valid in the S and X band frequencies. A comparison of different models is provided in [42]. GIT, Technology Services Corp. (TSC) [113], and Barton (BAR) reflectivity models at 3 GHz are compared in Fig. 2.5a. A similar comparison at 9.3 GHz with the additional Sittrop (SIT) [114] model is shown in Fig. 2.5b. Notice that the TSC, BAR, and SIT models show similar dependence of σ_0 on grazing angle, whereas the GIT model exhibits higher attenuation at lower grazing angles. Lower grazing angles imply

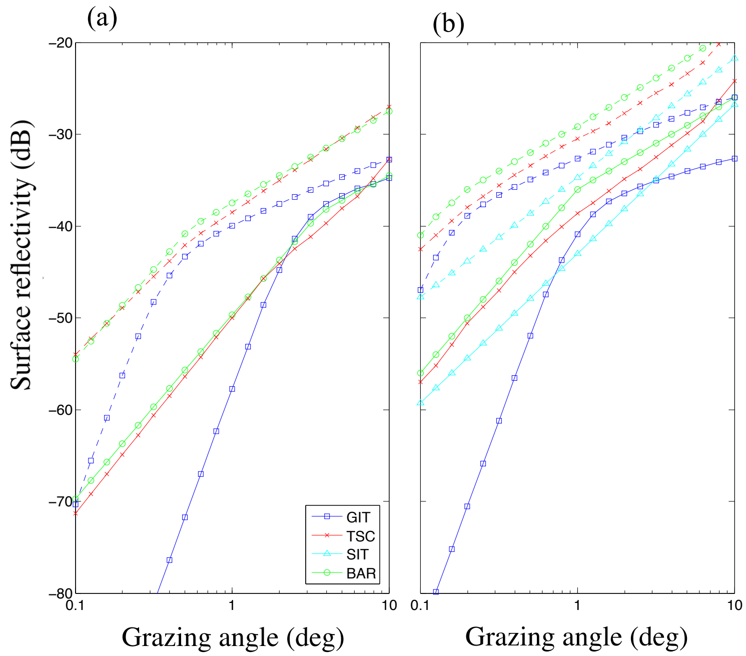

Figure 2.5: Reflectivity vs. grazing angle for several sea surface reflectivity models at (a) 3 GHz, and (b) 9.3 GHz.

the region near the radio horizon subject to diffraction effects. The increased attenuation shown by the GIT model as a function of decreasing grazing angle is indicative of standard diffraction effects, and it is for this reason the GIT model has been more widely used. That is, the GIT reflectivity can be assumed to be representative of σ_0 under standard atmosphere conditions.

[42] modified the GIT model to consider ducting effects on the radar backscatter by dividing σ_0 by the standard atmosphere propagation factor and multiplying by the propagation factor of the desired conditions [87].

Normalized mean sea backscattering coefficient σ_0 for grazing angles of 0.1 to 60° and frequencies of 0.5 to 35 GHz are tabulated by [110] based on almost 60 experiments. A model to fit the aforementioned dataset for grazing angles less than 10° and frequencies up to 35 GHz is provided by [115]. Modeling the sea surface reflectivity suitable for RFC applications remains an active field of research.

Calculation of the grazing angle is the key to the calculation of radar backscatter. A hybrid of ray tracing and plane wave beamforming has been suggested in the works of [21,25,104] to find the angle of arrival based on the propagation conditions. [26] suggested a curved wave beamformer that depends on the refractivity profile at each location.

2.4 Inverse problem framework

The radar clutter depends on the two way propagation loss from the transmitter to the range cell. The loss in turn depends on the environmental refractivity profile through which the wave is propagated. The expected clutter power of each candidate profile is computed and an objective function Φ that quantifies the difference between the observed, $\mathbf{P}_o$, and the simulated clutter power, $\mathbf{P}_s(\mathbf{m})$, is formed. $\mathbf{P}_o$ and $\mathbf{P}_s$ are the vectors of clutter power over the radar range. The candidate profile that yields the minimum difference is declared as the best match.

$$\hat{\mathbf{m}} = \underset{\mathbf{m}}{\mathrm{argmin}}\ \Phi(\mathbf{P}_o, \mathbf{P}_s(\mathbf{m}))\ . \tag{2.23}$$

The simulated clutter is a function of the propagation factor F, as seen in (2.6). F in turn, is a function of the environmental profile m. Using an l_2 norm as the objective function Φ yields:

$$\Phi = \|\mathbf{P}_o - \mathbf{P}_s(\mathbf{m})\|^{\mathbf{2}}\ , \tag{2.24}$$

which is also the negative log-likelihood function under the Gaussian noise assumption. Minimizing (5.5) over the refractivity profile $\mathbf{m}$ requires an efficient numerical search for the optimum values.

There have been several approaches to estimate the refractivity parameters from the observed clutter including: a matched–field processing approach toward inversion [76], a genetic algorithm [13], a Markov–chain Monte Carlo sampling approach to estimate the uncertainties of the inverted parameters [88], Markov state space model for microwave propagation [14], Kalman and particle filters [15], support vector machines [116], particle swarm optimization [89], a Bayesian approach with meteorological prior [17], an improved best fit approach [56,90] and a range adaptive objective function [117].

[118] suggested a matched-field processing approach for source localization and inversion for environmental parameters which was based on plotting ambiguity surfaces

of unknown variables. [76] showed successful application of the matched-field processing technique to invert for surface-based duct parameters. They also showed that it was not possible to invert for elevated duct parameters using single surface measurements.

Most of the previous RFC studies inverted the clutter power for the refractivity structure in a short range interval assuming changes in the refractivity profile to be negligible. [13] inverted for a range-dependent profile by considering range-dependent parameters. [14] used a Markov chain model on the propagation state space [119] to consider a range dependent profile. The latter approach reduces the complexity of inversions based on the number of unknown profiles with the added advantage of correcting inverted profile of shorter ranges efficiently by considering clutter power from longer ranges.

2.4.1 Likelihood function

The relationship between the observed complex-valued radar I and Q components of the field $\mathbf{u}_{I,o}$ and $\mathbf{u}_{Q,o}$ over N_r range bins and the predicted field $\mathbf{u}_{I,s}$ and $\mathbf{u}_{Q,s}$ is described by the model:

$$\begin{aligned} \mathbf{u}_{I,o} &= \sqrt{\mathbf{n}_1}\mathbf{u}_{I,s}(\mathbf{m})e^{j\phi_1} + \mathbf{n}_2 e^{j\phi_2} && (2.25) \\ \mathbf{u}_{Q,o} &= \sqrt{\mathbf{n}_1}\mathbf{u}_{Q,s}(\mathbf{m})e^{j\phi_1} + \acute{\mathbf{n}}_2 e^{j\acute{\phi}_2} && (2.26) \end{aligned}$$

where $\mathbf{n}_1$ is the multiplicative random variable in the modeled electric field due to a variable sea surface reflectivity. [17] considered different probability distributions for the random variable $\mathbf{n}_1$ including lognormal, K-distribution and Rayleigh. Here, a lognormal distribution is assumed for each element of the vector $\mathbf{n}_1$. Noise in the receiver, $\mathbf{n}_2$ and $\acute{\mathbf{n}}_2$, are modeled by Gaussian distributions. $\phi_1, \phi_2, \acute{\phi}_2$ are the random phase components of the complex random variable with uniform distributions:

$$\begin{aligned} \{\log n_1\}_1^N, &\sim \mathcal{G}(0, \sigma_1^2) && (2.27) \\ \{n_2\}_1^N, \{\acute{n}_2\}_1^N &\sim \mathcal{G}(0, \sigma_2^2) && (2.28) \\ \{\phi_1\}_1^N, \{\phi_2\}_1^N, \{\acute{\phi}_2\}_1^N &\sim \mathcal{U}(0, \pi) && (2.29) \end{aligned}$$

The radar output power is obtained by:

$$\mathbf{\Pi} = |\mathbf{u}_I|^2 + |\mathbf{u}_Q|^2 \, . \tag{2.30}$$

Thus, the observed and simulated clutter power are related by:

$$\boldsymbol{\Pi}_o = \mathbf{n}_1 \boldsymbol{\Pi}_s(\mathbf{m}) + \mathbf{n}_r \tag{2.31}$$

$$\{\log \mathbf{n}_1\}_1^N \sim \mathcal{G}(0, \sigma_1^2) \tag{2.32}$$

$$\{\mathbf{n}_r\}_1^N \sim \chi^2 \tag{2.33}$$

where $\mathbf{n}_1$ is the multiplicative noise with a lognormal distribution, and $\mathbf{n}_r$ is the additive receiver noise with a χ^2 distribution and 2 degrees of freedom. Working in the high CNR (clutter to noise ratio) regime, the $\mathbf{n}_r$ term can be neglected. Thus, the modeled power in the logarithmic domain is obtained as:

$$\mathbf{P}_o = \mathbf{P}_s(\mathbf{m}) + \mathbf{n} \tag{2.34}$$

$$\{\mathbf{n}\}_1^N \sim \mathcal{G}(0, \sigma^2) , \tag{2.35}$$

where, $\mathbf{P}_o$ and $\mathbf{P}_s(\mathbf{m})$ are vectors of the observed and simulated clutter power of the profile $\mathbf{m}$ in dB, and $\mathbf{n} = 10 \log \mathbf{n_1}$.

More than one source of clutter power observations can be used in an inversion. These sources can include the clutter power at different frequencies, different radar elevation angles, or different snapshots with similar conditions where $\mathbf{P}_{n,o}$ corresponds to the nth source of the observed clutter power. Given N different sources with uncorrelated noise power ν_n, the maximum likelihood function becomes: [1]

$$\mathcal{L}(\mathbf{m}) = \prod_{n=1}^{N} (\pi \nu_n)^{-N_r} \exp\left[-\frac{\|\mathbf{P}_{o,n} - \mathbf{P}_{s,n}(\mathbf{m})\|^2}{\nu_n} \right] . \tag{2.36}$$

Assuming that the noise power $\{\nu_n\}_{n=1..N}$ is constant across different observations, the negative log-likelihood function is simplified to

$$\Phi(\mathbf{m}) = -\log \mathcal{L}(\mathbf{m}) \propto \sum_{n=1}^{N} \|\mathbf{P}_{o,n} - \mathbf{P}_{s,n}(\mathbf{m})\|^2 . \tag{2.37}$$

The maximum likelihood estimate $\hat{\mathbf{m}}$ for $\mathbf{m}$ is obtained by minimizing (2.37) over the model parameter vector $\mathbf{m}$, which is similar to (5.5).

[11] $|\mathbf{x}| = (|x_1|, |x_2|, ...)$ and $\|\mathbf{x}\|^2 = \sum_i |x_i|^2$.

2.4.2 An inversion example

A set of refractivity profile measurements and radar returns was recorded at Wallops Island, Virginia, April 1998 [12,13]. Clutter signals were measured using the Space Range Radar (SPANDAR) with operational frequency of 2.84 GHz, horizontal beamwidth of $0.4°$, elevation angle of 0, antenna height of 30.78 m, and vertical polarization. The refractivity profiles of the environment were recorded using an instrumented helicopter provided by the Johns Hopkins University Applied Physics Laboratory. The helicopter flew in and out along the $150°$ radial from a point 4 km due east of the SPANDAR in a saw-tooth pattern with each transect lasting 30 min.

The range-dependent refractivity profile measured by the helicopter is shown in Fig. 2.6a. This profile corresponds to the measurement on April 2, 1998 from 13:19:14 to 13:49:00 (Run 07). The spatial variation of the M-profile is small in the 0–45 km range. Thus, RFC results of the corresponding clutter observations are compared to the average of the measured M-profiles in that range interval. Note that although the experimental measurements are from a range-dependent refractivity profile, inversions are based on a range-independent profile.

Recorded clutter power of the SPANDAR between azimuth 142–166° is used to estimate the trilinear function representing a surface-based duct since the clutter pattern (Fig. 2.1d) is rather stationary in this interval. The probability distribution of the refractivity profile from all inversion results is obtained and the maximum a posterior (MAP) solution of this distribution is found to be the refractivity profile that fits all data. Only the first 60 km of the radar clutter is used to invert for the refractivity profile to maintain a high CNR and to avoid high spatial variations of refractivity with range. A multiple angle clutter model based on curved wave beamforming [26] is used to calculate the clutter power, and APM [104] is used to calculate the electric field and propagation loss. Fig. 2.6 shows the inverted profiles obtained from clutter power observed along the 150° azimuth, the helicopter measured refractivity along the $150°$ azimuth and the span of inverted profiles using clutter power along 142–166°.

Fig. 2.7 shows the propagation loss using the inverted profile from Fig. 2.6b and a standard atmosphere. Surface-based ducting conditions result in the extended range of the radar and radar fades in unexpected locations assuming a standard atmosphere.

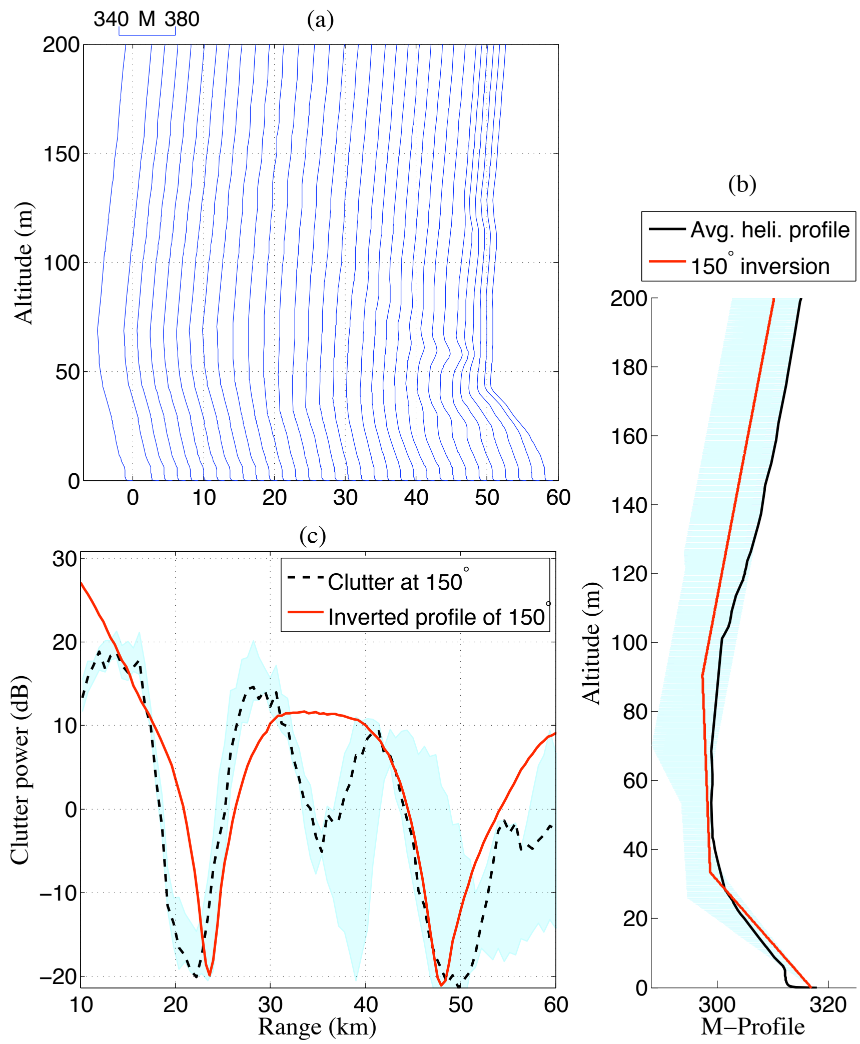

Figure 2.6: (a) Range-dependent refractivity profile recorded by an instrumented helicopter along the $150°$ azimuth. (b) Average of the first 45 km of the measured profile compared to the inverted profiles of $150°$ clutter (solid) and the MAP profile of 142–166° (shaded). (c) observed and modeled clutter power of the inverted profile.

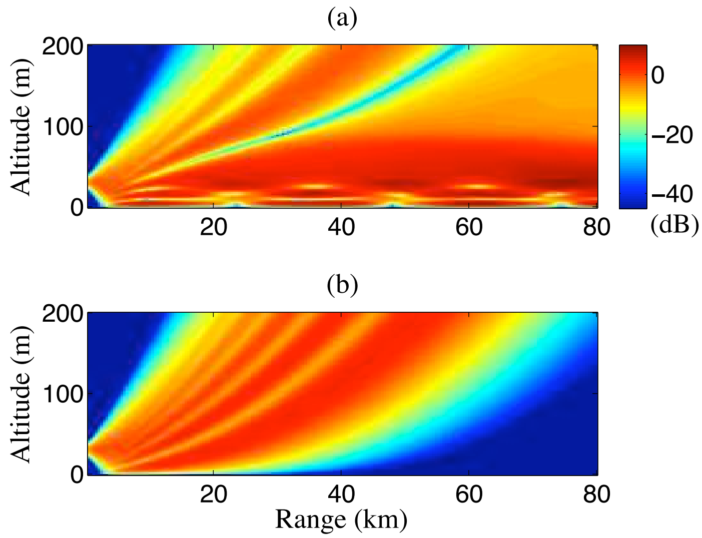

Figure 2.7: Propagation loss: (a) MAP estimate of the refractivity profile given the clutter power at 150° azimuth of SPANDAR Run 07, and (b) standard atmosphere.

Radar parameters in this figure are identical to those of the SPANDAR.

2.4.3 Bayesian approach

One important motivation behind estimation of the refractivity structure in the environment is to predict the radar performance in non-standard atmospheric conditions. This requires the statistical properties of the parameters-of-interest such as the propagation loss which can be computed from the statistical properties of the atmospheric refractivity. The unknown environmental parameters are taken as random variables with corresponding one–dimensional (1–D) probability density functions (pdfs) and an n–dimensional joint pdf. This probability function can be defined as the probability of the model vector $\mathbf{m}$ given the observed clutter power $\mathbf{P}_o$, $p(\mathbf{m}|\mathbf{P}_o)$, and it is called the posterior pdf (PPD). The profile $\mathbf{m}$ with the highest probability is referred to as the maximum a posteriori (MAP) solution. The posterior means, variances, and marginal probability distributions can be found by integrating over this PPD:

$$\mu_i = \int \dots \int_{\mathbf{m}'} m'_i p(\mathbf{m}'|\mathbf{P}_o)\mathbf{dm}' \,, \tag{2.38}$$

$$\sigma_i^2 = \int \dots \int_{\mathbf{m}'} (m'_i - \mu_i)^2 p(\mathbf{m}'|\mathbf{P}_o)\mathbf{dm}' \,, \tag{2.39}$$

$$p(m_i|\mathbf{P}_o) = \int \dots \int_{\mathbf{m}'} \delta(m'_i - m_i) p(\mathbf{m}'|\mathbf{P}_o)\mathbf{dm}' \,. \tag{2.40}$$

The posterior density of any specific environmental parameter can be obtained by marginalizing the n–dimensional PPD as given in (2.40) [120]. [79] used importance sampling (IS) [121] to compute the necessary multi-dimensional integrals needed to map the environmental uncertainty into propagation loss uncertainty. IS produces unbiased distributions of the desired variables, however, the variance of the estimates depend heavily on the importance density used in IS. Another problem with IS is the slow rate of convergence for the numerical computation of the integrals. [79] also compared IS to using just the 1-D marginals of refractivity parameters to compute the PDF of propagation loss. As long as the interparameter correlations are negligible, using marginals is computationally more efficient than IS. They later showed that lowering the peak clutter to noise ratio broadens the a posteriori distribution of the propagation loss [78].

The error in IS is minimized when samples are drawn from the posterior distribution of the environmental parameters $p(\mathbf{m}|\mathbf{P}_o)$. Sampling from the posterior requires a Markov chain Monte Carlo (MCMC) class sampler [121,122] such as the Metropolis-Hastings (MH) [123] and the Gibbs samplers [124]. MCMC methods are guaranteed to asymptotically converge to the true parameter distribution at a high computational cost. [88] used a MH sampler to find the a posteriori distribution for the environmental model parameters and used the MH sampler output to map the environmental uncertainty into the propagation loss domain.

[37] introduced a hybrid genetic algorithms (GA)–MCMC method to estimate the posterior probability faster than MCMC which does not suffer from the bias of histograms obtained from the GA. The hybrid GA–MCMC approximates the posterior distribution faster than an MCMC by first performing a GA inversion, discretizing the environmental parameter domain using the GA samples via Voronoi decomposition and the nearest neighborhood method [125,126], and finally applying a fast Gibbs sampler

over this discrete space. The posterior distribution can be found using the Bayes rule:

$$p(\mathbf{m}|\mathbf{P}_o) = \frac{p(\mathbf{m})\mathcal{L}(\mathbf{m})}{p(\mathbf{P}_o)} \propto p(\mathbf{m})\mathcal{L}(\mathbf{m}) \; , \tag{2.41}$$

with

$$p(\mathbf{P}_o) = \int_{\mathbf{m}} p(\mathbf{P}_o|\mathbf{m})p(\mathbf{m})\mathrm{d}\mathbf{m} \; . \tag{2.42}$$

The likelihood function $\mathcal{L}(\mathbf{m})$ is the same as in (2.36), assuming a zero-mean Gaussian distribution for the error. The prior $p(\mathbf{m})$ represents *a priori* knowledge about the environmental parameters $\mathbf{m}$, which might be from the meteorological statistics [17] or from the result of previous inversions [15,56]. A non-informative or flat prior assumption reduces (2.42) to:

$$p(\mathbf{m}|\mathbf{P}_o) \propto \mathcal{L}(\mathbf{m}) \; , \tag{2.43}$$

which has been discussed in Section 2.4.1. Fig. 2.8 is adopted from [88] which shows the highest posterior density (HPD) of the propagation loss obtained from the Metropolis samples of refractivity model parameters from Fig. 2.6. Posterior distributions are shown at a fixed range of 60 km and different altitudes of 28 and 180 m, one inside and one outside the duct. The point inside the duct exhibits a narrow distribution while the variance of the estimated propagation loss outside the duct is much larger. As expected, the detection range increases along the horizon but this increase is not uniform. Fig. 2.8c shows the effects of uncertainty in the environmental parameters to a simple problem of target detection given that the target is an isotropic antenna with the radar cross section of 1 m^2. The detection threshold in this example is chosen as 35 dB one way loss of the electric field.

A Markov state space model as discussed by [14] also provides a Bayesian framework by considering the inversion result of the previous states to invert for the current range step.

Continuous temporal and spatial variations in the environment led [15] to use extended [120] and unscented [127,128] Kalman filters to track RFC results along with Sequential Monte Carlo [60,129] methods such as the particle filters. The paper compared the filter performances in RFC tracking for different types of ducts and computed the Bayesian Cramer-Rao lower bound (CRLB) which presents a lower bound to the RMS error.

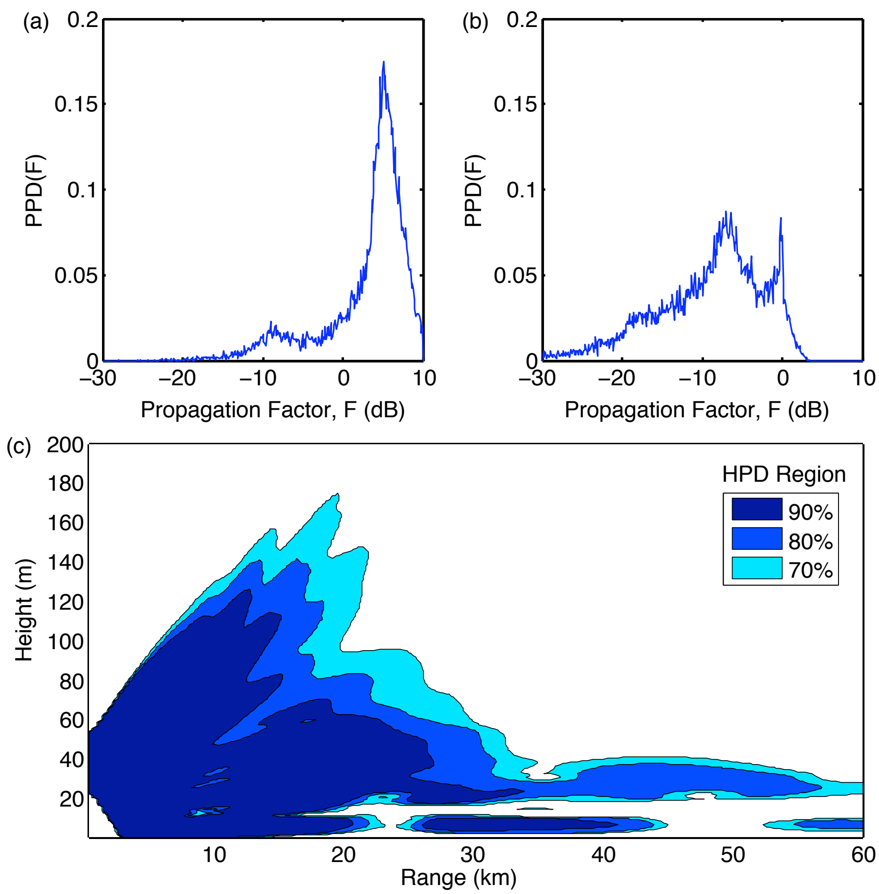

Figure 2.8: Posterior probability distribution of the propagation loss at range 60 km and altitudes of (a) 28 m, and (b) 180 m above the mean sea level, from the inversion of Fig. 2.6. (c) Detection probability given an isotropic target with an RCS of 1 m^2.

[56] provided a non-Bayesian approach to inversion but modeled a history of inverted parameters of surface-based ducts to keep the results smooth in azimuthal variations. They considered a library of pre-computed propagation losses of candidate profiles to find the one with the minimum distance to the observed clutter. Duct height variations are limited in the latter study and a smoothing procedure on the refractivity profiles is performed after inversions.

2.4.4 Alternative RFC formulations

The form of the objective function in (2.37) suggests that some observations can be weighted more heavily. Usage of different frequencies is discussed in [76]. [130] argued that using a single elevation angle results in inversions with low precision above the duct height. Thus, they used multiple elevation angles of the radar with different weights in the objective function to obtain more robust inversions.

[78] considered a weighting for the clutter power according to the distance of the range bin from the radar in an evaporation duct. [117] suggested using an adaptive weighting algorithm for different range bins in an evaporation duct that depends on the CNR. [78] have also suggested that RFC should be insensitive to the small variations of peak locations of clutter power with range. Thus, they produced random replica of the predicted field $\mathbf{P}_s$ to make predictions less prone to the measurement errors.

Consideration of an l_2 norm for error of $\Phi(\mathbf{m}) = \|\mathbf{P}_o - \mathbf{P}_s(\mathbf{m})\|^2$ is a consequence of assuming an additive uncorrelated Gaussian noise in (5.7). The term $\mathbf{n}_r$ in (2.31) models the noise floor in the receiver which has been modeled by a linear truncation procedure in the logarithmic power domain by [78] and by a complex Gaussian distribution on the field by [14,27]. A discussion of different random distributions and their effect on RFC is provided in [17].

Other objective functions have also been suggested in the statistical learning community. l_1 (sum of absolute error terms) and the Huber norm [131] are less sensitive to the outliers than the commonly used l_2 norm. The Huber norm is a hybrid of smooth l_2 norm for small errors and robust l_1 treatment of large residuals, which has been used by [132,133] for the robust inversion of the seismic data.

There have been approaches that do not use the clutter equation as a forward model for inversions. [57] used a rank correlation approach on the ray tracing results of candidate profiles to invert for the surface-based duct parameters based on the observed clutter power of a 5.6 GHz radar. A tomographic approach using a receiver array at the X-band and correlating the arrival wavefront spectrum to ray traces of candidate profiles has been suggested by [134]. In a similar problem, [40] used radar ground echo at low elevation angles to estimate the vertical gradient of refractivity near the ground. They used ray tracing to model the radar coverage. One shortcoming of the current RFC approaches is evident when surface and weather (volume) clutter are hard to separate such as in precipitation.

2.5 Conclusion and future directions

RFC is an approach to estimate the refractivity structure of a maritime environment based on the observed radar clutter power. Marine ducts and their mathematical models have been discussed, and a framework for casting an inverse problem was presented. An inversion consists of a forward model to map the candidate profiles to the observation domain, and a similarity measure to find the best profile. However, there are several shortcomings in the current approaches to RFC that need to be addressed in future studies:

Bilinear and trilinear approximations to surface-based ducts are not representative of the duct structure in some situations, and their performance worsens as the operational frequency increases. There have been attempts to overcome this problem by suggesting environmental refractivity models that rely on finding basis vectors of the refractivity profile. Models for duct structures are required that are simple (for easy inversion), and at the same time more representative of the true wave propagation, especially if RFC is to be implemented at frequencies higher than 3 GHz.

Sea surface reflectivity models that are currently used in the radar community, e.g. the GIT model, do not represent well the sea reflections at very low grazing angles. Thus, remote sensing problems require more realistic models of the sea surface reflectivity at these angles ($< 1°$).

One of the caveats of RFC algorithms is that detection of elevated ducts is not possible since the trapped electromagnetic waves do not interact with the sea surface. However, these ducts can be predicted based on meteorological conditions [62]. The 3-D refractivity profiles are intimately linked to the weather. There have been attempts to include climatological statistics of duct heights based on the observation location and time of the year for evaporation ducts [17].

Fusion of weather prediction algorithms with RFC inversions can greatly increase the performance of both. An example is in costal regions when the warm flow of air over the sea forms a rising surface duct for radar propagation. Numerical weather prediction (NWP) systems have undergone substantial development in the last decade. There currently exist capabilities to extract 48 h radar forecast based on output from NWP [135]. These forecasts are used now to predict the radar performance [136]. An improvement of RFC then would be using these fields as prior into the RFC inversion. After the inversion, the RFC posterior refractivity estimates could be used to influence the small-scale data assimilation for NWP. More research is required to fill the gap between weather prediction and RFC.

Acknowledgments

The contents of Chapter 2 were first published in the Journal of Radio Science as: A. Karimian, C. Yardim, P. Gerstoft, W. .S. Hodgkiss, Amalia Barrios , “Refractivity Estimation from Sea Clutter: An invited Review”, *Radio Sci.*, 46, RS6013, 2011.

Chapter 3

Multiple Grazing Angle Sea Clutter Modeling

3.1 Introduction

Lower atmospheric ducts over the ocean are common in many maritime regions of the world. These non-standard conditions result in effects such as significant variations in the maximum operational radar range, creation of radar fades where the radar performance is reduced, and increased sea clutter [1]. Atmospheric ducts are more common in hot and humid regions of the world. The Persian Gulf, the Mediterranean and California coasts are examples of such regions where an increase in the humidity pattern above the sea surface is accompanied by an increase in the temperature profile [17].

Calculation of the expected sea clutter power at low grazing angles requires modeling of ocean radar reflectivity per unit area [1]. It is common in practice to use the semi-empirical sea reflectivity model from the Georgia Institute of Technology (GIT) [112]. The GIT model is based on fitting a single grazing angle model to low angle sea surface clutter measurements. Dockery and Reilly modified the GIT model to take into account the effects of non-standard ducting conditions on clutter [42,87]. They divided the GIT reflectivity by the propagation factor obtained under standard conditions to remove the standard atmosphere effect on the measurements. More recent empirical models of sea clutter at low grazing angles are investigated in [115].

The occurrence of ducting conditions causes grazing angles to be range dependent, as the electromagnetic wave is trapped inside the duct. The strong dependence of sea surface reflectivity on low grazing angles makes estimation of these angles important. Ray tracing is a common way of finding the grazing angle at the sea surface in the microwave region. However, it fails to account for shadow zones [20]. Hence, angular spectral estimation can be used to obtain the angle of arrival (AOA) as a function of range. Vertical arrays at each range can be generated synthetically with samples of the field obtained from a parabolic equation code [22].

Grazing angle calculation in existing propagation software packages depends on tropospheric conditions. The Advanced Propagation Model (APM) software [20] uses the maximum grazing angle obtained from ray tracing for propagation over the ocean, while plane wave spectral estimation (PWS) is used to calculate the dominant grazing angle over land. The Tropospheric electromagnetic parabolic equation routine (Temper) [23] uses the MUSIC algorithm [24] in its automatic mode to obtain the grazing angle when changes of the refractivity index are high. A forward/backward spatial smoothing MUSIC method [137] is used, which divides the synthetic array into overlapping subarrays. This method assumes a constant refractivity along the array. Temper uses ray tracing for evaporation ducts where MUSIC is not reliable. Switching between ray tracing and spectral estimation requires an ad hoc decision rule based on the gradient of the refractivity index along the array [21,25].

Both APM and Temper use a parabolic equation approximation to the wave equation [20,23]. There also have been attempts to incorporate a grazing angle dependent impedance of the horizontal reflecting surface into the forward propagation formulation of the parabolic equation [108].

In this paper we propose a self-consistent way of obtaining the grazing angles so that it is not necessary to switch between grazing angle computation techniques. Curved wave spectral estimation (CWS) can be applied as an angular spectral estimation technique when the approximation of a constant refractivity index along the array fails. Hence, CWS is applicable to all atmospheric conditions with a refractivity index that varies with height.

The worst case clutter can be estimated using the maximum grazing angle obtained from ray tracing or angular spectral estimation [20]. However, a more realistic clutter model is needed in applications such as refractivity from clutter (RFC) [13–15,18,27,88,130]. Multiple grazing angle clutter provides such a model that takes all incident angles into account.

The single angle clutter equation is reviewed in Section 3.2. Array processing and the effects of vertical variations of refractivity on angular spectral estimation is discussed in Section 3.3. The angular power spectrum of the incident electromagnetic wave is used in Section 3.4 to construct a multiple angle clutter model. Section 3.5 provides several examples to show the performance of curved wave spectral estimation and the multiple grazing angle clutter model.

3.2 sea clutter at low grazing angles

Radars operating in maritime environments encounter a back-scattered signal from the sea surface. Received clutter depends on the refractivity profile of the environment known as the M-profile. This dependence makes inference of the refractivity profile from the observed clutter possible [13]. The expected clutter is expressed as [87]:

$$P_c(r) = \frac{P_t G^2 \lambda^2 \theta_B c \tau \sigma_0 \sec(\theta) F^4(r)}{2(4\pi r)^3 L}\ , \tag{3.1}$$

where P_t is the transmitter power, G is the antenna gain, λ is the wavelength, θ_B is the antenna pattern azimuthal beamwidth, c is the propagation speed, τ is the pulse width, σ_0 is the sea surface reflectivity per unit area, θ is the grazing angle at range r, F is the propagation factor, and L is the total assumed system losses.

The propagation factor, F, is defined as the ratio of the magnitude of the electric field at a given point under specified conditions to the magnitude of the electric field under free-space conditions with the beam of the transmitter directed toward the point in question [1]: $F(r) = |\frac{E(r)}{E_{fs}(r)}|$.

3.2.1 Modified GIT model

The standard GIT model, see Appendix 3.6, is a semi-empirical model that calculates the sea surface reflectivity [87]. This model is based on fitting the experimental measured average sea surface reflectivity to a function of polarization, radar frequency, grazing angle, wind speed and radar look direction. The effect of standard atmosphere can be removed by normalizing the GIT cross-section with respect to the 4/3 effective earth radius propagation factor in standard conditions [87], [138]:

$$\sigma_0(r,\theta) = \frac{\sigma_{0,GIT}(r,\theta)}{F^4_{std}(r')} \;, \tag{3.2}$$

where $F^4_{std}(r')$ is the two-way propagation factor of the standard atmosphere ($\frac{dM}{dh} = 0.118$ M-units/m) at the equivalent range r' with the same wind speed and an isotropic antenna. r' is the range that yields the same grazing angle θ under the standard atmospheric condition [138]:

$$r'(\theta) = \sqrt{a_e^2\theta^2 + 2a_e h_{ant}} - a_e\theta \;, \tag{3.3}$$

where a_e is the 4/3 average earth radius in meters, and h_{ant} is the antenna height relative to the sea surface.

Substitution of (3.2) into (4.1) yields the final form of the clutter power equation based on the modified GIT reflectivity:

$$P_c(r) = \frac{P_t G^2 \lambda^2 \theta_B c\tau \sigma_{0,GIT}(r,\theta)\sec(\theta) F^4(r)}{2(4\pi r)^3 L F^4_{std}(r')} \;. \tag{3.4}$$

Fig. 3.1 shows changes of sea surface reflectivity per unit area $\sigma_{0,GIT}$ for horizontal and vertical polarizations as a function of grazing angle and wind speed, with radar operating frequency of 3 GHz. Note that σ_0 varies as much as 45 dB in relatively calm sea conditions as the grazing angle changes from 0.1 to $1°$. The strong dependence of clutter power on sea surface reflectivity, and hence grazing angle, is a motivation to incorporate all incident angles into the clutter model.

3.3 Angular spectral estimation

Angular spectral estimation techniques find the incident power distribution versus grazing angle. The elements of the vertical synthetic array are formed from the complex field u at each range obtained from the FFT bins of the electromagnetic parabolic equation (PE) propagation model. For Cartesian coordinates [22]:

$$u(x,z) = e^{-jkx}\psi(x,z) \;, \tag{3.5}$$

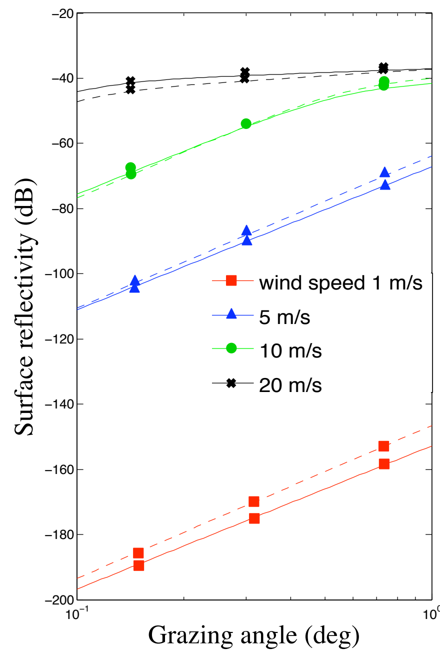

Figure 3.1: The sensitivity of GIT reflectivity per unit area $\sigma_{0,GIT}$ to grazing angle and wind speed at 3 GHz for horizontal (solid) and vertical (dashed) polarization.

where x is the horizontal Cartesian range, z is the altitude, and k is the wavenumber. ψ is the tangential electric field E_y for horizontal polarization, and the tangential magnetic field H_y for vertical polarization.

The maximum inter-element spacing of the synthetic array Δz is derived from the aliasing criterion in the parabolic equation model [22]:

$$\Delta z \leqslant \frac{\lambda}{2\sin(\alpha_{\max})} \,. \tag{3.6}$$

where $\alpha_{\max}$ is the cone angle of the valid parabolic equation approximation to the full field (see Section 3.5). Assuming plane wave propagation, the required number of array elements N_a to achieve the desired null-to-null beamwidth θ_{BW} according to the Rayleigh resolution limit is expressed as [139]:

$$N_a = \frac{\lambda}{\Delta z\, \theta_{BW}/2} \,. \tag{3.7}$$

To find the angular spectral distribution of the incoming electromagnetic wavefronts, the elements of each synthetic array should be properly phase shifted and added coherently.

One important assumption in the angular spectral distribution methods for finding the grazing angle is that the PE approximation should be valid for the full field.

Curved wave spectral estimation (CWS) is discussed next, followed by a summary of plane wave spectral estimation (PWS) as a special case of CWS. Curved wave spectral estimation handles curvature in wavefronts due to an inhomogenous medium. It is demonstrated that unlike PWS, CWS produces comparable results with ray theory irrespective of the refractivity gradient.

3.3.1 Wentzel-Kramers-Brillouin-Jeffreys approximation to wave propagation

The flat earth approximation is a modification to the atmospheric refractive index n_r which is equivalent to transforming the spherical propagation problem into a horizontal propagation one:

$$n_{\text{mod}} = n_r + \frac{z}{r_e}, \tag{3.8}$$

where n_{mod} is the modified refractive index and r_e is the radius of the Earth. Pekeris has shown that this transform often can be used for distances of up to half the Earth radius without incurring an error of more than 2% at any frequency [1]. The modified refractivity, M, is the part per million deviation from the refractivity index of a vacuum, defined as:

$$M = (n_{\text{mod}} - 1) \times 10^6 \, . \tag{3.9}$$

The Wentzel-Kramers-Brillouin-Jeffreys (WKBJ) approximation provides a locally plane wave solution in a lossless inhomogeneous medium assuming that the field solution $u(x, z)$ is separable: $u(x, z) = t(x)f(z)$. This approximation requires vertical variations of the vertical wavenumber $k_v(z)$ to be [140]:

$$\left| \frac{dk_v}{dz} \right| \ll \frac{k_v^2}{2\pi} \, . \tag{3.10}$$

The latter condition can be simplified in locally plane wave propagation to the condition that the medium should change slowly with respect to the wavelength. Similar conditions should hold as the wavenumber changes across the x direction. Vertical and horizontal refractivity index variations in almost all atmospheric conditions, including ducting situations, satisfy the aforementioned conditions. Hence, CWS is applicable to all practical cases in lower atmospheric propagation.

The vertical field $h(z)$ for one pair of incident and reflected wavefronts in the WKBJ solution is expressed as [140]:

$$h(z,\theta) = \frac{A_i}{\sqrt{k_v(z,\theta)}} e^{+j\int_{z_1}^{z} k_v(z,\theta)dz} + \frac{A_r}{\sqrt{k_v(z,\theta)}} e^{-j\int_{z_1}^{z} k_v(z,\theta)dz} \tag{3.11}$$

where A_i and A_r are constants of the incident and forward reflected fields, and z_1 denotes the sea surface. A_i and A_r are related by $A_r = \Gamma A_i$, where Γ is the forward reflection coefficient. The total vertical field $f(z)$ is a summation over multiple pairs of incident and reflected wavefronts at each range.

To find the surface reflection coefficient Γ in (4.6), we apply the Kirchoff approximation and model the effect of a rough sea surface. Based on the Miller-Brown-Vegh (MBV) model [105], an effective surface reflection coefficient can be expressed as a reduction ρ to the smooth surface Fresnel reflection coefficient Γ_0:

$$\gamma_w(\theta) = \frac{2\pi}{\lambda} h_w \sin\theta \; , \tag{3.12}$$

$$\rho(\theta) = e^{-2\gamma_w^2(\theta)} I_0 \left[2\gamma_w^2(\theta)\right] \; , \tag{3.13}$$

$$\Gamma(\theta) = \rho(\theta)\Gamma_0 \; . \tag{3.14}$$

Assuming an infinite sea surface impedance for both vertical and horizontal polarizations is a good approximation at microwave frequencies and small grazing angles [22]. Thus, $\Gamma_0 = -1$ for the field u. Above, I_0 is the modified Bessel function of the first kind, and h_w is the rms wave height from the Phillips ocean wave spectrum [106]:

$$h_w = 0.0051 v_w^2 \; , \tag{3.15}$$

where v_w is the wind speed in m/s. Computing Γ by (3.12–3.14) has been reported to agree well with measurements when $\gamma_w < 1.8$ [105,141].

An incident wavefront with wavenumber $k(z) = \frac{\omega}{c(z)} = \frac{\omega n_{\text{mod(z)}}}{c_0}$ arrives at height z with horizontal angle θ_z, angular frequency ω, and wave speed $c(z)$; c_0 is the electromagnetic wave speed in a vacuum. The horizontal wavenumber k_h is constant due to Snell's law:

$$k_h(z,\theta) = k(z)\cos\theta_z = k(z_1)\cos\theta \; , \tag{3.16}$$

where θ is the grazing angle at the surface. Hence, the vertical wavenumber is:

$$
\begin{aligned}
k_v(z,\theta) &= \sqrt{k^2(z) - k_h^2(z,\theta)} \\
&= \frac{\omega}{c_0}\sqrt{n_{\text{mod}}^2(z) - n_{\text{mod}}^2(z_1)\cos^2\theta}\,. \qquad (3.17)
\end{aligned}
$$

Vertical phase changes of the field are obtained by integration over the vertical wavenumber.

3.3.2 Curved wave spectral estimation

Consider the geometry in Fig. 3.2. Panel (a) shows the power diagram $|u|^2$ for an arbitrary antenna setting and a surface-based duct. Panels (b) and (c) show linear synthetic arrays along the z-axis with equal inter-element spacing Δz similar to the height grid size in the parabolic equation model.

Curved wave spectral estimation (CWS) is a method of non-planar angular spectral estimation that matches to the curvature of waves imposed by a variable refractivity index. This method is based on the WKBJ approximation to the electromagnetic wave propagation solution. An attempt to compensate for such curvature is derived in [142], where the reference point for phase shifts is chosen at the array element with minimum wave speed. Since the grazing angle at the sea surface is of interest, the reference point here is at the sea surface z_1. The geometry of CWS is similar to that of PWS with phase differences between array elements that are calculated by integration over the vertical wavenumber.

There are two assumptions in CWS: (1) the curvature of wavefronts is only due to vertical variation in refractivity, and (2) the refractivity index of the environment varies slowly with range. Two curved wave angular estimation equations are derived. The first only matches to incident wavefronts (denoted by $B_{\text{cws,1}}$), and the second matches both to incident and reflected wavefronts and yields a higher angular resolution (denoted by $B_{\text{cws,2}}$).

Assume that $\{u_l\}_{l=1}^{N_r}$ are N_r samples of the field obtained from a parabolic equation approximation to the electromagnetic wave propagation. N_r is the index of the last array element with k_v real, and it is upper bounded by N_a in (3.7). The phase difference between the reference and lth elements located at z_1 and z_l is obtained by integration of

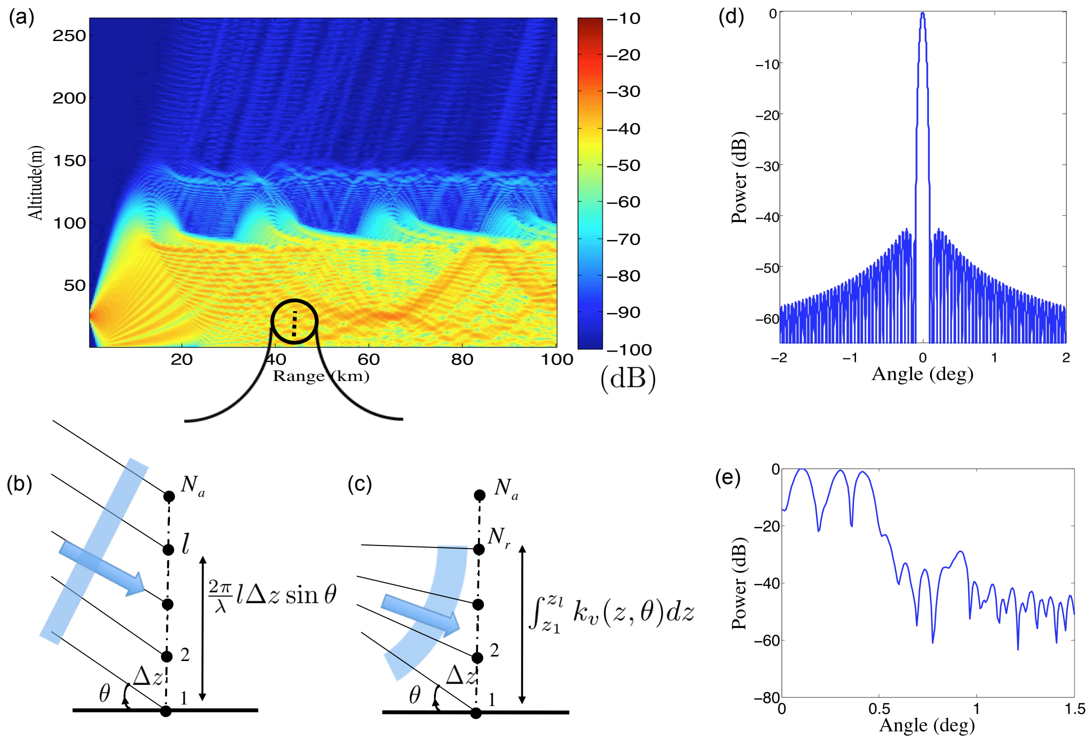

Figure 3.2: (a) Power $|u|^2$ (dB) from PE in an arbitrary surface-based duct. (b,c) Geometry of the line array used for the estimation of grazing angles at each range for plane and curved wave spectral estimation. (d) The spatial transfer function of a 200 element Hamming window with inter-element spacing of 5.7λ. (e) Normalized angular power spectrum $|B_{\text{CWS},1}(\theta)|^2$ for an arbitrary range (65 km) of Panel (a).

k_v along the vertical line joining the aforementioned points:

$$\phi_l(\theta) \quad = \quad \int_{z_1}^{z_l} k_v(z,\theta)dz \; . \tag{3.18}$$

The CWS output in direction θ is obtained by matching to the phase changes of the incident wavefront, seen in (4.6), assuming a grazing angle θ at the sea surface:

$$B_{\text{CWS},1}(\theta) = \sum_{l=1}^{N_r} w_l u_l e^{-j\phi_l(\theta)} \; , \tag{3.19}$$

where $l = 1$ corresponds to the array element index at the sea surface, u_l is the complex field at the lth element of the array obtained from the PE solution to the wave equation, and w_l is the corresponding window or shading coefficients. A Hamming window is used in this study as $\{w_l\}_{l=1}^{N_r}$ to weight array elements. The spatial transfer function of a Hamming window with 200 elements is shown in Fig. 3.2(d). Panel (e) shows the angular power spectrum as a function of grazing angle for an arbitrary range (65 km) of the example in Panel (a).

Using the field in the form of (4.6) for one pair of incident and reflected wavefronts, curved wave spectral estimation can be revised to match their sum for grazing angle θ:

$$B_{\text{CWS,2}}(\theta) \quad = \quad \sum_{l=1}^{N_r} w_l u_l \left(e^{-j\phi_l(\theta)} + \Gamma(\theta) e^{j\phi_l(\theta)}\right) \tag{3.20}$$

The synthetic array used in (3.20) is equivalent to using an array of twice the aperture where the lower half of the array virtually covers the reflected wavefront. Here we use half the Hamming window with maximum coefficient of 1 at the sea surface ($l = 1$) for $\{w_l\}_{l=1}^{N_r}$ in (3.20). This window is equivalent to a full Hamming window on the equivalent synthetic array of twice the aperture. Strictly speaking, using this window is appropriate only when $\Gamma = -1$. However, it yields satisfactory results for our examples. If $\Gamma(\theta)$ is uncertain or significantly different than -1 (high wind speeds and high frequencies), (3.19) is better to use to estimate the incident wavefront grazing angle.

3.3.3 Plane wave spectral estimation

Classical angular spectral estimation assumes plane wave propagation with a constant wave speed along the array. Plane and curved wave propagation are compared in Fig. 3.2(b) and (c). Plane wave spectral estimation is a special case of curved wave spectral estimation. Assuming a constant vertical wavenumber, (3.18) yields a constant phase advance of $\frac{2\pi}{\lambda}\Delta z \sin\theta$ between adjacent array elements with grazing angle θ. Thus, (3.19) becomes:

$$B_{\text{PWS,1}}(\theta) = \sum_{l=0}^{N_a-1} w_l u_l e^{-j\frac{2\pi l}{\lambda}\Delta z \sin\theta}\ , \tag{3.21}$$

where an aperture of N_a elements is considered. Matching to both incident and reflected wavefronts with grazing angle θ and a constant vertical wavenumber yields an expression similar to (3.20):

$$B_{\text{PWS},2}(\theta) = \sum_{l=0}^{N_a-1} w_l u_l (e^{-j\frac{2\pi l}{\lambda}\Delta z \sin\theta} + \Gamma(\theta) e^{j\frac{2\pi l}{\lambda}\Delta z \sin\theta}) \,, \tag{3.22}$$

where u_l and w_l are identical to those in CWS.

It has been shown that the assumption of plane wave propagation does not yield correct grazing angles comparable to ray tracing for an evaporation duct [21]. This is because the severe gradient and curvature of refractivity within the immediate vicinity of the sea-surface violates the assumption of plane wave propagation. CWS is intended to correct for this propagation curvature.

Fig. 3.3 shows the angular spectrum obtained using plane and curved wavefront assumptions. An evaporation duct is considered with duct height of 24 m, antenna height of 25 m, frequency of 10 GHz, and wind speed of 5 m/s. As expected, better angular resolution is obtained when both incident and reflected wavefronts are considered as opposed to considering only the incident wavefront.

Fig. 3.4 compares the performance of ray tracing, MUSIC, PWS (3.22) and CWS (3.20) to obtain grazing angles in an evaporation duct and antenna setting identical to those of Fig. 3.3. Panels (a) and (b) compare angular spectral estimation for wind speed of 5 m/s at 3 and 10 GHz, respectively. The aperture is fixed at 20 m for PWS and CWS for both frequencies. The MUSIC results are obtained from Temper [23]. Note that Temper uses ray tracing in the first 3 km even in its sole MUSIC mode for grazing angle calculation. Although both MUSIC and PWS are based on the plane wave propagation assumption, the MUSIC implementation in Temper is based on dividing the synthetic array into overlapping sub-arrays. Hence, a different set of grazing angles is obtained when the refractivity index varies considerably along the array.

Previous studies on evaporation ducts showed that grazing angles obtained by ray tracing and M-layer [143] converge to the same value in the microwave region [12]. M-layer is a computer code that finds propagating modes of radio waves in a stratified atmosphere above the sea surface. Fig. 3.4 shows the general agreement of grazing angles obtained from ray tracing and CWS. The disagreement of CWS and ray tracing at short ranges is due to the poor approximation of PE to the total field and spherical wavefronts coming from the source. CWS assumes the curvature of the wavefronts to

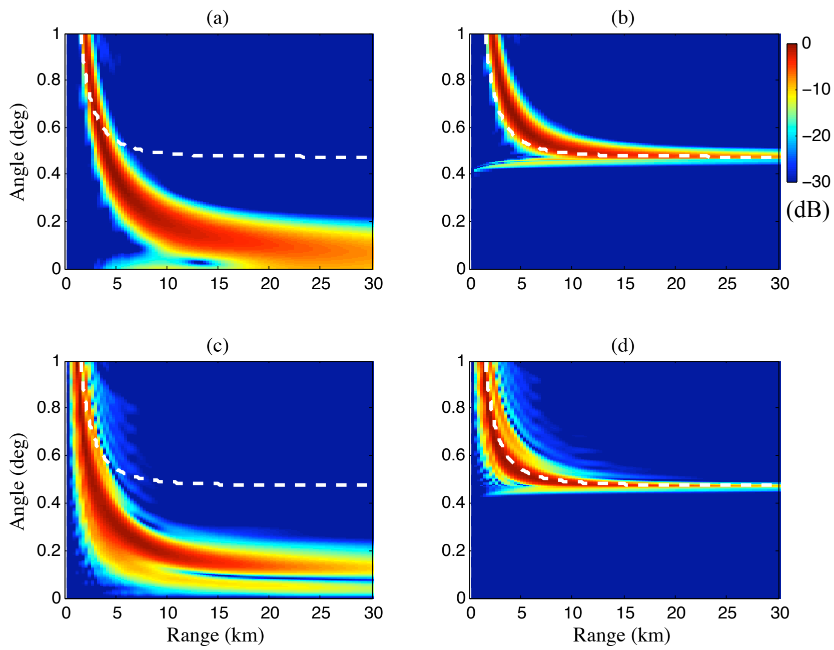

Figure 3.3: Angular power spectrum for a 24 m evaporation duct, antenna height of 25 m at 10 GHz, using: (a) plane wave spectral estimation $|B_{\text{PWS,1}}|^2$ (3.21), (b) curved wave spectral estimation $|B_{\text{CWS,1}}|^2$ (3.19), (c) $|B_{\text{PWS,2}}|^2$ (3.22), (d) $|B_{\text{CWS,2}}|^2$ (3.20). Dashed lines are grazing angles obtained from the ray theory. Higher angular resolution is obtained when both incident and reflected wavefronts are considered. In each case, the angular power spectrum is normalized by the maximum power over the whole range.

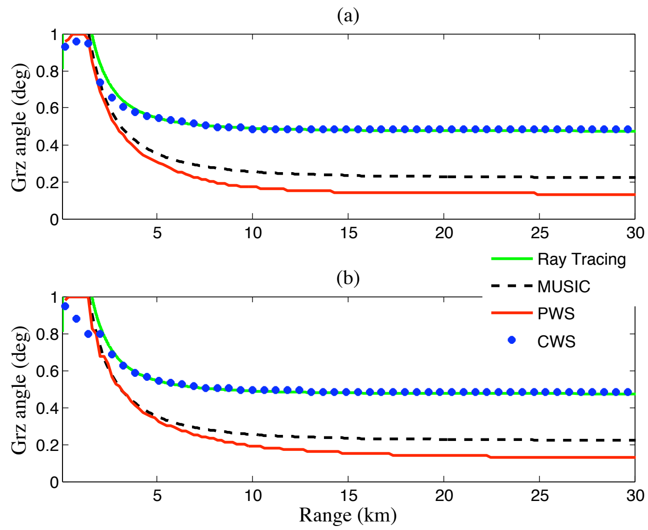

Figure 3.4: Grazing angle computed by ray tracing, MUSIC, PWS and CWS for an evaporation duct with duct height of 24 m and antenna height of 25 m at (a) 3 GHz, (b) 10 GHz. The synthetic aperture is 20 m for all cases.

be only due to a variable refractivity structure. This assumption breaks down near the antenna where spherical propagation dominates due to near field effects.

The disagreement between ray tracing (geometrical optics) and the plane wave propagation assumption was reported in [21]. Note that better angular estimation for PWS and MUSIC can be obtained by using a shorter array with less refractivity index variations. We use (3.20) and (3.22) in our simulations due to their higher angular resolution relative to (3.19) and (3.21) respectively. However, (3.19) and (3.21) also give similar results.

3.4 Multiple Grazing Angle Clutter

Ducted environments are leaky waveguides with the ocean behaving as a reflecting surface and the duct top behaving as a partially reflecting boundary. These waveguides carry more than one mode while different groups of modes interact with the surface with different equivalent grazing angles. It is shown in Fig. 3.1 that surface reflectivity changes up to 45 dB as grazing angle changes from 0.1 to 1° for wind speeds of less than 10 m/s. Therefore, a realistic model for sea surface clutter depends on the summation of surface reflections over all incident angles weighted by their corresponding powers.

Assume $\gamma(\theta) = |B_{\text{cws}}(\theta)|^2$ to be the angular power spectrum obtained from (3.19) or (3.20). Considering the single grazing angle clutter model (4.3) and weighting the clutter power along each angle θ by the normalized power $\frac{\gamma(\theta)}{\int_\theta \gamma(\theta)}$ yields the multiple angle clutter model:

$$P_c(r) = \frac{\alpha_c(r) F^4(r)}{\int_\theta \gamma(\theta) d\theta} \int_\theta \frac{\sigma_{0,GIT}(\theta) \sec(\theta) \gamma(\theta)}{F^4_{std}(\theta)} d\theta \; , \tag{3.23}$$

where $F_{std}(\theta)$ is the propagation factor of the standard atmosphere at $r'(\theta)$ from (3.3), and $\alpha_c(r) = \frac{P_t G^2 \lambda^2 \theta_B c\tau}{2(4\pi r)^3 L}$ includes all the terms independent of θ. It has been suggested to use propagation factors at the height of 1 m to avoid cancellation of the total field at the conductor surface [87]. However, that choice of the propagation factor may lead to an error in the calculation of the clutter power. This error is negligible in most practical situations [109].

The procedure to compute the clutter power for a given refractivity profile is summarized below. Sea surface reflectivity equations are provided in Appendix 3.6.

1. Run a parabolic equation model to obtain the field $u(x, z)$ for the desired range extent and given environment. The inter-element spacing is obtained from (3.6), and the number of array elements is obtained from (3.7).

2. For each range, construct a vertical synthetic array from the PE FFT bins.

3. Using (3.12–3.14) find the surface reflection coefficient $\Gamma(\theta)$ for all angles. Then, use (3.18) and (3.20) to obtain the angular distribution.

4. Use (3.2), (3.27) or (3.28) depending on the polarization to obtain sea surface reflectivity values for different grazing angles.

5. Calculate the total clutter power by (5.2) which uses the angular power spectrum and sea surface reflectivities from Steps 2 and 3.

3.5 Examples

Electromagnetic wave propagation examples in different ducting environments are considered here. The simulated radar in the examples operates at 3 and 10 GHz, vertically polarized with elevation angle of $0°$ and half-power beamwidth of $0.4°$. The radar antenna is located 25 m above the sea surface and wind speed is 5 m/s.

The clutter powers due to both single and multiple grazing angle models are normalized to the power at the range of 10 km (except the example of the evaporation duct which is normalized at 5 km), so that clutter power changes of different models can be compared conveniently. For the multiple grazing angle model in (5.2), we use (3.20) for CWS and (3.22) for PWS due to their higher angular resolutions relative to (3.19) and (3.21), respectively. However, the latter also gives similar results.

The parabolic equation yields valid solutions for wave propagation inside a cone with vertex angle $\alpha_{\max}$ [22], here $\alpha_{\max} = 5°$. This angle is a trade-off between PE stability and accuracy. The complex field (PE solution), ray tracing results and maximum ray tracing clutter calculations are obtained from APM [20]. APM is a hybrid model that consists of four sub-models: flat earth, ray optics, extended optics, and the split-step PE model. The PE model within APM is the primary model from which all other sub-models are driven [20]. All examples described in this section are based on executing only the PE algorithm within APM. The forward scattered field of APM is obtained by using maximum angle of ray traces for surface impedance calculations at each range, i.e. the spectral method described here has not been used.

APM also computes clutter based on the modified GIT reflectivity model described in Section 3.2.1. For over-water propagation paths, such as the examples presented in this section, APM determines the grazing angle based on ray tracing. It performs a combination of interpolation and elimination to determine the maximum grazing angle over a given range for those cases where ducting is present and grazing angles determined by ray tracing will result in "multi-valued" grazing angles for a particular range interval. The maximum grazing angles determined from ray tracing, and used within APM for clutter computations are shown for an example in Fig. 3.8(c).

The theoretical bound (3.6) yields $\Delta z \leqslant 0.172$ m for 10 GHz and $\Delta z \leqslant 0.573$ for 3 GHz. The upper bounds are used here in each case. The CWS output is restricted to grazing angles of 0 to $1.5°$. A 20 m aperture is used at 10 GHz which gives a null-to-null beamwidth of 0.17° for a rectangular window. The same resolution condition requires a 67 m synthetic aperture at 3 GHz, which usually is not possible since the aperture is limited by the duct height in this work.

3.5.1 Evaporation Ducts

Evaporation ducts are the most common types of non-standard atmospheric phenomena in maritime environments. The Paulus-Jeske model provides a relationship between modified refractivity M, altitude z and duct height h_d [68]. Assuming equal temperature of the sea surface and air layer boundary simplifies the Paulus-Jeske model [12]:

$$M(z) = M_0 + c_0(z - h_d \ln \frac{z + h_0}{h_0}) \, , \tag{3.24}$$

where M_0 is the base refractivity usually taken as 300 M-units, $c_0 = 0.13$ M-unit/m is the linear slope of the refractivity and h_0 is the roughness factor taken as 1.5×10^{-4} m.

Fig. 3.5 compares the output power of CWS, $\gamma(\theta)$, and grazing angles computed by ray tracing for different ranges in an evaporation duct with duct height of 24 m and operational frequency of 10 GHz. The radar is located at 25 m from the sea surface. Calculated clutter power obtained from different methods also is shown.

Panel (a) shows the refractivity profile similar to [21] where MUSIC [24] was reported to fail capturing the correct grazing angles. Panel (b) shows the propagation factor, in dB, of the environment with radar conditions as described before. Panel (c) shows the angular power spectrum of CWS overlaid with grazing angles obtained from ray tracing. It shows that the peaks of CWS coincide with the ray tracing results.

CWS is performed on the PE complex field with an array of size 20 m and inter-element spacing of $\Delta z = 0.17$ m. Agreement of CWS and ray tracing is clear in Fig. 3.5(c). Panel (d) shows the clutter power obtained from a single grazing angle using maximum ray tracing and the multiple grazing angle model using CWS and PWS. Single angle ray tracing and multiple angle CWS result in similar clutter patterns due to the single grazing angle nature of evaporation ducts. The multiple grazing angle model that utilizes PWS has a different rate of fall-off. This will result in erroneous duct height estimation in inversion problems since the rate of fall-off of the clutter power is

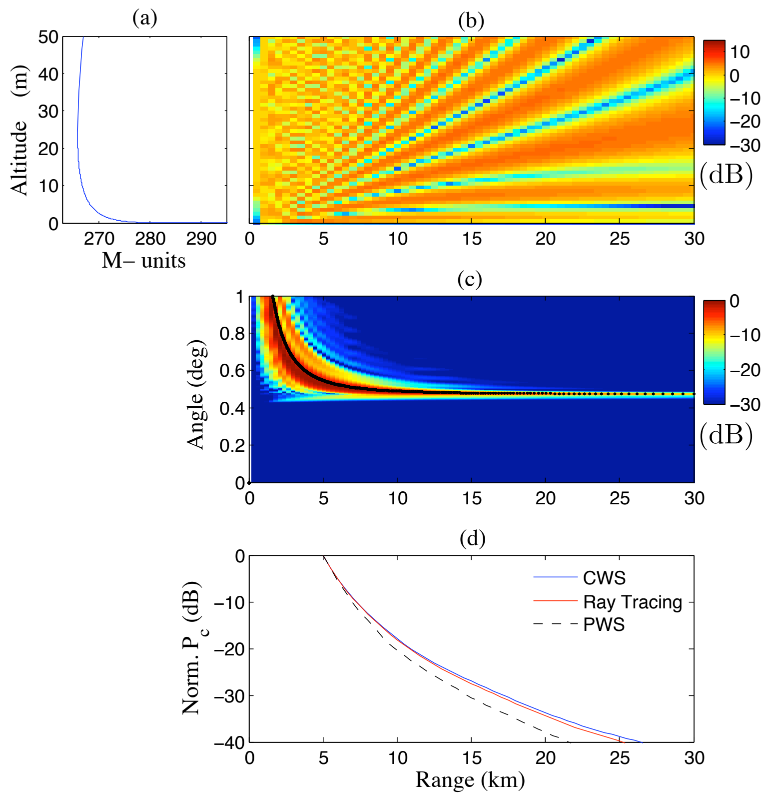

Figure 3.5: (a) M-profile of an evaporation duct with $h_d = 24$ m. (b) Propagation factor F in dB for 10 GHz. (c) Output power of CWS normalized by the maximum power over the whole range, compared to the grazing angle computed by ray tracing (solid). (d) Clutter power calculated by maximum ray tracing and the multiple grazing angle model (CWS, PWS).

a function of duct height in evaporation ducts [17].

The reliability of CWS is tied to the reliability of the field calculated by PE. Fig. 3.5 shows that angular spectral estimation yields comparable results to ray tracing where PE is a valid approximation to the full field and curved wavefronts are not due to near field spherical propagation.

3.5.2 Surface-Based Ducts

Surface ducts occur when humidity and temperature inversions are both present which typically is due to the advection of warm and dry coastal air to the sea. These ducts are less common than evaporation ducts but their effect is more prominent on radar returns [1]. The M-profile of a range-independent surface based duct can be approximated by a bilinear or tri-linear function (depending on the structure of the refractivity profile):

$$M(z) = M_0 + \begin{cases} c_1 z & z \leqslant h_1 \\ c_1 h_1 + c_2(z - h_1) & h_1 \leqslant z \leqslant h_2 \\ c_1 h_1 + c_2 h_2 & h_2 \leqslant z \\ \quad +0.118(z - h_1 - h_2)\,. & \end{cases} \tag{3.25}$$

Refractivity changes along the array in the examples shown in Figs. 3.6–3.8 are small such that curvature of wavefronts along the array is negligible. Hence, MUSIC and CWS will obtain similar angles. Fig. 3.6 shows an example of a surface based duct taken from [21] with radar frequency of 10 GHz and antenna height 25 m to show the agreement of CWS with previous studies. As used in [21], MUSIC with forward/backward smoothing [137] assumes a constant refractivity index by averaging over overlapping sub-arrays. The panels are similar to those of Fig. 3.5.

Ray tracing does not always result in smooth variations of calculated grazing angles. Fig. 3.7(a) is an example where ray tracing results in discontinuities while CWS results in smooth grazing angle estimation without any further processing and extra assumptions. This continuity results in a continuos clutter power, as seen in Fig. 3.7(b). The refractivity profile and radar conditions are all similar to Fig. 3.6 except that the operational frequency is at 3 GHz and antenna height is 45 m. Interpolation methods such as greatest angle path (GAP) have been developed that yield relatively continuous grazing angles biased toward larger ray trace angles [25]. However, these methods were developed to keep the single grazing angle smooth and are not necessarily correct physically.

An example of multiple arrivals with comparable power is provided in Fig. 3.8 where a surface-based duct is used with the refractivity profile shown in Panel (a). All radar simulation parameters are similar to the other examples. Using only one of the ray traces as the grazing angle is not representative of the incident wave. However, angular spectral estimation captures all incident angles and their corresponding relative powers. Panel (c) shows that multiple grazing angles are present where none is dominant. Using the maximum grazing angle may result in an unrealistic dynamic range of the clutter

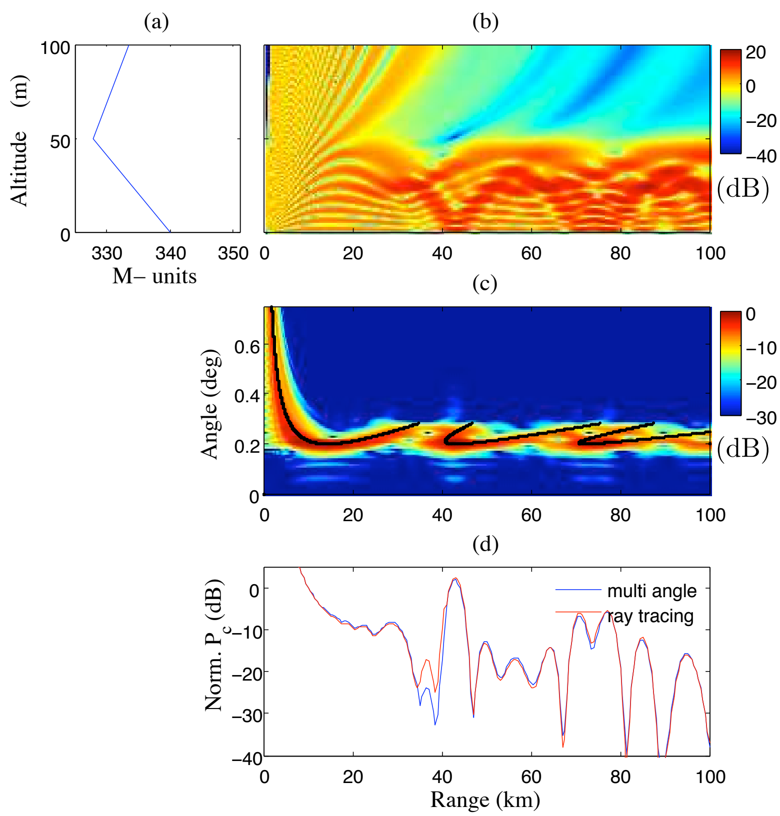

Figure 3.6: (a) M-profile of a surface-based duct. (b) Propagation factor F in dB for 10 GHz. (c) CWS output power normalized by the maximum power over the whole range, overlaid with grazing angles obtained from ray tracing (solid). (d) Clutter power from maximum ray tracing and the multiple grazing angle model.

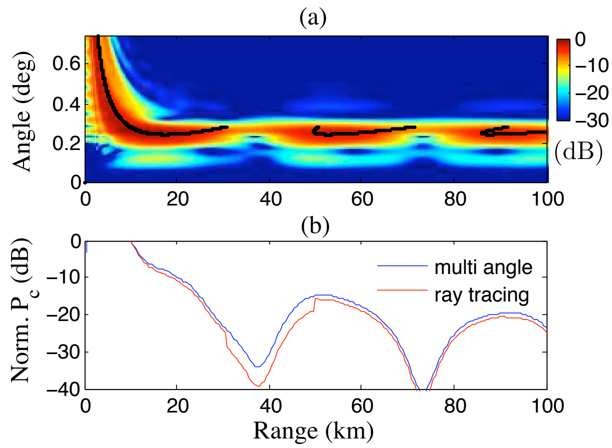

Figure 3.7: Discontinuity in clutter power when grazing angle is obtained from ray tracing. Similar refractivity profile and conditions as in Fig. 3.6 except that antenna height and frequency are 45 m and 3 GHz. (a) CWS output power normalized by the maximum power over the whole range, overlaid with grazing angle obtained from ray tracing (solid). (b) Multiple angle clutter power based on CWS and single angle clutter based on ray tracing.

power, as observed in Panel (d).

3.5.3 SPANDAR 1998 Measured Refractivity

A refractivity profile measured during the Space Range Radar (SPANDAR) experiment, Wallops Island, Virginia, April 2, 1998 [12,13] is considered here. This profile was measured using an instrumented helicopter provided by the Johns Hopkins University Applied Physics Laboratory. The particular refractivity profile used here is from Run 07, at a range of 59 km from the SPANDAR.

Fig. 3.9 is an example using real refractivity profile measurements that shows agreement of angular spectral estimation using CWS and grazing angles obtained from ray theory.

3.6 Conclusion

A multiple grazing angle clutter model based on curved wave spectral estimation (CWS) has been introduced. CWS is a generalization of plane wave spectral estimation

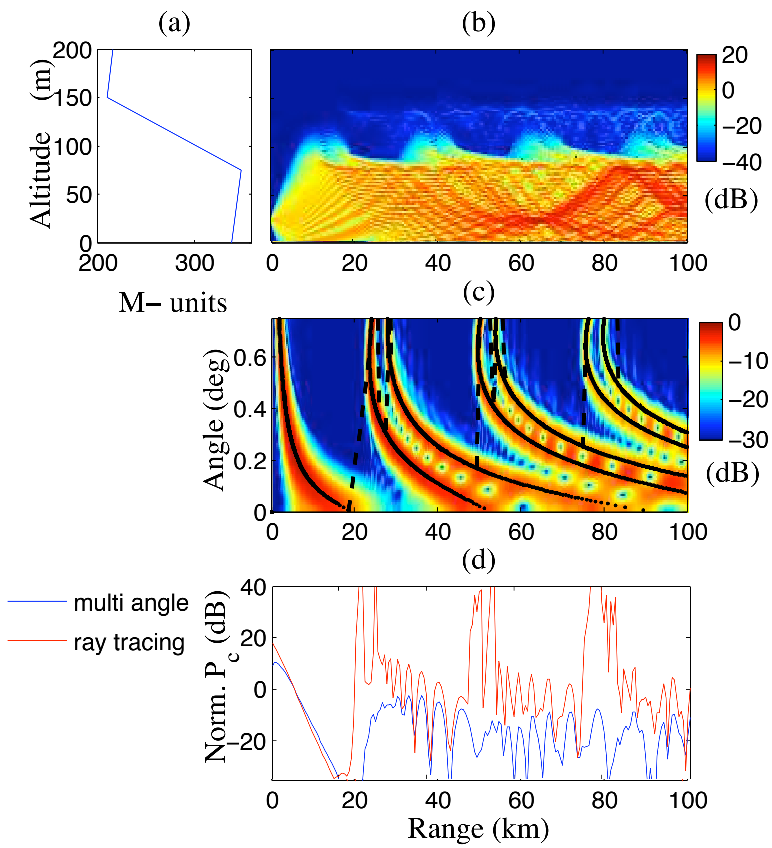

Figure 3.8: (a) M-profile of a surface-based duct. (b) Propagation factor F in dB for 10 GHz. (c) CWS output power normalized by the maximum power over the whole range, overlaid with grazing angles obtained from ray tracing (solid) and maximum of ray traces (dashed). (d) Clutter power from maximum ray tracing and the multiple grazing angle model based on CWS.

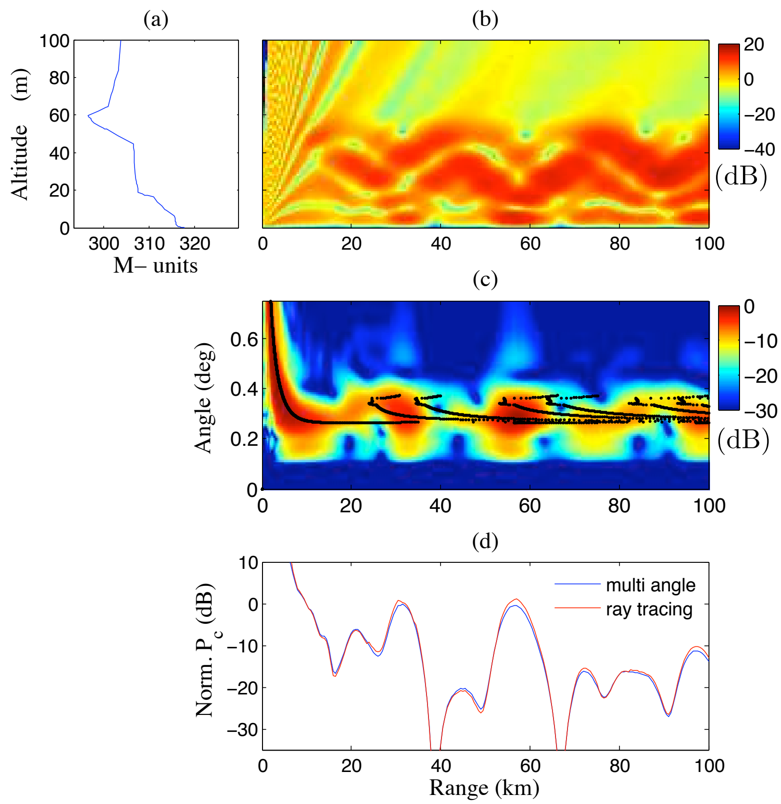

Figure 3.9: (a) M-profile measured during the SPANDAR 1998 experiment. (b) Propagation factor F in dB for 3 GHz. (c) CWS output power normalized by the maximum power over the whole range, overlaid with grazing angles obtained from ray tracing (dark line). (d) Clutter power from maximum ray tracing and the multiple grazing angle model.

(PWS) where curvature of wavefronts due to changes in the refractivity index is considered. Examples demonstrated that the power versus grazing angle obtained by CWS is more accurate than PWS and it does not have the problem of discontinuity in grazing angles introduced by ray tracing.

The multiple grazing angle clutter model integrates over all grazing angles weighted by the angular power spectrum. Grazing angles can be determined by CWS from a synthetic vertical array generated by samples of the field. These samples are obtained from a parabolic equation propagation model. The performance of this clutter model was compared to that of single grazing angle clutter calculations for evaporation and surface-based ducts. This method yields a more realistic model for the received clutter that then can be used in estimation of the refractivity profile of the ambient environment based on the observed backscattered radar signal. Although the multiple grazing angle clutter model has been derived for sea clutter, it also can be adapted for land clutter.

appendix: GIT model

Sea surface reflectivity computation in this work is based on the Georgia Institute of Technology (GIT) model [112]. Reilly and Dockery modified the GIT model to incorporate the atmospheric condition influence on the sea surface reflectivity [42,87,138].

The basic GIT model calculates the sea surface reflectivity per unit area of vertical and horizontal polarizations by considering an average wave height in a given sea condition and taking into account the radar look direction [112]:

$$h_{av} = 0.00425 v_w^{2.5} , \tag{3.26}$$

where h_{av} is the average wave height in meters, and v_w is the wind speed in m/s. Defining:

$$a = (14.4\lambda + 5.5)\theta \frac{h_{av}}{\lambda}$$
$$q = 1.1(\lambda + 0.015)^{0.4} ,$$

in which λ is the wavelength in meters, and θ is the grazing angle in radians. Then:

$$G_a = \frac{a^4}{a^4+1}$$
$$G_M = \exp\{0.2(1-2.8\theta)(\lambda+0.015)^{-0.4}\cos\psi\}$$
$$G_w = (\frac{1.94v_w}{1+v_w/15.4})^q \ ,$$

where ψ is the angle between the antenna look direction and the wind direction. The GIT sea surface reflectivity model is:

$$\sigma_{0h,GIT} = 10\log(3.9\times10^{-6}\lambda\theta^{0.4}G_aG_MG_w) \tag{3.27}$$

$$\sigma_{0v,GIT} = \begin{cases} \sigma_{0h,GIT} - 1.73\ln(h_{av}+0.015) \\ \ +3.76\ln(\lambda) + 2.46\ln(\theta+0.0001) \\ \ +22.2 \qquad \text{1 to 3 GHz} \\ \sigma_{0h,GIT} - 1.05\ln(h_{av}+0.015) \\ \ +1.09\ln(\lambda) + 1.27\ln(\theta+0.0001) \\ \ +9.70 \qquad \text{3 to 10 GHz,} \end{cases} \tag{3.28}$$

where $\sigma_{0h,GIT}$ and $\sigma_{0v,GIT}$ are the sea surface reflectivities per unit area for H and V polarizations obtained from the GIT model, in dB. The effect of the angle between the radar look direction and wind direction is an additive bias term as $\cos\psi$ in the sea surface reflectivity.

Acknowledgments

Contents of Chapter 3 were published as: A. Karimian, C. Yardim, P. Gerstoft, W. .S. Hodgkiss, Amalia Barrios, “Multiple grazing angle sea clutter modeling”, *IEEE Trans. Antennas Propagat.*, vol. 60, no. 90, pp. 4408-4417, September 2012.

Chapter 4

Estimation of radio refractivity using a multiple angle clutter model

4.1 Introduction

Lower atmospheric ducts over the ocean are common in many maritime regions of the world. These non-standard conditions create effects such as significant variations in the maximum operational radar range, creation of radar fades where the radar performance is reduced, and increased sea clutter [1]. Atmospheric ducts are more common in hot and humid regions of the world. The Persian Gulf, the Mediterranean and California coasts are examples of such regions with common formation of a ducting layer above the sea surface [17].

Surface-based ducts appear almost 25% of the time off the coast of South California and 50% in the Persian Gulf [41]. Efforts in remote sensing and numerical weather prediction have been directed toward a better estimation of the refractivity profile in the lower atmosphere (less than 500 m above the sea surface) [6,136]. The atmospheric refractivity profile is often measured by direct sensing of the environment. Rocketsondes and radiosondes typically are used for in situ sampling of the surface layer [44]. Lidar [55] and GPS signals [10] also have been used to measure the vertical refractivity profile.

A more recent approach, refractivity from clutter (RFC), uses the radar return signals to estimate the ambient environment refractivity profile [12–14,18,56,88]. This approach makes tracking of spatial and temporal changes in the environment possible [15].

Most previous RFC studies have considered a grazing angle-independent clutter model. This model is a consequence of neglecting the effect of a variable grazing angle on the clutter power at low angles [13,90], or the convergence of angles at far ranges. Convergence of the grazing angle at far ranges is valid for a range-independent evaporation duct [12,17].

Grazing angle is range-dependent in ducted environments. In addition, multiple angles of arrival at each range typically are present in strong surface-based ducts (e.g. see Fig. 4.1c) [18,26]. Thus, neglecting changes of the grazing angle along the propagation path, or assuming single path propagation does not yield a realistic clutter model in ducted environments. [78] and [14] have considered horizontal variability of the sea surface reflectivity, albeit considering it as a random process.

The present study uses two approaches to include the grazing angle information: a range-dependent single angle clutter model that is based on the maximum grazing angle at each range, and a range-dependent multiple angle clutter model that is based on all angles of arrival. The worst case clutter in maritime environments can be calculated by considering the maximum grazing angle at each location [20,25]. However, this model is not appropriate for RFC applications where a more realistic model for the expected clutter is required. The multiple angle clutter model incorporates all incident wavefronts and weights them proportional to their relative powers [26].

4.2 Sea clutter at low grazing angles

Radars operating in maritime environments encounter a back-scattered field from the sea surface which depends on the refractivity profile of the environment known as the M-profile. This dependence makes inference on the refractivity profile from the observed clutter possible [13]. The expected clutter at range r is expressed as [87]:

$$P_c(r) = \frac{P_t G^2 \lambda^2 \theta_B c \tau \sigma_0 \sec(\theta) F^4(r)}{2(4\pi r)^3 L}\ , \tag{4.1}$$

where P_t is the transmitter power, G is the antenna gain, λ is the wavelength, θ_B is the antenna pattern azimuthal beamwidth, c is the propagation speed, τ is the pulse width, σ_0 is the sea surface reflectivity per unit area, θ is the grazing angle at range r, F is the propagation factor, and L is the total assumed system losses.

The pattern propagation factor F is defined as the ratio of the magnitude of the electric field at a given point under specified conditions to the magnitude of the electric field under free-space conditions with the beam of the transmitter directed toward the point in question [61]: $F(r) = \frac{|E(r)|}{|E_{fs}(r)|}$.

A review of the three models of clutter power that are used in this study is provided below.

4.2.1 Grazing angle independent clutter model

The dependence of the sea surface reflectivity on the grazing angle has not been included in most previous RFC studies [13,56]. This assumption results in a range-independent sea surface reflectivity term in the clutter power equation. The $\sec(\theta)$ term also is a weak function of θ at low grazing angles. Thus, normalizing the clutter power with reference to the power at range r_o yields the approximation:

$$\frac{P_c(r)}{P_c(r_o)} \simeq \left(\frac{r_o}{r}\right)^3 \frac{F^4(r)}{F^4(r_o)} \,. \tag{4.2}$$

The propagation factor F can be obtained from a parabolic equation (PE) code [80]. The assumption of an angle-independent sea surface reflectivity is valid where grazing angle does not significantly vary with range.

4.2.2 Range-dependent single grazing angle clutter

The clutter power typically is estimated based on a single grazing angle of an incident wavefront at each range. The grazing angle can be estimated from ray theory [20] or from angular spectral estimation techniques, such as MUSIC, that calculate the angle of arrival [23]. Both of these methods might yield several grazing angles at each range. Usage of the maximum grazing angle at each location leads to the worst case clutter power. This is a conservative estimate of the expected clutter power that is used in radar performance analysis. However, ray tracing has its own limitations. There are surface locations that rays do not reach, requiring interpolation or extrapolation of grazing angles at those ranges.

The sea surface reflectivity σ_0 is dependent on the grazing angle θ. In practice it is common to use the semi-empirical sea surface reflectivity model from the Georgia Institute of Technology (GIT) [112]. GIT is based on fitting the experimental measured average surface reflectivity to a function of polarization, radar frequency, grazing angle, wind speed and radar look direction [87]. It is assumed that the GIT model is based on measurements obtained under standard atmospheric conditions. This model also depends on a single grazing angle. [138] modified the GIT model to take into account the effects of non-standard ducting conditions on sea clutter. They divided the GIT surface reflectivity by the standard atmosphere propagation factor to remove the standard atmospheric effect on the measurements. Derivation of surface reflectivity models at low grazing angles continue to be an active field of research [115]. Using the modified GIT sea surface reflectivity model, the clutter power equation is obtained as:

$$P_c(r) = \frac{P_t G^2 \lambda^2 \theta_B c \tau \sigma_{0,GIT}(r) \sec(\theta) F^4(r)}{2(4\pi r)^3 L F^4_{std}(r')} \,, \tag{4.3}$$

where $F^4_{std}(r')$ is the two-way propagation factor of a standard atmosphere ($\frac{dM}{dh} = 0.118$ M-units/m) at range r' with the same wind speed and an isotropic antenna. r' is the range corresponding to the grazing angle θ in the standard atmosphere with an identical radar height and an isotropic antenna.

4.2.3 Range-dependent multiple grazing angle clutter

Angular spectral estimation techniques find the incident power distribution versus grazing angle at each range. The elements of the vertical synthetic array (Fig. 4.1a) are formed from the complex field u at each range obtained from the FFT bins of the electromagnetic parabolic equation (PE) propagation model. For Cartesian coordinates [22]:

$$u(x, z) = e^{-jkx} \psi(x, z) \,, \tag{4.4}$$

where x is the horizontal Cartesian range, z is the altitude, and k is the wavenumber. ψ is the tangential electric field E_y for horizontal polarization, and the tangential magnetic field H_y for vertical polarization.

A multiple angle clutter model based on curved wave spectral estimation (CWS) [26] is considered in this work. CWS is a non-plane wave spectral estimation technique based on the Wentzel-Kramers-Brillouin-Jeffreys (WKBJ) approximation to the electromagnetic wave propagation solution. The WKBJ approximation provides a solution in a lossless inhomogeneous medium assuming that the field solution $u(x,z)$ is separable: $u(x,z) = t(x)f(z)$. This approximation requires the vertical wavenumber $k_v(z)$ to be slowly varying along the coordinate system [140]. The latter condition can be simplified in plane wave propagation to the condition that the medium changes slowly with respect to the wavelength. The vertical field $f(z)$ is a summation of multiple pairs of incident and reflected wavefronts. The field due to each pair of wavefronts with angle θ at the surface in the WKBJ approximation is expressed as [140]:

$$\begin{aligned} h(z,\theta) &= \frac{A_i}{\sqrt{k_v(z,\theta)}} e^{+j\int_{z_1}^{z} k_v(z,\theta)dz} \\ &+ \frac{A_r}{\sqrt{k_v(z,\theta)}} e^{-j\int_{z_1}^{z} k_v(z,\theta)dz}, \end{aligned} \tag{4.5}$$

where A_i and A_r are constants of the incident and forward reflected waves, and z_1 denotes the sea surface. A_i and A_r are related by $A_r = \Gamma A_i$ with Γ the reflection coefficient. Assuming $\Gamma = -1$, (4.5) is simplified:

$$h(z,\theta) = \frac{A_i}{\sqrt{k_v(z,\theta)}} \left(e^{+j\int_{z_1}^{z} k_v(z,\theta)dz} - e^{-j\int_{z_1}^{z} k_v(z,\theta)dz} \right) . \tag{4.6}$$

The geometry of CWS is shown in Fig. 4.1b. Spatial samples of the PE field are used along a vertical line array. CWS matches to the phase variations of different array elements based on the WKBJ solution. An inherent assumption in CWS is that the curvature of wavefronts is only due to an inhomogeneous medium.

Let the medium have a stratified structure with the modified atmospheric refractive index $n_{mod}(z)$ at each range r and height z. The modified refractive index is obtained by $n_{mod}(z) = n_r(z) + \frac{z}{r_e}$ from the atmospheric refractive index $n_r(z)$ and earth radius r_e, which is a flat earth approximation to the spherical propagation problem.

The vertical wavenumber k_v is a function of the wavenumber k, the horizontal wavenumber k_h, and gazing angle θ. Let ω denote the angular frequency, and c_0 the

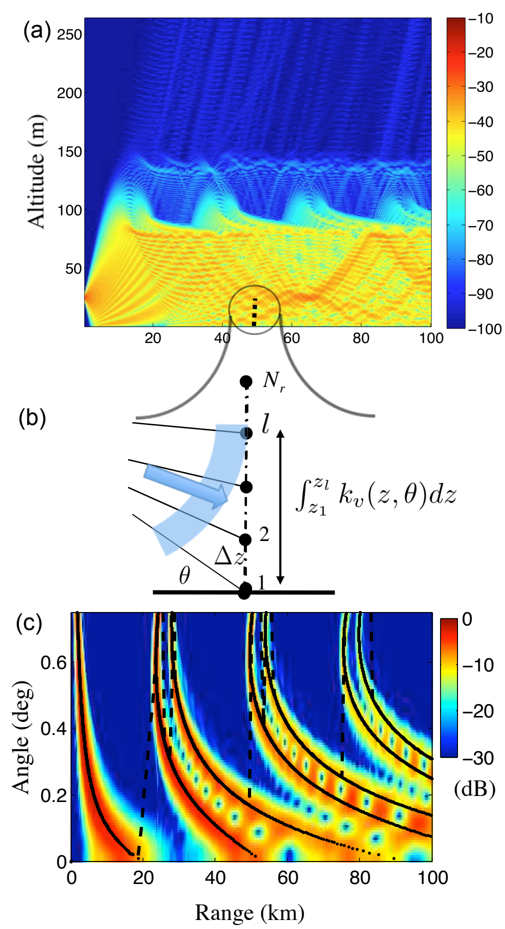

Figure 4.1: (a) Power $|u|^2$ (dB) from the parabolic equation (PE) propagation model in an arbitrary surface-based duct similar to the profile of Fig. 4.2c. (b) Geometry of the line array used for the estimation of grazing angles at each range for curved wave spectral estimation. (c) Angular spectral power (contour plot), grazing angle from ray tracing (solid), the maximum angle from ray tracing (dashed).

wave speed in a vacuum. Applying Snell's law for k_h yields:

$$\begin{aligned} k_v(z,\theta) &= \sqrt{k^2(z) - k_h^2(z,\theta)} \\ &= \frac{\omega}{c_0}\sqrt{n_{\text{mod}}^2(z) - n_{\text{mod}}^2(z_1)\cos^2\theta}\,. \end{aligned} \tag{4.7}$$

With k_v real, the phase difference between z_1 and z_l is obtained by integration of k_v along the vertical line joining the aforementioned points:

$$\phi_l(\theta) = \int_{z_1}^{z_l} k_v(z,\theta)dz\,. \tag{4.8}$$

The CWS output in direction θ is obtained by matching to the phase variations of array elements for a pair of incident and reflected wavefronts with angle θ, expressed in (4.6):

$$\begin{aligned} B_{\text{cws}}(\theta) &= \sum_{l=1}^{N_r} w_l u_l \left(e^{-j\phi_l} - e^{j\phi_l}\right) \\ &= -2j\sum_{l=1}^{N_r} w_l u_l \sin\left(\int_{z_1}^{z_l} k_v(z,\theta)dz\right)\,, \end{aligned} \tag{4.9}$$

where u_l is the PE field at the lth element of the array and w_l are the weighting coefficients of the array, here half a Hamming window. This is equivalent to using a Hamming window on a double size array that covers the incident and reflected wavefronts separately [26]. N_r is the index of the highest array element with $k_v \geqslant 0$.

Fig. 4.1c shows an example that exhibits variable grazing angles. Panels (a) and (c) are based on computations from an environment with a refractivity structure similar to Fig. 4.2c. Fig. 4.1c shows that in a range-independent surface-based duct, constant or single grazing angle assumptions are not necessarily valid. Also, most practical situations include a range varying refractivity profile [13] where a range-independent grazing angle assumption is no longer valid. Inversion of a range-dependent evaporation duct is studied in Section 4.3.2.

The angular spectral power $\gamma(\theta) = |B_{\text{cws}}(\theta)|^2$ is obtained from (4.9). $\gamma(\theta)$ can be used to decompose the total power into the power arriving from different directions. The multiple angle clutter model is obtained as:

$$P_c(r) = \frac{\alpha_r F^4(r)}{\int_\theta \gamma(\theta)d\theta}\int_\theta \frac{\sigma_{0,GIT}(\theta)\sec(\theta)\gamma(\theta)}{F_{std}^4(\theta)}d\theta\,, \tag{4.10}$$

where $\alpha_r = \frac{P_t G^2 \lambda^2 \theta_B c\tau}{2(4\pi r)^3 L}$ includes all θ independent terms.

The multiple angle clutter model (4.10) can be visualized by assuming a discrete set of N_θ grazing angles. Using spectral estimation, incident power at each range can be decomposed into its angular components $\{\gamma(\theta_i)\}_{i=1}^{N_\theta}$. Consider the weighted propagation factor associated with grazing angle θ_i to be defined by:

$$F_i^2(r) \triangleq F^2(r) \frac{\gamma(\theta_i)}{\sum_{n=1}^{N_\theta} \gamma(\theta_n)} \; . \tag{4.11}$$

Incident power is assumed to be back-scattered uniformly. Due to reciprocity, back-scattered angles received by the radar are identical to the incident angles at the same range. Thus, the total clutter power is:

$$\begin{aligned} P_c(r) &= \sum_{i=1}^{N_\theta} \alpha_r F_i^2(r) \sigma_0(\theta_i) \sec(\theta_i) \sum_{j=1}^{N_\theta} F_j^2(r) \\ &= \sum_{i=1}^{N_\theta} \alpha_r F^2(r) F_i^2(r) \sigma_0(\theta_i) \sec(\theta_i) \; . \end{aligned} \tag{4.12}$$

Substituting (4.11) into (4.12) yields the discrete form of (4.10). Here, we have assumed different propagation paths to be uncorrelated.

Fig. 4.2 compares clutter power obtained from the previously mentioned models. Left panels show the refractivity profiles of the modeled environment, and right ones show the corresponding clutter power at 3 GHz, vertical polarization, antenna beamwidth of 0.4°, antenna height of 15 m and wind speed of 5 m/s. All clutter power plots are normalized with reference to the starting range (10 km for the surface-based duct example and 3 km for evaporation duct examples).

Fig. 4.2a shows a range-independent evaporation duct with duct height of 24 m. Differences between the fall-off rates of angle dependent and independent models are due to rapid variations of the grazing angle in the vicinity of the radar. Most previous RFC studies considered the clutter power at ranges where grazing angle does not vary significantly with range. For evaporation ducts, this region is shown in Fig. 1 of [17]. However, this usually means avoiding the region in the vicinity of the radar where clutter to noise ratio is high. Panel (c) shows a surface-based duct. Its corresponding clutter power obtained from the maximum angle of ray tracing shows larger dynamic range

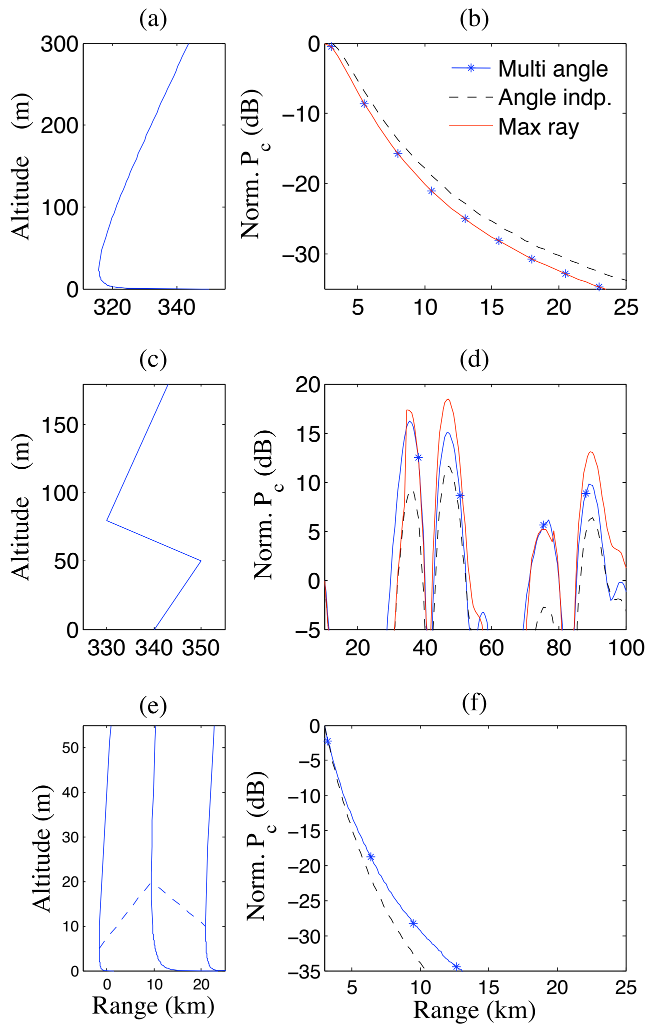

Figure 4.2: Left panels: refractivity profile, right panels: corresponding clutter power at 3 GHz using various clutter models: multiple grazing angle, angle independent, and maximum angle from ray tracing.

and discontinuities at boundaries of ray theory shadow zones. Panel (e) shows a range-dependent evaporation duct which is discussed further in Section 4.3.2. The modeled clutter power, assuming angle dependent sea surface reflectivity, results in different clutter power than when using angle independent sea surface reflectivity. The multiple angle and maximum angle from ray tracing clutter power results are identical. The latter is due to the single angle nature of propagation in an evaporation duct.

4.3 Performance analysis for RFC estimation

Refractivity from clutter techniques find the best refractivity profile that matches the observed clutter. The expected clutter power of each candidate profile is computed and an objective function is formed that quantifies the distance between the observed and the modeled clutter. The candidate profile that yields the minimum objective function is declared as the best match. Previous RFC studies have considered the sum of the squared errors, the l_2 norm, as the objective function [13,14,17].

The main purpose of this section is to analyze how different clutter models affect the RFC model parameters.

4.3.1 Surface-based ducts

Surface-based ducts typically are due to the advection of warm and dry coastal air to the sea. These ducts are less common than evaporation ducts but their effect is more prominent on radar returns [1]. Here, the M-profile of a surface-based duct is approximated by a tri-linear function:

$$M(z) = M_0 + \begin{cases} m_1 z & z \leqslant h_1 \\ m_1 h_1 + m_2(z - h_1) & h_1 \leqslant z \leqslant h_1 + h_2 \\ m_1 h_1 + m_2 h_2 & h_1 + h_2 \leqslant z \\ +m_0(z - h_1 - h_2) & \end{cases} \tag{4.13}$$

A genetic algorithm is used to invert for the parameters m_1, m_2, h_1, h_2 based on observed clutter [37]. $m_0 = 0.118$ M-units/m is the slope of the standard atmosphere. The specific choice of M_0 (here 320 M-units) does not affect the propagation pattern of electromagnetic waves and does not affect the parameter estimation.

The radar and environmental parameters in this example are: 3 GHz radar frequency, 25 m antenna height, 5 m/s wind speed, antenna beamwidth of 0.4° and vertical polarization. The surface-duct parameters are identical to those of Fig. 4.2c. The results of Fig. 4.3(a–c) are obtained by running 200 inversions on the modeled clutter.

Two random components in the observed clutter power are modeled here: variations of sea surface reflectivity and noise at the receiver. The selection of sea surface reflectivity statistics for RFC applications depends on the wind speed and direction, grazing angle, polarization and the radar range resolution [144]. Low grazing angle results in complex scattering mechanisms, such as shadowing caused by sea swells and diffraction over the wave edges. These factors increase the spikiness of the sea surface clutter [145]. On the other hand, decreasing the radar resolution increases the number of random scatters inside each range bin, which in turn reduces the spiky behavior of the sea surface reflectivity [1]. The effect of different distributions on clutter modeling and RFC is investigated by [17]. The receiver noise floor is another source of randomness that affects the observed radar clutter [12].

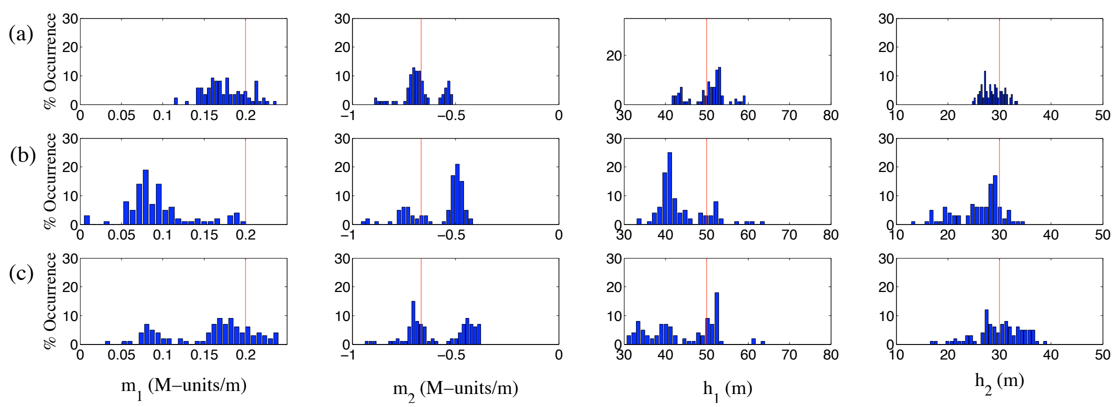

Figure 4.3: Inverted surface based duct parameters using various clutter models: (a) multiple angle, (b) maximum angle from ray tracing, and (c) angle-independent. The simulated clutter power is modeled by the multi angle clutter model and include random components of the sea surface reflectivity and noise floor in the receiver. Vertical lines are the actual parameters of this synthetic example.

Here, variations of the surface reflectivity from GIT is modeled using a lognormal distribution with zero mean and 3 dB standard deviation Gaussian in the logarithmic domain. The additive receiver noise is modeled by a Gaussian distribution over the complex field [17]. Clutter power is normalized at the range of 10 km. Clutter to noise ratio at that range ($\text{CNR}_{10\,km}$) is taken as 40 dB. The observed clutter power is obtained from the multiple grazing angle clutter model.

Results in Fig. 4.3a are distributed around the original parameters as expected, since both simulated clutter and inversion algorithm use the same clutter model. Panels in (b) show that using a single angle clutter model obtained from the maximum angle from ray tracing yields a biased estimation. The bias of the estimated parameters is especially clear in the first slope (m_1) and the second height (h_2) of the trilinear model in this example. Using the maximum angle of arrival is common in the calculation of the worst case clutter [20,25], but is not appropriate for RFC applications. Panels in (c) are obtained by inversion using a grazing angle independent clutter model, which has been used in previous RFC studies. Some bias is observed in RFC using the latter method, but the bias is less than using a clutter model with the maximum arrival angle.

The propagation factor of the profile used in the simulation of Fig. 4.3 is plotted in Fig. 4.4a. The propagation factors and electric fields are obtained using the parabolic equation (PE) code in the Advanced Propagation Model [20]. The differences between the propagation factors of the inverted profiles and the original profile are compared in Panels (b–d) of the same figure. The assumption of an angle independent sea surface reflectivity (Panel d) yields 1.8 dB average error in the propagation factor of the inverted profile in the ducted regions, while inversion using the single angle clutter from maximum arrival angle produces a larger average error of 3.6 dB.

4.3.2 Range-dependent evaporation duct

Evaporation ducts are the most common types of non-standard atmospheric phenomena in maritime environments. The Paulus-Jeske model provides a relationship between modified refractivity M, altitude z and duct height h_d [68]. Assuming equal temperature of the sea surface and air layer boundary simplifies the Paulus-Jeske model [12]:

$$M(z) = M_0 + c_0(z - h_d \ln \frac{z + h_0}{h_0}) \ , \tag{4.14}$$

where M_0 is the base refractivity usually taken as 350 M-units, $c_0 = 0.13$ M-unit/m is the linear slope of the refractivity and h_0 is the roughness factor taken as 1.5×10^{-4} m.

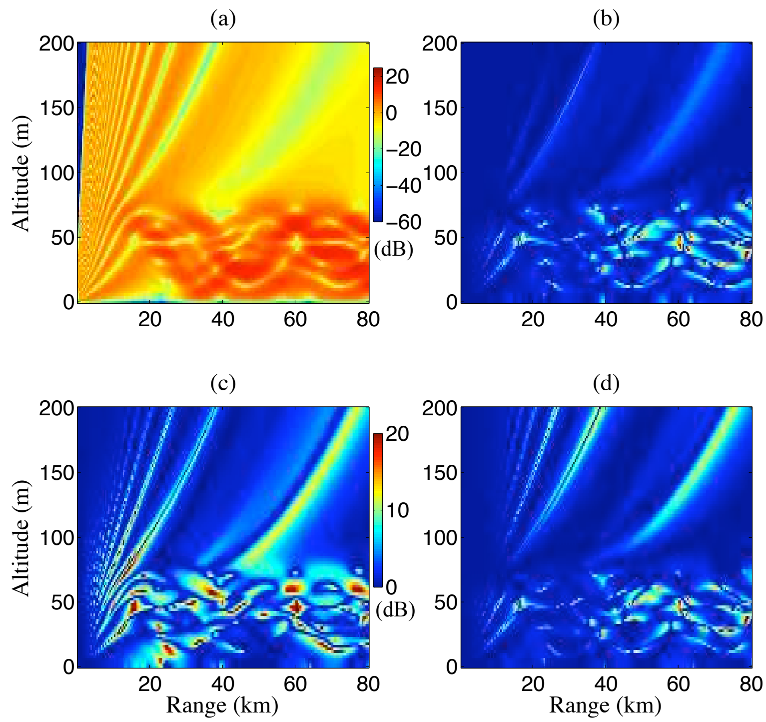

Figure 4.4: (a) Propagation factor (dB) corresponding to the refractivity profile in Fig. 4.2c. (b-d): The difference between the propagation factors of the original profile and inversion of noisy signals using multiple angle, maximum angle from ray tracing, and angle-independent clutter models respectively. The color scale is identical in (b-d). Profile parameters are obtained from the distribution peaks in Fig. 4.3.

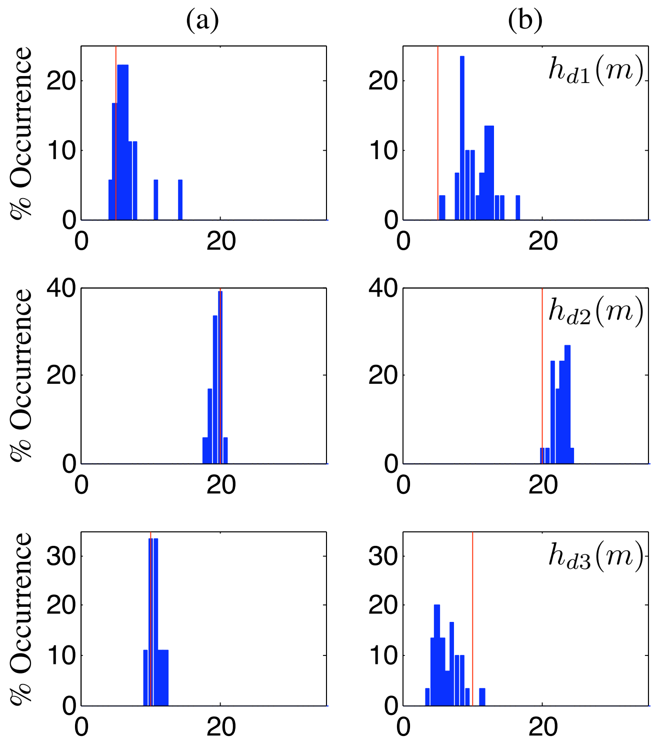

Figure 4.5: Inverted range-dependent evaporation duct height parameters using clutter models: (a) multiple angle and (b) angle-independent. Vertical lines denote the actual parameters of this synthetic example.

This section considers a range-dependent evaporation duct with duct heights of 5, 20 and 10 m at ranges of 0, 12.5 and 25 km respectively (shown in Fig. 4.2e). Duct heights in-between are linearly interpolated. The simulated clutter power is used to invert for the duct heights using the multiple angle and the angle-independent clutter models. The histograms of inverted duct heights are shown in Fig. 4.5 using 30 inversions. The radar in this synthetic example operates at 3 GHz and located at 12 m above the sea surface. The bias in the inversion results of the angle-independent clutter model exemplifies that the latter model is not a good candidate for inverting range-dependent environments.

4.3.3 SPANDAR 1998 dataset

All three clutter models in this study are compared using the SPANDAR 1998 data. Refractivity profile measurements and radar returns were recorded in Wallops Island, Virginia, April 1998 [12,13]. The clutter signals were measured using the Space Range Radar (SPANDAR) with operational frequency of 2.84 GHz, horizontal beamwidth of $0.4°$, elevation angle of 0, antenna height of 30.78 m, and vertical polarization. The refractivity profiles of the environment were measured using an instrumented helicopter provided by the Johns Hopkins University Applied Physics Laboratory. The helicopter flew in and out along the $150°$ radial from a point 4 km due east of the SPANDAR in a saw-tooth pattern with each transect lasting 30 minutes. Only the first 60 km of clutter power is used to invert for the refractivity profile to maintain a high CNR and avoid high spatial variations of the refractivity index with range.

The range-dependent refractivity profile measured by the helicopter is shown in Fig. 4.7a.This profile corresponds to the measurement on April 2, 1998 from 13:19:14 to 13:49:00 (Run 07). The spatial variations of the M-profile are small in the 0–55 km range. Thus, RFC results from the corresponding clutter observations are compared to the average of the measured M-profiles in that range interval. Note that although measurements show slow range variations, the inversions are based on a range-independent profile.

Clutter power recorded from the SPANDAR between azimuth 145–155° are used for estimation of the trilinear function representing a surface based duct, since the clutter pattern and the two duct parameters m_1 and h_1 are rather stationary in this interval [15]. Histograms of estimated parameters using three different clutter models are plotted in Fig. 4.6. The peaks of the parameter distributions (solid lines in Fig. 4.6) are used in Fig. 4.7 to represent the estimated refractivity profiles and their clutter powers. The dashed lines in Fig. 4.6 are the inverted parameters using only the clutter power at 150° azimuth. The distribution of inverted parameters for m_1 and h_1 is narrower than that of m_2 and h_2, since the SPANDAR refractivity profile can be well approximated by a bilinear function.

The average measured refractivity along the first 55 km of recordings and 150° azimuth, the observed clutter along the same angle, and the distribution of clutter power between azimuth 145–155° are compared to the inverted trilinear profiles and their modeled clutter in Fig. 4.7(b,c). Panel (b) shows that the refractivity profile estimated from the multiple angle clutter model has the closest resemblance to the average refractivity

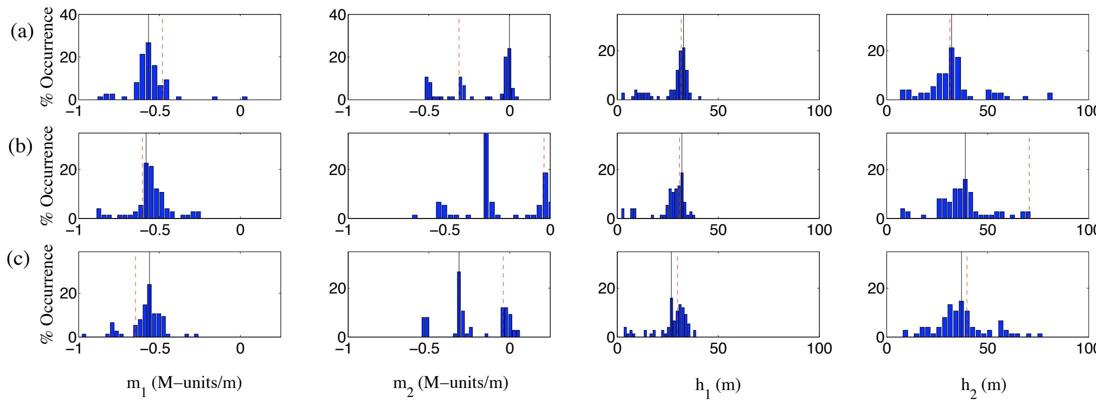

Figure 4.6: Histograms of estimated trilinear function parameters for the SPANDAR dataset, Run 07, along azimuth 145–155°. The peaks of parameter distribution (solid lines) are used in Fig. 4.7. Inversions use different clutter models: (a) multiple angle, (b) maximum angle from ray tracing, (c) angle-independent. Dashed lines show inverted parameters only using the clutter at 150°.

profile measured by the helicopter.

Another important characteristic of refractivity profiles is the M-deficit, which is defined as the total change in the modified refractivity of the trapping layer. The average M-deficit of the observed profile from 0 to 55 km is 22 M-units. This is consistent with the inverted profile with 20 M-units of M-deficit, using the multiple angle clutter model.

Previous RFC studies that used the 1998 SPANDAR dataset were based on an angle-independent clutter model for inversions. Although results of Fig. 4.7 suggests that the multiple clutter model is a better model for inverting clutter data for estimating refractivity profiles, more analysis with real data is required for verification.

4.4 Conclusion

RFC estimates the refractivity profile of maritime environments from observed radar clutter. A grazing angle independent clutter model was assumed in previous studies. Two new clutter models are considered here: a range-dependent multiple angle clutter model and a range-dependent single angle clutter model based on the maximum grazing angle from ray theory. Multiple angle clutter includes all incident grazing angles weighted proportional to their relative powers at each range.

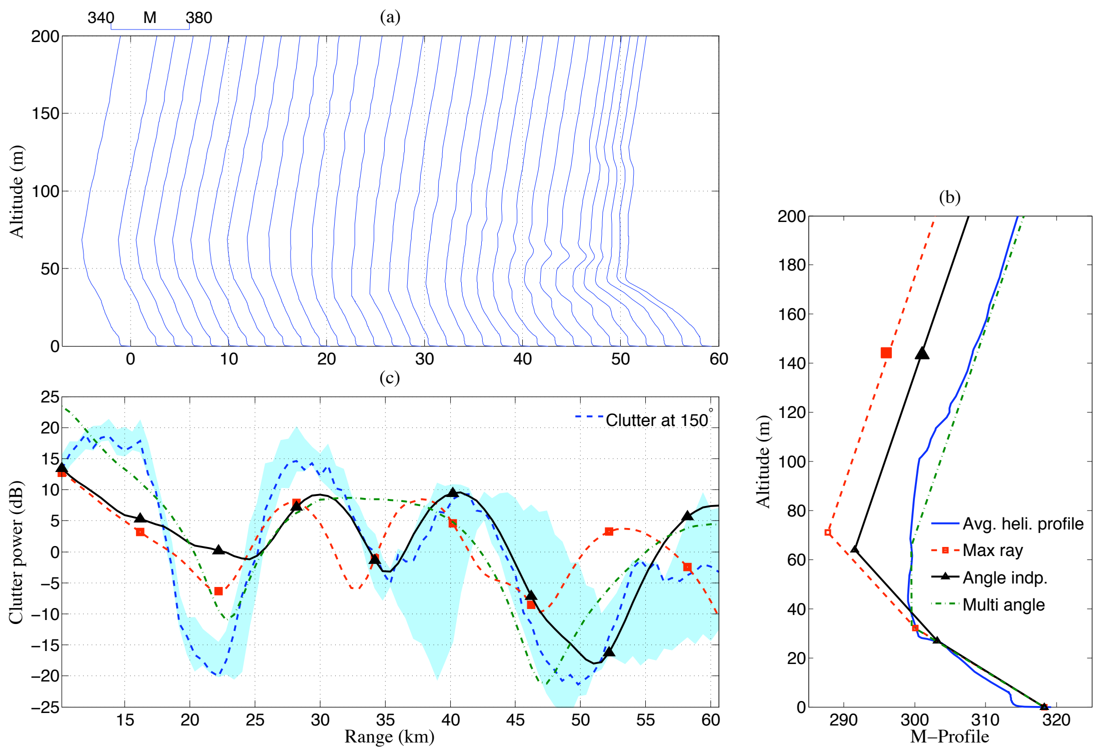

Figure 4.7: (a) Refractivity profile along the 150° azimuthal line. (b) Average of the first 55 km of measured refractivity profiles compared to the estimated profiles from RFC. Trilinear function parameters are obtained from Fig. 4.6. (c) Observed clutter at 150° azimuth and modeled clutters based on inverted profiles. The shaded area shows the variation of clutter power between 145–155° used in RFC.

The performance of clutter models in RFC is compared in a simulated surface-based duct, a range-dependent evaporation duct, and the 1998 SPANDAR dataset. The differences in the clutter power of different models are projected into the environmental parameter domain during the RFC inversion. Results show that the range-dependent single angle clutter model based on the maximum grazing angle yields biased estimations relative to the multiple angle clutter model. An angle-independent clutter model also yields biased parameter inversions, especially when inverting for range-dependent refractivity profiles. Although more analysis is required, the results suggest that the multiple angle clutter model yields more accurate RFC inversions, especially when surface-based ducts and range varying environments are present.

Acknowledgments

The contents of Chapter 4 were previously published as: A. Karimian, C. Yardim, P. Gerstoft, W. .S. Hodgkiss, Amalia Barrios, “Estimation of refractivity using a multiple angle clutter model”, *Radio Sci.*, 47, RS0M07, 2012.

Chapter 5

Towards assimilation of atmospheric surface layer using weather prediction and radar clutter observations

5.1 Introduction

Knowledge of the atmospheric surface layer (ASL) is crucial in weather prediction and in the prediction of radar and communication systems performance at frequencies above 2 GHz on low-altitude paths. Bulk measurements and rocketsondes are *in situ* methods for sampling of the ASL [44]. While having some limitations [45,46] these methods are still in use today. Using radar clutter returns to estimate the refractivity profile in the ASL potentially can be done continuously [12,13,15]. Ship board radars commonly operate across the world's oceans and in many complex coastal environments. These sensors can potentially sample the ASL continuously, in otherwise data denied regions and over water where measurements, particularly vertical profiles, are scarce.

Refractivity profiles and their corresponding radar clutter returns also can be modeled using mesoscale numerical weather prediction (NWP) [34,36]. Sea clutter predictions based on range-varying ASL characterization from the Coupled Ocean and Atmospheric Mesoscale Prediction System (COAMPS) [33] were shown by [34] to be in agreement with clutter observed by a S-band radar in the lee of the Kauai Island. Mesoscale NWP has steadily improved over time and good agreements with observed ASL values have been reported [35,36].

Mesoscale NWP models cannot represent all processes in the atmosphere, and there always is some degree of error in the information that is assimilated into the model. The uncertainty of estimations increase as the distance (in both space and time) increases from the observations that have been assimilated. The spatial resolution of NWP also might be too coarse to capture vertical variations of the atmosphere [146].

Refractivity from clutter (RFC) techniques use observed radar backscatter to estimate the ambient environment refractivity profile [18,147]. There has been strong correlation between the retrieved refractivity profile using an S-band radar and *in situ* measurements by instrumented aircrafts [12,13]. RFC techniques enable the tracking of spatial and temporal changes in the environment [14,15]. There have been attempts to incorporate the worldwide surface meteorological observations database using the environmental library of advanced refractive effects prediction system (AREPS) [16] in the RFC inversion [17]. This method uses regional meteorological duct height statistics as a prior probability density in refractivity profile inversions. One drawback of RFC is the increased variance in the estimated refractivity above the atmospheric duct [37]. Above the duct NWP potentially regularize the RFC-ED solution. On the other hand, RFC inversions can potentially reduce the NWP errors by increasing observations from RFC-capable ships. Here, the application of RFC in evaporation ducting conditions is referred to as RFC-ED.

The dependence of environmental refractivity index on the atmospheric parameters is discussed in Section 5.2, with an emphasis on evaporation ducting conditions. Inversion of the refractivity profile and atmospheric bulk parameters using radar clutter observations are discussed in Section 5.3. Mesoscale NWP and ensemble methods are reviewed in Section 5.4. Integration of NWP and RFC-ED for inversion of the atmospheric bulk parameters is discussed in Section 5.5. The COAMPS model is used to generate ensembles of air and sea temperatures, relative humidity, and wind predictions at 10 m above the sea. These are converted to vertical atmospheric profiles in the vicinity of the sea surface using Navy Atmospheric Vertical Surface Layer Model

(NAVSLaM) [148]. The atmospheric profile obtained from the previous step is used jointly with observed clutter power inversions in evaporation ducts to estimate the air-sea temperature difference (ASTD) and relative humidity in the ASL. It is shown that the parameter estimation uncertainty is reduced compared to using either methods alone.

5.2 Dependence of refractivity index on atmospheric parameters

Humidity typically decreases rapidly in the ASL above the ocean surface, resulting in a leaky waveguide that bends radio waves toward the surface. This feature is known as an evaporation duct. Maritime evaporation ducts are almost always present around the globe [1] and usually affect both low-altitude radar detection and maximum communication ranges. As a consequence, correct characterization of the ASL is important in determining the performance of these systems.

The vertical modified refractivity M is defined as the part per million deviation of the index of refraction n from that of a vacuum after transforming the spherical earth propagation into a flat earth problem. Modified refractivity, M, is a function of atmospheric variables with experimental constants for frequencies 0.1–100 GHz [2,3]:

$$\begin{aligned} M(z) &= \frac{77.6P(z)}{T_{\text{air}}(z)} - \frac{5.6e(z)}{T_{\text{air}}(z)} + 3.75 \times 10^5 \frac{e(z)}{T_{\text{air}}^2(z)} \\ &+ 0.1568z, \end{aligned} \tag{5.1}$$

where $P(z)$ and $e(z)$ are the atmospheric pressure and partial pressure of water vapor in (hPa), and $T_{\text{air}}(z)$ is the absolute air temperature (K), all at altitude z in meters. Monin-Obukhov (MO) similarity theory is widely accepted as the means to relate physical quantities and processes in the ASL [4]. MO-based models can generate vertical atmospheric profiles given the sea surface temperature (T_{sea}), and values at a reference height of air temperature, wind-speed (u), and relative humidity (RH). Corresponding vertical refractivity profiles can subsequently be obtained using (5.1). Except for relatively rare sub-refractive cases, the vertical $M(z)$ profile is concave with respect to height z and has an inflection point referred to as the evaporation duct height (h_d) as illustrated in

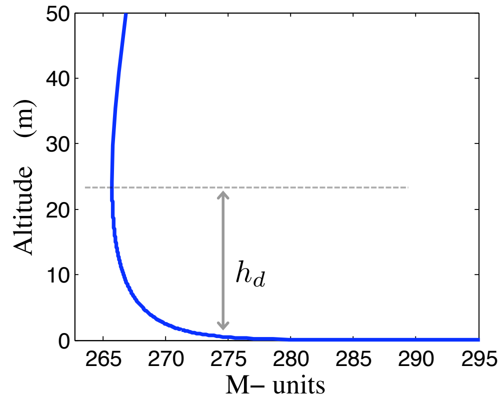

Figure 5.1: The modified refractivity profile of an arbitrary evaporation duct with $\Delta T = 0$ and duct height $h_d = 24$ m.

Fig. 5.1. As a point of clarification, the vertical M-profile is not uniquely defined by h_d in most MO models including [67,72].

NAVSLaM [72,148] is based on MO theory and is used here to compute the vertical atmospheric and refractivity profiles in an evaporation duct from bulk parameters (air temperature, humidity and pressure at a certain height from the sea surface). Bulk parameters can be provided by in-situ measurements, climatological databases, or NWP.

Changes of duct height versus ASTD ($\Delta T = T_{\text{air}} - T_{\text{sea}}$), relative humidity, and wind-speed are shown in Fig. 5.2 for sea temperatures $T_{\text{sea}} = 15$°C and 30°C. Atmospheric variables T_{air}, RH, u are all taken at 10 m. In general, ASL models are insensitive to the atmospheric pressure [149], and a typical atmospheric pressure of 1020 hPa is used here. Fig. 5.2 shows rapid changes of the duct height with ΔT where $\Delta T > 0$, and less variations where $\Delta T < 0$. Comparison of Panels (a,c) and (b,d) shows that the sensitivity of duct height to ΔT and RH in warm sea waters is more than in colder waters. Clearly, the sensitivity of h_d to changes in ΔT, RH, and u is state-dependent and small errors in ΔT, RH, and u can result in large errors in h_d when $\Delta T > 0$.

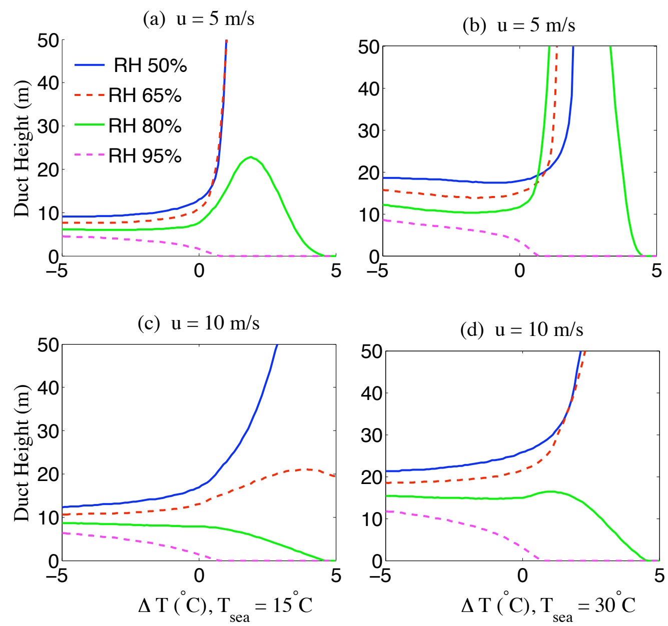

Figure 5.2: Evaporation duct height versus $\Delta T = T_{\text{air}} - T_{\text{sea}}$ and relative humidity (RH) for wind-speed (u) of 5 m/s and 10 m/s, obtained by NAVSLaM. All atmospheric variables are referenced at 10 m above the sea surface. $T_{\text{sea}} = 15°\text{C}$ in (a,c) and $T_{\text{sea}} = 30°\text{C}$ in (b,d).

5.3 Refractivity from clutter

Radar clutter in a maritime environment depends on the two way propagation loss from the transmitter to the range cell, and propagation loss depends on the refractivity profile. Assume an environment described by a vector of model parameters $\mathbf{m}$ through which the electromagnetic waves are propagated. Previous RFC-ED studies have considered the duct height of an evaporation duct as the state parameter [12,17,56] under the assumption that $\Delta T = 0$. This assumption was important to constrain the possible atmospheric solutions. The vector of atmospheric parameters $\mathbf{m} = [\Delta T, RH]^{\mathrm{T}}$ at a height of 10 m are used here as the state vector.

5.3.1 Sea clutter model

The expected radar clutter power in a maritime environment can be expressed as a function of the radar parameters, the propagation factor F which is a function of the refractivity profile $\mathbf{m}$ and range r, and grazing angle θ [1]:

$$P_{\mathrm{c}}(\mathbf{m}, r) = \frac{P_{\mathrm{t}} G^2 \lambda^2 \theta_{\mathrm{B}} c \tau \sigma_0 \sec(\theta) F^4(\mathbf{m}, r)}{2(4\pi r)^3 L}, \tag{5.2}$$

where P_{t} is the transmitter power, G the antenna gain, λ the wavelength, θ_{B} the antenna pattern azimuthal beamwidth, c the propagation speed, τ the pulse width, σ_0 the expected sea surface reflectivity per unit area, and L the total assumed system losses. Grazing angle θ is also a function of $\mathbf{m}$ and r. The sea surface reflectivity in ducting conditions typically is computed based on the work by [87].

For simplicity, synthetic clutter powers are computed assuming range-independent refractivity profiles and wind speed, using the parabolic equation based Advanced Propagation Model (APM) [150]. This method can easily be extended to range-dependent profiles. For range-independent evaporation ducts the sea surface grazing angles are constant hence, sea-surface reflectivity σ_0 can be assumed to be range-independent [12]. Normalization of (5.2) with respect to the clutter power at a fixed range r_0 (here $r_0 = 5$ km) simplifies inversions by getting rid of the constant parameters [13]:

$$P_{\mathrm{n,c}}(\mathbf{m}, r) = \frac{P_{\mathrm{c}}(\mathbf{m}, r)}{P_{\mathrm{c}}(\mathbf{m}, r_0)} = \frac{F^4(\mathbf{m}, r) r_0^3}{F^4(\mathbf{m}, r_0) r^3} \,. \tag{5.3}$$

Letting F, $P_{\mathrm{n,c}}$ represent the associated values in dB as opposed to real numbers, we can rewrite 5.3 as:

$$P_{\mathrm{n,c}}(\mathbf{m}, r) = 4\left(F(\mathbf{m}, r) - F(\mathbf{m}, r_0)\right) + 3 \log \frac{r}{r_0} \,. \tag{5.4}$$

5.3.2 Refractivity profile inversion and bulk-parameters for evaporation ducts

Inversion for the evaporation duct height from a S-band radar clutter was reported in [12]. The sensitivity of the radar clutter power to the duct height at different frequencies was studied by [17]. RFC-ED studies in the past have assumed sea and air temperatures to be equal. This assumption simplifies the refractivity profile of an evaporation duct to be logarithmic in the vicinity of sea surface and only dependent on the duct height.

An objective function J_{RFC} that quantifies the difference between the normalized observed and modeled clutter power, $\mathbf{P}_{\mathrm{n,o}}$ and $\mathbf{P}_{\mathrm{n,c}}(\mathbf{m})$, is formed here. $\mathbf{P}_{\mathrm{n,o}}$ and $\mathbf{P}_{\mathrm{n,c}}$ are the vectors of clutter power in dB over N range bins. The optimal solution minimizes the objective function:

$$\hat{\mathbf{m}} = \underset{\mathbf{m}}{\operatorname{argmin}} \; J_{\text{RFC}}(\mathbf{P}_{\mathrm{n,o}}, \mathbf{P}_{\mathrm{n,c}}(\mathbf{m})) \,. \tag{5.5}$$

The backscattered radar signal can be modeled using a multiplicative random variable representing the variable sea-surface reflectivity and additive thermal noise. Following [1], variation of the sea-surface reflectivity is assumed to have a log-normal density. Working in the high CNR (clutter to noise ratio) regime, the additive noise term can be neglected. Therefore, the observed clutter power in the logarithmic domain is obtained as:

$$\mathbf{P}_{\mathrm{n,o}} = \mathbf{P}_{\mathrm{n,c}}(\mathbf{m}) + \mathbf{n} \,, \tag{5.6}$$

$$\mathbf{n} \sim \mathcal{G}(\mathbf{0}, \mathbf{C}_{\mathrm{o}}) \,, \tag{5.7}$$

where $\mathbf{P}_{\mathrm{n,o}}$ and $\mathbf{P}_{\mathrm{n,c}}(\mathbf{m})$ are in dB, $\mathbf{n}$ is the vector of logarithmic random sea reflectivity variations that is assumed to be Gaussian, and $\mathbf{C}_{\mathrm{o}}$ is the covariance matrix of sea surface reflectivity variations. The log-likelihood objective function J_{RFC} is expressed by:

$$J_{\text{RFC}} = (\mathbf{P}_{\mathrm{n,o}} - \mathbf{P}_{\mathrm{n,c}}(\mathbf{m}))^T \mathbf{C}_{\mathrm{o}}^{-1} (\mathbf{P}_{\mathrm{n,o}} - \mathbf{P}_{\mathrm{n,c}}(\mathbf{m})) \,. \tag{5.8}$$

Range bin widths of RFC are assumed to be in the order of hundreds of meters. Due to this large distance, sea-surface variations of consecutive bins are assumed to be uncorrelated. Thus, $\mathbf{C}_{\mathrm{o}} = \nu \mathbf{I}$ where ν is the variance of the logarithmic sea-surface reflectivity, and $\mathbf{I}$ is the identity matrix. Equation (5.8) is the negative log-likelihood function under log-normal radar cross section (RCS) statistics. Modeling random variations of the clutter power due to the changes in the sea-surface reflectivity by the log-normal density often is a good approximation in RFC applications [27].

A weakness of RFC-ED as a stand-alone means for characterizing the ASL's refractivity is using a log-linear refractivity profile defined by a single-parameter [12]. This simplification causes small errors when the inverted refractivity profile obtained from RFC-ED is used for propagation calculations at the same frequency as the sensing radar. Errors increase, though, as the difference between the frequencies of the sensing and the use of the profiles increases. Fig. 5.3 shows that not only the duct height, but also the shape of the profile affects the radar clutter. This effect is more pronounced at higher frequencies. In this example, the sea surface temperature is 30°C, wind-speed is 5 m/s, and radar is 10 m above the sea surface. The clutter power fall-off rate for a 14 m duct in $\Delta T < 0$ and $\Delta T = 0$ conditions are similar at 3 GHz. However, those fall-off rates differ at 10 GHz. Thus, knowledge of the bulk parameters is required when inverted parameters at one frequency are to be used at a different frequency. Using the refractivity profile obtained from NWP might improve the modeling error at other frequencies. Figs. 5.3 and 5.4 both use NAVSLaM to obtain the refractivity profile from COAMPS parameters. APM [150] then is used to compute the clutter power from these refractivity profiles.

The radar clutter power is sensitive to changes in the atmospheric variables. [151] showed that radar propagation is also more sensitive to changes of humidity and temperature than to those of pressure levels. Fig. 5.4 demonstrates the sensitivity of the clutter power to atmospheric parameters. This figure shows the changes in the clutter power of a radar at 10 m above the sea surface, operating at 3 GHz, when ASTD changes by 1°C, or relative humidity changes by 10%. Here it is assumed that pressure is constant, surface temperature and wind-speed are obtained from COAMPS ensemble forecasts, and radar clutter is used to invert for humidity and ASTD.

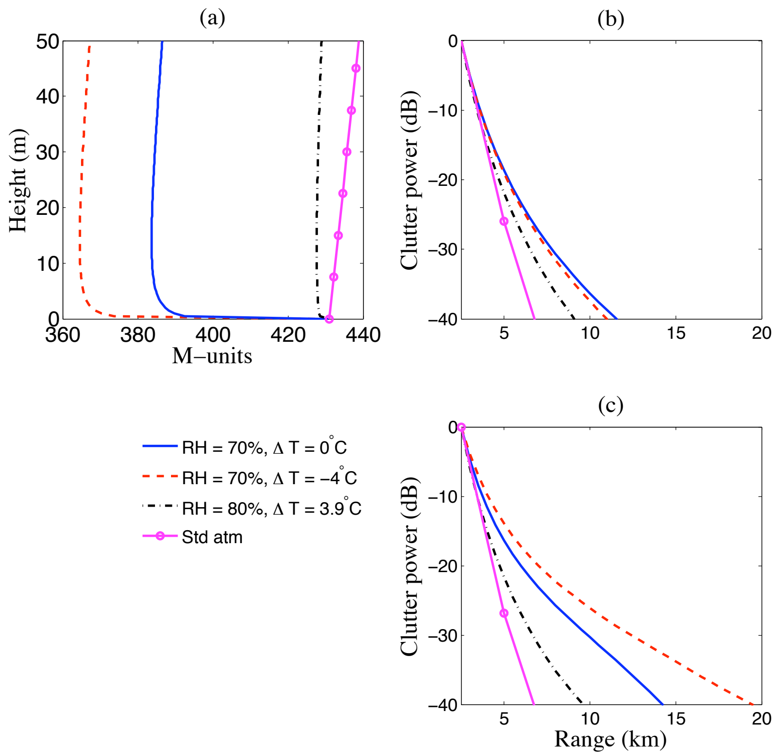

Figure 5.3: (a) Modified refractivity profiles, all with duct height of 14 m. The corresponding clutter powers when the radar is located at 10 m, for operational frequencies of (b) 3 GHz, and (c) 10 GHz. $T_{\text{sea}} = 30°C$, and $u = 5$ m/s.

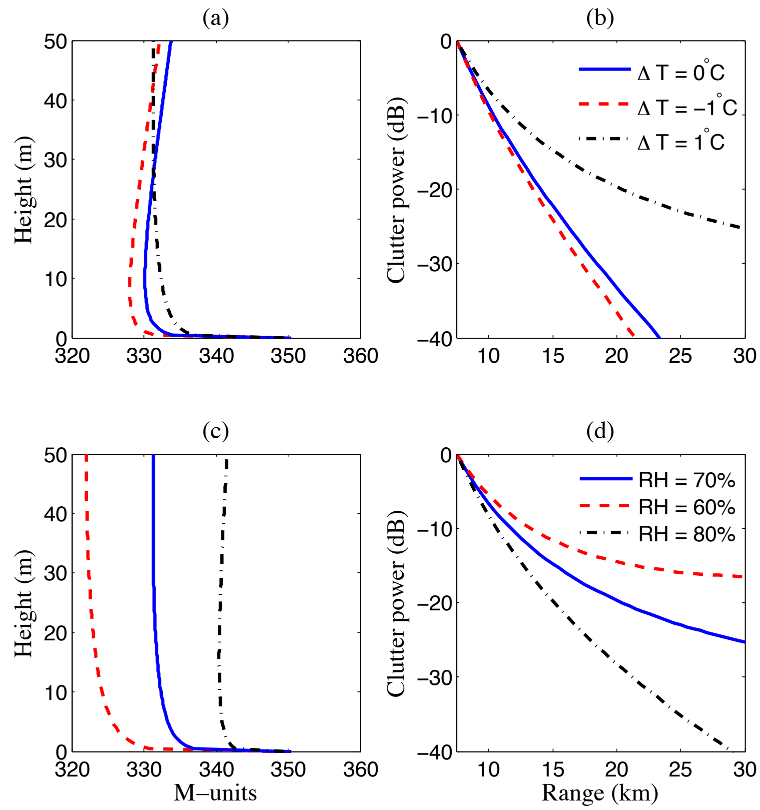

Figure 5.4: (a,c): Modified refractivity profiles, (b,d): Corresponding clutter powers. Radar frequency is 3 GHz and located at 10 m above the sea-surface. $T_{\text{sea}} = 15°C$, and $u = 5$ m/s. (a,b): $RH = 70\%$, different ΔT conditions. (c,b): $\Delta T = 1°C$, different humidities.

5.4 Numerical weather prediction

NWP depends heavily on the initial and lateral boundary conditions, land-sea surface and terrain conditions, numerical approximations and parameterization of physical processes [146]. The uncertainty in the aforementioned factors gives rise to an uncertainty in NWP analysis and forecasts. Ensemble methods use the perturbations of the initial state and perturbations of model physics to yield the density of predicted parameters.

Ensemble methods, in their simplest form, involve averaging over all members with equal weight. [152] suggested that using the ensemble average improves the NWP accuracy only up to the point that there is a change in the meteorological regime, i. e. when there is a bifurcation in the member predictions. The reason is that the ensemble average does not correspond to a meaningful forecast after the divergence point of various forecasts. [153] used a Bayesian approach to find ensemble weights for forecasting. They further showed that spatial smoothing helps the reliability of results. [154] used the variational data assimilation framework and assumed Gaussian densities for variations of weather states to assimilate weather forecast ensemble members.

COAMPS produces predictions of the ocean and atmosphere on time-scales of hours to several days [33]. Data from radiosondes, aircraft, buoy and ship data are used to blend the observed data with the first-guess field generated by COAMPS [155]. Multivariate optimum interpolation (MVOI) analysis of wind and pressure and univariate interpolation of temperature and moisture are used to combine the observational corrections to the first-guess from COAMPS previous 12-hour forecast.

COAMPS is a nonhydrostatic mesoscale model developed from the Navier-Stokes equations for winds, potential temperature, perturbation pressure, and five species of water and their auto-conversions including mixing ratios of water vapor, clouds, rain, snow, ice and grauple. It contains physical parameterizations appropriate for high-resolution characterization of the surface energy budget, surface fluxes, planetary and marine boundary layers, short and longwave radiation, and convection. For the ensemble forecasts evaluated here, three nested grids were used with horizontal spacings of 45, 15, and 5 km, respectively. Each domain has 45 vertical levels with the lowest located at 10 m. The vertex of the third grid (origin in Figs. 5.5–5.6) is at $[18.10048°\text{N},$

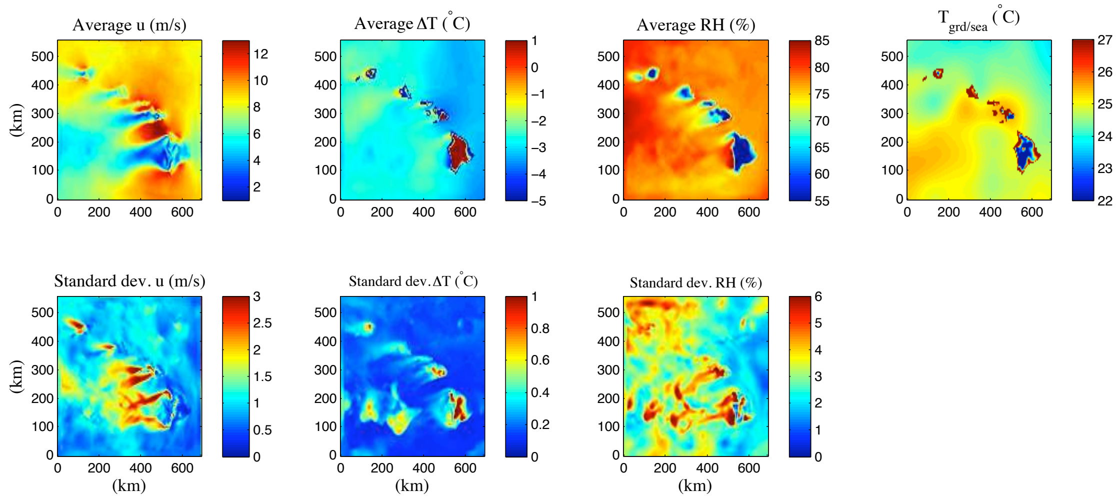

Figure 5.5: Average values (top row) and standard deviation (bottom row) of COAMPS ensemble of wind-speed, air-sea/ground temperature difference and relative humidity at 10 m around the Hawaii Islands for May 7, 2008 at 12 am UTC using 5 km grid spacings. The last column is the observed surface temperature (sea or ground surface) during the same time using buoy and ship data.

199.0548°E], south west of the Hawaiian Islands. Sea temperatures are obtained from satellite data, and no perturbation is introduced to this parameter in generation of ensemble members. Here, the ensemble transform [156] is used to generate initial states for ensemble predictions [157]. One of the ensemble members is the control run and the rest are run with perturbed conditions. The error covariance of the ensemble with respect to the average prediction is formed at the start of each forecast cycle (i.e. every 6 hours).

Two NWP ensembles in the region of the Hawaiian Islands are used here that are known to have evaporation ducting conditions. The first is a 16-member ensemble on the air-sea boundary layer at 12 am on May 7, 2008, and the second is a 32-member ensemble that correspond to July 26–28, 2008 with 3 hour gaps starting from 12 am UTC. The data that correspond to 12 am UTC May 7, 2008 are shown in Fig 5.5. Atmospheric parameters shown in that figure are all at 10 m. Sea temperature in general is higher than the air temperature in this dataset. COAMPS outputs at 10 m are used as inputs to NAVSLaM to find the evaporation duct profiles at each location. The average and standard deviation of duct heights are shown in Fig. 5.6. Duct height is not very sensitive

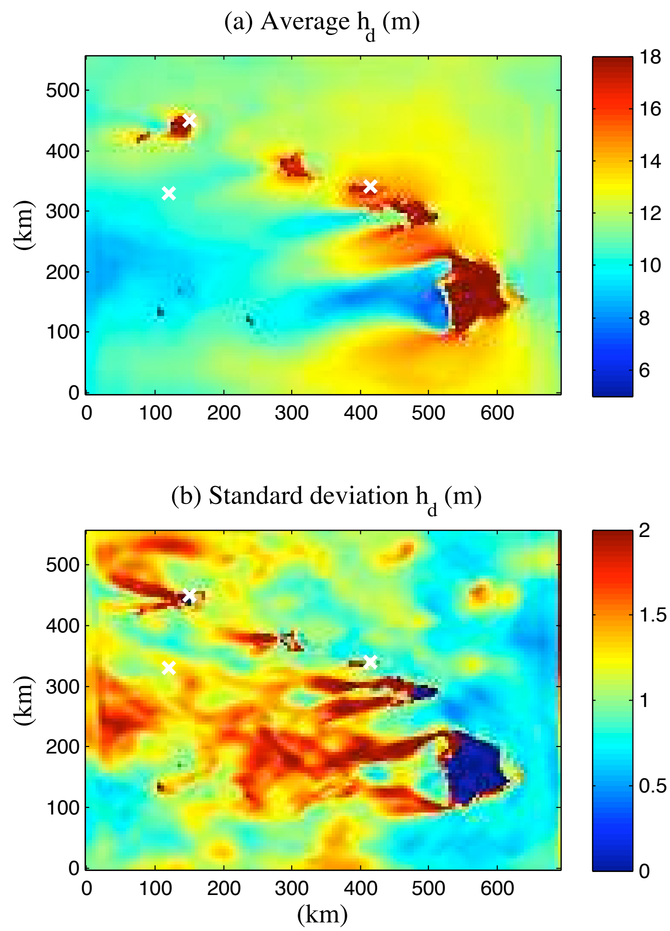

Figure 5.6: (a) Average and (b) standard deviation of duct heights obtained by running NAVSLaM on the COAMPS ensemble in Fig. 5.5. The geographic locations of cases analyzed in Figs. 5.7–5.9 are marked with white (x).

to ΔT changes where air temperature is less than the sea temperature. The ensemble for July 26–28, 2008 shows similar variations in the standard deviation of atmospheric variables and duct heights, and thus are not shown.

Ensemble methods provide the environmental parameter uncertainty in NWP predictions. This will allow the integration of the NWP results with the RFC. The data assimilation method given in the next section will merge these two sources of information (NWP and RFC) on the ASL parameters taking into account how much belief we have in each method via the uncertainties attached to each method.

5.5 Integration of radar observations and weather prediction

Data assimilation generally can be described as an optimization problem to integrate observations with predictions [158]. [130] used clutter powers from multiple grazing angles to infer the refractivity profile of surface ducts and introduced limits on possible refractivity profile solutions from climatological constraints. In a similar framework, ocean salinity and temperature measurements in the water column were used to update the water-mass properties in oceanic circulation models [159]. Underwater acoustic propagation loss has been used by [160] for coupled oceanographic and acoustic data assimilation.

A quadratic metric is defined to measure the fitness of each set of candidate atmospheric variables $\mathbf{m}$ to predicted values by NWP and inversions of observed clutter power $\mathbf{P}_{\mathrm{o}}$. Here, $\mathbf{m} = [\Delta T, RH]^{\mathrm{T}}$, with atmospheric variables at a height of $10\,\mathrm{m}$. The clutter power fall-off rate does not convey information about the air pressure and absolute value of the wind-speed, and it is a weak function of sea-surface temperature. Hence, these are used directly from NWP.

Variational data assimilation studies typically have considered a quadratic cost function that assumes the prediction and observation error terms to have Gaussian densities [146,158]. The joint cost function of NWP and RFC-ED is obtained by statistics yielded from the NWP ensemble and the RFC-ED inversion equation (5.8):

$$\begin{aligned} J(\mathbf{m}) &= J_{\text{NWP}}(\mathbf{m}) + J_{\text{RFC}}(\mathbf{m}) \\ &= \frac{1}{2}(\mathbf{m} - \boldsymbol{\mu}_{\text{NWP}})^T \mathbf{C}_{\mathrm{N}}^{-1} (\mathbf{m} - \boldsymbol{\mu}_{\text{NWP}}) \\ &+ \frac{\lambda}{2}(\mathbf{P}_{\mathrm{n,o}} - \mathbf{P}_{\mathrm{n,c}}(\mathbf{m}))^T \mathbf{C}_{\mathrm{o}}^{-1} (\mathbf{P}_{\mathrm{n,o}} - \mathbf{P}_{\mathrm{n,c}}(\mathbf{m})) \end{aligned} \tag{5.9}$$

where $\boldsymbol{\mu}_{\text{NWP}}$ and $\mathbf{C}_{\mathrm{N}}$ are the average and covariance of NWP ensemble atmospheric variables. λ is a constant to balance the effect of RFC-ED and NWP on the joint penalty function. Here, $\lambda = 1$ is used, which corresponds to a Bayesian solution using the NWP term as a prior and RFC-ED as the likelihood term with Gaussian variations. A two-dimensional search through the ΔT and RH parameter space is used here to find the optimum $\mathbf{m}$.

Analysis of NWP outputs indicates that assuming a range-independent profile for a radius of 20–25 km is reasonable far from the coasts. Simulations in this paper are made by taking the average COAMPS predictions at the location of interest and assuming that the ΔT, humidity and wind profiles are range-independent up to a range of 25 km. The same approach can be extended to range-dependent profile inversions where the state vector will be larger.

Three atmospheric conditions classified by values of ΔT are investigated. The cases of $\Delta T > 0$, $\Delta T = 0$, and $\Delta T < 0$ loosely correspond to the stable, neutral, and unstable thermodynamic atmospheric conditions, respectively. The geographic locations of these examples are shown with white crosses in Fig. 5.6. The most prevalent situation in the dataset is the $\Delta T < 0$ condition. This condition is investigated with the example in Fig. 5.7. The $\Delta T = 0$ condition occurs rarely. One example of this condition is studied in Fig. 5.8. The $\Delta T > 0$ condition in our dataset occurs only near the coast where the assumption of a range-independent profile fails. We only use the range-independent refractivity profile assumption in Fig. 5.9 to demonstrate an inversion example under the $\Delta T > 0$ condition. The priors for ΔT and RH for RFC-ED inversions are assumed to be uniformly distributed with ΔT = [-4°C, 2°C] and RH = [50%, 100%] for all examples.

All three examples in Figs. 5.7–5.9 consider the radar clutter with CNR of 25 dB at the range of 10 km. A 5° azimuthal segment is used for each inversion where synthetic clutter power is generated with independent noises and 1° azimuthal spacing. The logarithmic radar cross section is assumed to have a Gaussian density with zero mean and 3 dB standard deviation. The average of the NWP ensemble is taken as the true state and used to generate 100 clutter power realizations. The synthetic clutter power in the range of 5–25 km with bins every 1 km is used for RFC-ED inversions (5.8) and joint NWP, RFC-ED inversions (5.10). Two-dimensional and marginal densities of NWP ensemble, RFC-ED inversions and joint inversions are all demonstrated in these plots. Histograms of inverted duct heights obtained from RFC-ED inversions are also plotted.

An example with $\Delta T < 0$ corresponding to 12 am UTC May 7, 2008 at [120, 330] km in Fig. 5.5 is shown in Fig. 5.7. RFC-ED is insensitive to ΔT and more sensitive to the humidity. This is consistent with Fig. 5.2 where the duct height is rather insensitive

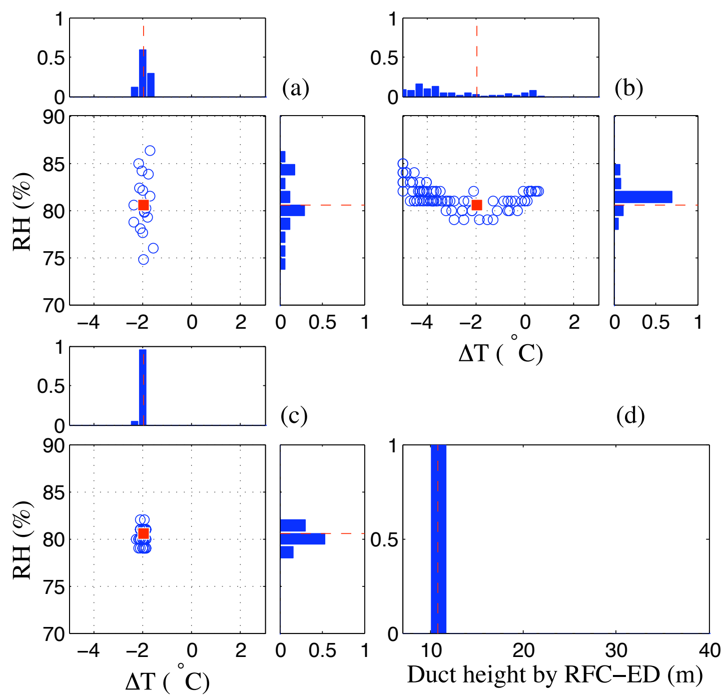

Figure 5.7: Case 1, $\Delta T < 0$ corresponding to 12 am UTC May 7, 2008 at [120, 330] km in Fig. 5.5, (a–c): Scatter plots of ΔT and RH, and their marginal densities obtained by (a) COAMPS ensemble, (b) RFC-ED, (c) joint NWP, RFC-ED. The NWP ensemble mean (□) is used for clutter power simulations. (d): Histogram of duct heights obtained by RFC-ED in (b).

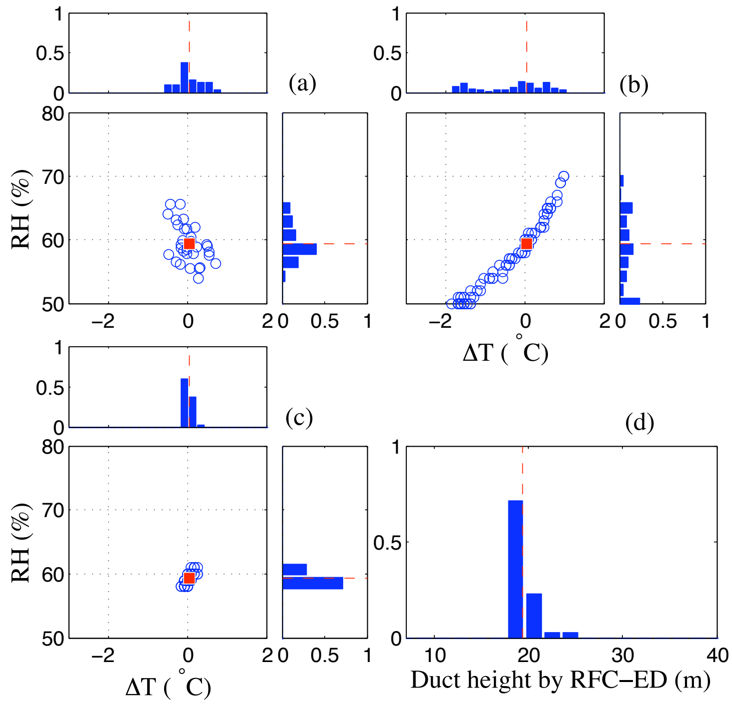

Figure 5.8: Case 2, $\Delta T = 0$ corresponding to 3 am UTC July 27, 2008 at [415, 340] km in Fig. 5.5, (a–c): Scatter plots of ΔT and RH, and their marginal densities obtained by (a) COAMPS ensembles, (b) RFC-ED, (c) joint NWP, RFC-ED. The NWP ensemble mean (□) is used for clutter power simulations. (d): Histogram of duct heights obtained by RFC-ED in (b).

to ΔT where $\Delta T < 0$, but highly sensitive to changes in the level of relative humidity. In contrast, the NWP has a larger uncertainty for RH and smaller for ΔT. Hence, the combination of RFC-ED and NWP reduces the uncertainties in atmospheric parameter estimation drastically. Pairs of $[\Delta T, RH]^{\mathrm{T}}$ found by RFC-ED form a curve of points with very similar duct heights. This is shown by the narrow histogram of inverted duct heights in (d) using RFC-ED. The clutter power depends strongly on the duct height, with other parameters having second order effects [12].

An example with almost $\Delta T = 0$ is considered in Fig. 5.8. RFC-ED provides a set of solutions that all correspond to similar clutter power patterns. These solutions all yield similar duct heights demonstrated by the narrow probability density in Panel (d). Similarity of duct heights of inverted profiles is expected since clutter power is a strong function of the duct height in evaporation ducts, rather than the minor changes

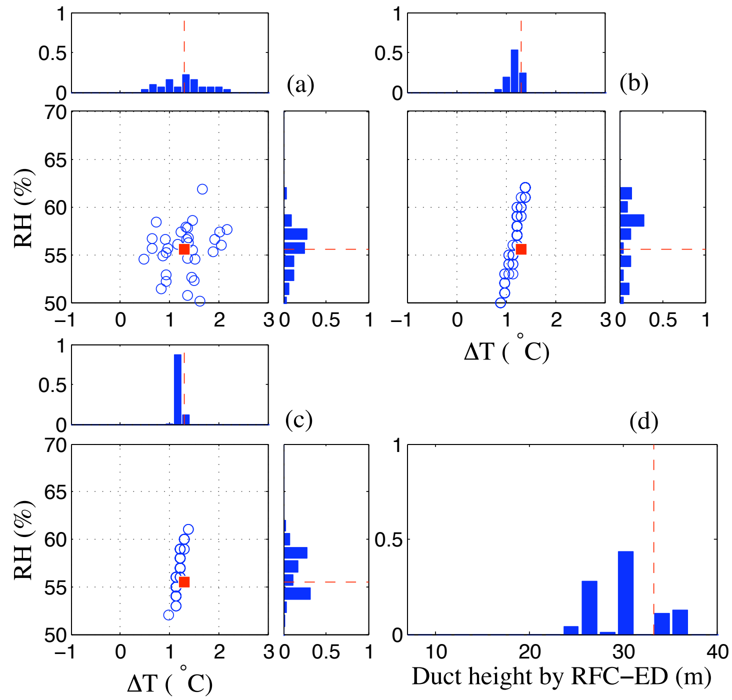

Figure 5.9: Case 3, $\Delta T > 0$ corresponding to 12 am UTC July 28, 2008 at [150, 450] km in Fig. 5.5, (a–c): Scatter plots of ΔT and RH, and their marginal densities obtained by (a) COAMPS ensembles, (b) RFC-ED, (c) joint NWP, RFC-ED. The NWP ensemble mean (□) is used for clutter power simulations. (d): Histogram of duct heights obtained by RFC-ED in (b).

in the refractivity index gradient. The joint inversion of NWP and RFC-ED reduces the uncertainty of lower atmospheric parameter estimation found from either method.

An example with $\Delta T > 0$ is demonstrated in Fig. 5.9. The duct-height uncertainty obtained from RFC-ED is reduced in this case, as seen in Panel (d). The reason is that the M-profile converges to a vertical profile when $\Delta T > 0$. For example, compare the shape of M-profiles in Fig. 5.3, where all M-profiles have the same duct height.

The environment can evolve after earlier COAMPS predictions. An example of this scenario is provided in Fig. 5.10. This example considers the original atmospheric parameters to be $\Delta T = 0$, and $RH = 60\%$ obtained by COAMPS. The environment is assumed to have evolved to a new state where $\Delta T =$1.5°C and $RH = 65\%$. Combination of RFC-ED and NWP helps to obtain inversion results closer to the current environmental state.

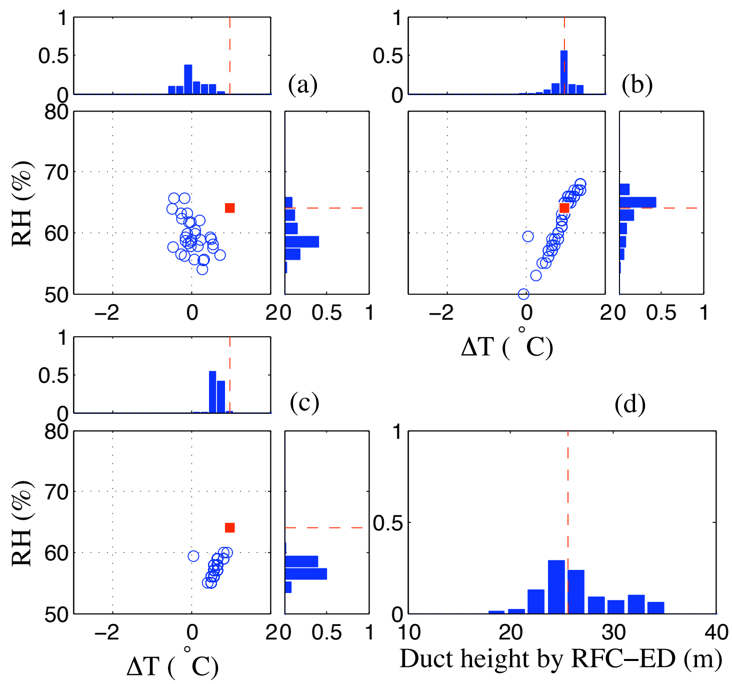

Figure 5.10: Case 4, evolution of the environment after predictions, (a–c): Scatter plots of ΔT and RH, and their marginal densities obtained by (a) COAMPS from Fig. 5.8, (b) RFC-ED, (c) joint NWP, RFC-ED. The square shows the assumed true state used for clutter power simulations, (d): Histogram of duct heights obtained by RFC-ED in (b).

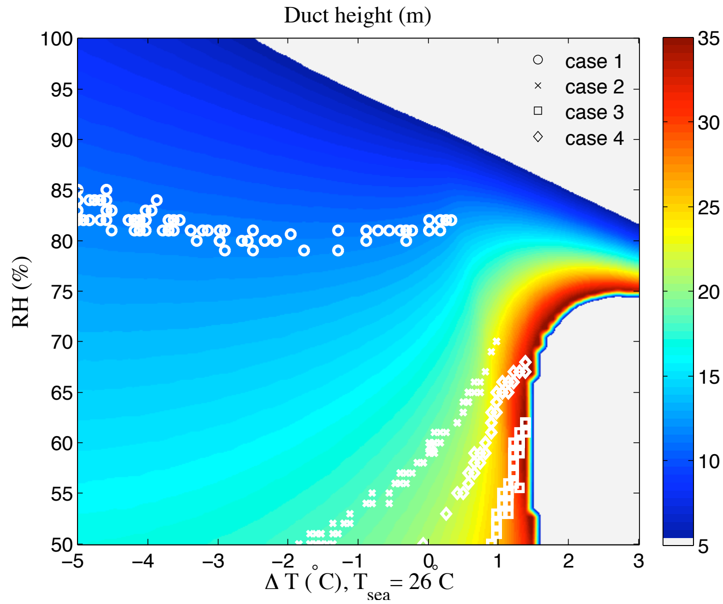

Figure 5.11: Duct height (m) as a function of ΔT and RH with $T_{\text{sea}} = 26°C$ and $u = 8$ m/s, conditions similar to average ensemble in Fig. 5.5. Scattered symbols show inversion results obtained by RFC-ED. Cases 1–4 refer to Figs. 5.7–5.10, respectively.

A 2-dimensional plot of duct height as a function of ΔT and RH is shown in Fig. 5.11, with conditions similar to Figs. 5.7–5.10. Inverted parameters obtained from RFC-ED in those examples are also shown. Inversion results follow the contours in Fig. 5.11, due to the strong dependence of the clutter power on duct height. This is consistent with the histograms of duct heights in Panel (d) of Figs. 5.7–5.10, especially the narrow histograms in $\Delta T < 0$ and $\Delta T = 0$ conditions. When varying ΔT and RH, NAVSLaM produces a non-logarithmic profile. Nevertheless, the profiles are characterized in terms of just the duct height. NAVSLaM does not provide reliable refractivity profiles for large positive ΔT (white area in Fig. 5.11). For these reasons, inverted duct heights are not constant with variations of ΔT and RH in inversions studied in Figs. 5.7–5.10, and the spread of inverted duct height histograms gets larger for $\Delta T > 0$.

The propagation factor F is defined as the ratio of the magnitude of the electric field at a given point under specified conditions to the magnitude of the electric field under free-space conditions with the same transmitter [1]. The probability densities of propagation factor using atmospheric parameters from the three methods discussed are shown in Fig. 5.12 for heights of 10 and 40 m and range of 25 km. This example uses 1000 synthetic clutter powers in each case to generate histograms. The propagation factor probability density obtained from NWP appears to have a flat distribution, and more peaked for RFC-ED. RFC-ED yields atmospheric parameters that result in similar clutter power, and thus also result in similar propagation factors. The probability density of F using the joint technique appears to be a combination of propagation factor densities obtained from NWP and RFC-ED. However, this combination is not linear since the relationship between F and atmospheric variables ΔT and RH is not linear. The importance of estimating the true atmospheric conditions for radar performance prediction can be seen by comparing the estimated F values to the F of standard atmosphere with no ducting. Standard atmosphere propagation factors at 25 km range and heights of 10 m and 40 m are -27 dB and -35 dB, respectively. Thus, failing to model the evaporation duct can lead to errors of 10–40 dB in the expected radar signal power in assessment of radar propagation.

5.6 Conclusion

Here, the Numerical Weather Prediction (NWP) and Refractivity from Clutter (RFC) results were combined, opening the way for a full data assimilation of the refractivity profile. NWP and RFC can be used jointly in maritime environments to reduce the estimation variance of atmospheric variables near the sea surface. Advantages of NWP (providing prior information to a high altitude) and RFC (real-time tracking of atmospheric parameters) can be utilized jointly to provide a powerful inversion method. This investigation focused on RFC for evaporation ducts (RFC-ED) within the atmospheric surface layer.

Spatial and temporal variability in the atmosphere were captured by COAMPS non-hydrostatic mesoscale forecasts at 5-km horizontal grid spacing. Atmospheric ensemble hindcasts were used here from Summer 2008 around the Hawaiian Islands where it was known to have prevailing evaporation ducting conditions. These deterministic forecasts provided the control run to a 16-member and 32-member ensemble suite. An ensemble transform technique was used in which initial conditions at each forecast cycle

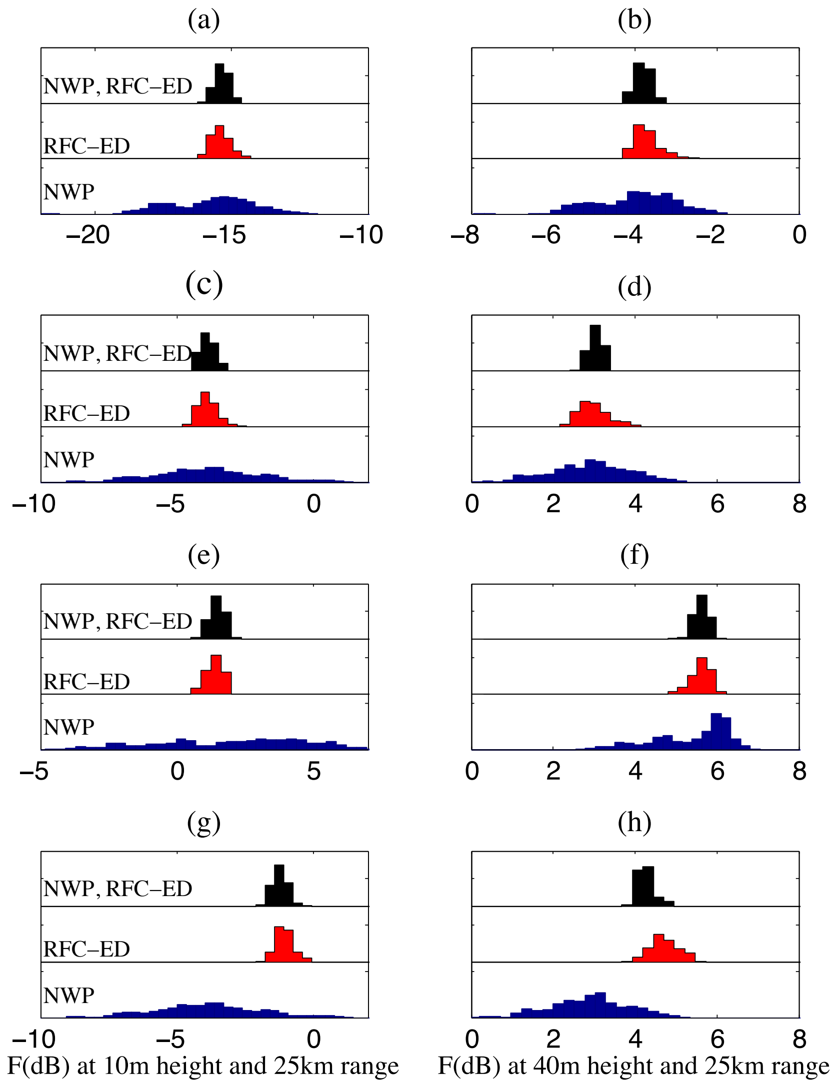

Figure 5.12: The distribution of propagation factor F using NWP, RFC-ED and joint NWP RFC-ED at heights of 10 m and 40 m and range of 25 km from an assumed source. The vertical axis is the empirical probability. (a,b): The example in Fig. 5.7 with $\Delta T < 0$, (c,d): the example in Fig. 5.8 with $\Delta T = 0$, (e,f): the example in Fig. 5.9 with $\Delta T > 0$, (g,h): the biased example in Fig. 5.10.

were perturbed to depict how uncertainty due to errors in the initial state would evolve within the forecasts.

The RFC-ED was implemented by creating an objective function that matched the measured clutter power in a range interval and at a given azimuth to the modeled clutter power. Sea temperature, air pressure, and windspeed were directly used from NWP. Air-sea temperature difference (ASTD) and humidity were identified as the state vector to be found by NWP-only, RFC-ED-only, and the joint method. An ensemble of Hawaii hindcasts and a range of possible ASTD values were considered through four examples. It was shown that NWP and RFC had different sensitivities to ASTD and RH under varying stability conditions. Thus, using a joint method enabled us to reduce significantly the overall uncertainties in these parameters. Likewise, the real-time RFC updates were able to mitigate the error in atmospheric parameters created under a hypothetical case when the true environment deviated from the initial COAMPS estimates.

Acknowledgment

The contents of Chapter 5 are submitted to *J. Appl. Meteorol.* for publication as: A. Karimian, C. Yardim, T. Haack, P. Gerstoft, W. .S. Hodgkiss, Ted Rogers, “Towards assimilation of atmospheric surface layer using weather prediction and radar clutter observations”.

Chapter 6

Conclusion and Future Research

RFC is an approach for estimating the refractivity structure of a maritime environment based on observed radar clutter power. Marine ducts and their mathematical models have been discussed, and a framework for casting an inverse problem was presented. An inversion consists of a forward model to map the candidate refractivity profiles to the observation domain, and a similarity measure to find the best profile [18]. A radar clutter model was presented that was based on all propagating grazing angles at each range and the amount of power that they carry [26]. The performance of this model was tested on simulated clutter powers and measured radar data [27]. Finally, a framework was suggested for joint inversion of radar clutter observations and a numerical weather prediction (NWP) ensemble in evaporation ducting conditions [19]. However, there are issues that need to be addressed in future studies.

Bilinear and trilinear approximations to surface-based ducts are not representative of the duct structure in some situations, and their performance worsens as the operational frequency increases [18]. There have been attempts to overcome this problem by suggesting environmental refractivity models that rely on finding basis vectors of the refractivity profile [84]. Models for duct structures are required that are simple (for easy inversion), and at the same time more representative of the true wave propagation, especially if RFC is to be implemented at frequencies higher than 3 GHz.

Sea surface reflectivity models that currently are used in the radar community, e.g. the GIT model [112], do not represent well the sea reflections at very low grazing angles. Thus, remote sensing problems require more realistic models of the sea surface reflectivity at these angles ($< 1^\circ$).

Fusion of weather prediction algorithms with RFC inversions can greatly increase the performance of both. An example is in costal regions when the warm flow of air over the sea forms a rising surface duct that influences radar propagation. NWP systems have undergone substantial development in the last decade. There currently exist capabilities to extract 48 h weather forecasts [135]. These forecasts are used now to predict the radar performance [136]. An improvement of this work was presented in this dissertation that used RFC inversions alongside with weather forecasts.

Our framework for integration of radar observations with an NWP ensemble was focused on estimation of the atmospheric bulk parameters at a certain height (10 m) in evaporation ducting conditions [19]. While evaporation ducts are the most common ocean ducting phenomenon, a more general framework can be developed for integration of an NWP ensemble with radar observations that can work in surface-based and elevated ducting conditions as well. However, our approach was based on the Monin-Obukhov (MO) similarity theory which links bulk parameters to a full vertical atmospheric surface layer profile in evaporation ducting conditions. Similar theories need to be developed first in other atmospheric conditions. An alternative solution is to implement approaches that do not depend on the MO theory. Our research opened the way for a full data assimilation framework, where radar observations can be assimilated into the initial field that is used for NWP.

Bibliography

[1] M. I. Skolnik, *Radar handbook*, 3rd ed. New York: McGraw-Hill, 2008.

[2] G. D. Thayer, "An improved equation for the radio refractive index of air," *Radio Sci.*, vol. 9, no. 10, pp. 803–807, Oct. 1974, doi:10.1029/RS009i010p00803.

[3] M. Bevis, S. Businger, and S. Chiswell, "GPS meteorology: mapping zenith wet delays onto precipitable water," *J. Appl. Meteor.*, vol. 33, pp. 379–386, 1994, doi:10.1175/1520-0450(1994)033<0379:GMMZWD>2.0.CO;2.

[4] T. Foken, "50 years of the Monin–Obukhov similarity theory," *Bound.-Layer Meteor.*, vol. 119, no. 3, pp. 431–447, June 2006.

[5] J. H. Richter, "Structure, variability, and sensing of the coastal environments," in *AGARD SPP Symposium on Propagation Assessment in Coastal Environments*. NATO AGARD, Neuilly-sur-Seine, France, Feb. 1995, pp. 1.1–7.14.

[6] L. T. Rogers, "Likelihood estimation of tropospheric duct parameters from horizontal propagation measurements," *Radio Sci.*, vol. 32, pp. 79–92, 1997, doi:10.1029/96RS02904.

[7] T. Haack and S. D. Burk, "Summertime marine refractivity conditions along coastal California," *J. Appl. Meteor.*, vol. 40, pp. 673–687, 2001, doi:10.1175/1520-0450(2001)040<0673:SMRCAC>2.0.CO;2.

[8] H. V. Hitney, "Remote sensing of refractivity structure by direct measurements at UHF," in *AGARD Conf. Proc.*, Cesme, Turkey, Feb. 1992, pp. 1.1–1.5.

[9] K. D. Anderson, "Tropospheric refractivity profiles inferred from low elevation angle measurements of Global Positioning System (GPS) signals," in *AGARD Conf. Proc.*, Bremerhaven, Germany, Sep. 1994, pp. 2.1–2.7.

[10] A. R. Lowry, C. Rocken, S. V. Sokolovsky, and K. D. Anderson, "Vertical profiling of atmospheric refractivity from ground-based GPS," *Radio Sci.*, vol. 37, pp. 1041–1059, 2002, doi:10.1029/2000RS002565.

[11] L. Lin, Z. Zhao, Y. Zhang, and Q. Zhu, “Tropospheric refractivity profiling based on refractivity profile model using single ground-based global positioning system,” *Radar Sonar Navigation, IET*, vol. 5, no. 1, pp. 7–11, Jan. 2011, doi:10.1049/iet-rsn.2009.0167.

[12] L. T. Rogers, C. P. Hattan, and J. K. Stapleton, “Estimating evaporation duct heights from radar sea echo,” *Radio Sci.*, vol. 35, no. 4, pp. 955–966, 2000, doi:10.1029/1999RS002275.

[13] P. Gerstoft, L. T. Rogers, J. L. Krolik, and W. S. Hodgkiss, “Inversion for refractivity parameters from radar sea clutter,” *Radio Sci.*, vol. 38, no. 3, pp. 1–22, Apr. 2003, doi:10.1029/2002RS002640.

[14] S. Vasudevan, R. Anderson, S. Kraut, P. Gerstoft, L. T. Rogers, and J. L. Krolik, “Recursive Bayesian electromagnetic refractivity estimation from radar sea clutter,” *Radio Sci.*, vol. 42, RS2014, 2007, doi:10.1029/2005RS003423.

[15] C. Yardim, P. Gerstoft, and W. S. Hodgkiss, “Tracking refractivity from clutter using Kalman and particle filters,” *IEEE Trans. Antennas Propagat.*, vol. 56, no. 4, pp. 1058–1070, 2008, doi:10.1109/TAP.2008.919205.

[16] W. L. Patterson, “User’s manual for Advanced Refractive Effect Prediction System, 3.4 ed,” Atmos. Propag. Branch Space and Nav. Warfare Syst. Cent., San Diego, CA, Tech. Rep., 2005.

[17] C. Yardim, P. Gerstoft, and W. S. Hodgkiss, “Sensitivity analysis and performance estimation of refractivity from clutter technique,” *Radio Sci.*, vol. 44, RS1008, 2009, doi:10.1029/2008RS003897.

[18] A. Karimian, C. Yardim, P. Gerstoft, W. S. Hodgkiss, and A. E. Barrios, “Refractivity estimation from sea clutter: An invited review,” *Radio Sci.*, vol. 46, RS6013, 2011, doi:10.1029/2011RS004818.

[19] A. Karimian, C. Yardim, T. Haack, P. Gerstoft, W. S. Hodgkiss, and T. Rogers, “Towards assimilation of atmospheric surface layer using weather prediction and radar clutter observations,” *J. Appl. Meteorol.* , submitted 2012.

[20] A. E. Barrios, “Advanced propagation model (APM) computer software configuration item (CSCI),” Space and Naval Warfare Systems Center, TD 3145, August 2002.

[21] G. D. Dockery and J. R. Kuttler, “An improved impedance-boundary algorithm for Fourier split-step solution of the parabolic wave equation,” *IEEE Trans. Antennas Propagat.*, vol. 44, no. 12, pp. 1592–1599, 1996, doi:10.1109/8.546245.

[22] M. Levy, *Parabolic equation methods for electromagnetic wave propagation*. London: The Institution of Electrical Engineers, 2000.

[23] G. D. Dockery, "Modeling electromagnetic wave propagation in the troposphere using the parabolic equation," *IEEE Trans. Antennas Propagat.*, vol. 36, no. 10, pp. 1464–1470, 1988, doi:10.1109/8.8634.

[24] R. O. Schmidt, "Multiple emitter location and signal parameter estimation," *IEEE Trans. Antennas Propagat.*, vol. 34, no. 3, pp. 276–280, 1986, doi:10.1109/TAP.1986.1143830.

[25] G. D. Dockery, R. S. Awadallah, D. E. Freund, J. Z. Gehman, and M. H. Newkirk, "An overview of recent advances for the TEMPER radar propagation model," in *IEEE Radar Conference*, April 2007, pp. 896–905.

[26] A. Karimian, C. Yardim, P. Gerstoft, W. S. Hodgkiss, and A. E. Barrios, "Multiple grazing angle sea clutter modeling," *IEEE Trans. Antennas Propagat.*, vol. 60, no. 9, pp. 4408–4417, 2012.

[27] ——, "Estimation of refractivity using a multiple angle clutter model," *Radio Sci.*, vol. 47, RS0M07, 2012.

[28] F. Fabry, C. Frush, I. Zawadzki, and A. Kilambi, "On the extraction of near-surface index of refraction using radar phase measurements from ground targets," *J. Atmos. Oceanic Technol.*, vol. 14, pp. 978–987, 1997.

[29] T. M. Weckwerth, C. R. Petter, F. Fabry, S. J. Park, M. A. LeMone, and J. W. Wilson, "Radar refractivity retrieval: Validation and application to short–term forcasting," *J. Appl. Meteor.*, vol. 44, pp. 285–300, 2005, doi:10.1175/JAM-2204.1.

[30] R. D. Roberts, E. Nelson, J. W. Wilson, N. Rehak, J. Sun, S. Ellis, T. Weckwerth, F. Fabry, P. Kennedy, J. Fritz, V. Chandrasekar, S. Reising, S. Padamanabhan, J. Braun, T. Crum, L. Mooney, and R. Palmer, "REFRACTT 2006: Real time retrieval of high-resolution, low-level moisture fields from operational NEXRAD and research radars," *Bull. Amer. Meteor. Soc.*, vol. 89, no. 10, pp. 1535–1538, Oct. 2008.

[31] J. W. Wilson and R. D. Roberts, "Summary of convective storm initiation and evolution during IHOP: Observational and modeling perspective," *Mon. Wea. Rev.*, vol. 134, no. 1, pp. 23–47, 2006, doi:10.1175/MWR3069.1.

[32] R. M. Wakimoto and M. H. Murphy, "Analysis of a dryline during IHOP: implications for convection initiation," *Mon. Wea. Rev.*, vol. 137, no. 3, pp. 912–936, 2009, doi:10.1175/2008MWR2584.1.

[33] R. M. Hodur, "The naval research laboratory's coupled ocean-atmosphere mesoscale prediction system (COAMPS)," *Mon. Wea. Rev.*, vol. 125, no. 7, pp. 1414–1430, 1997.

[34] S. D. Burk, T. Haack, L. T. Rogers, and L. J. Wagner, "Island wake dynamics and wake influence on the evaporation duct and radar propagation," *J. Appl. Meteor.*, vol. 42, pp. 342–367, 2003.

[35] T. Haack, C. Wang, S. Garrett, A. Glazer, J. Mailhot, and R. Marshall, "Mesoscale modeling of boundary layer refractivity and atmospheric ducting," *J. Appl. Meteor. Climetol.*, vol. 49, pp. 2437–2457, 2010.

[36] C. Wang, D. Wilson, T. Haack, P. Clark, H. Lean, and R. Marshall, "Effects of initial and boundary conditions of mesoscale models on simulated atmospheric refractivity," *J. Appl. Meteor. Climetol.*, vol. 51, pp. 115–131, 2012.

[37] C. Yardim, P. Gerstoft, and W. S. Hodgkiss, "Statistical maritime radar duct estimation using a hybrid genetic algorithm—Markov chain Monte Carlo method," *Radio Sci.*, vol. 42, RS3014, 2007, doi:10.1029/2006RS003561.

[38] K. D. Anderson, "Radar detection of low-altitude targets in a maritime environment," *IEEE Trans. Antennas Propagat.*, vol. 43, no. 6, pp. 609–613, 1995, doi:10.1109/8.387177.

[39] R. J. Doviak and D. S. Zrnić, *Doppler radar and weather observations*, 2nd ed. Academy Press, 1993, p. 562.

[40] S. Park and F. Fabry, "Estimation of near-ground propagation conditions using radar ground echo coverage," *J. Atmos. Oceanic Technol.*, vol. 28, pp. 165–180, Feb. 2011, doi:10.1175/2010JTECHA1500.1.

[41] W. Patterson, "Ducting climatology summary," SPAWAR Sys. Cent., San Diego, Calif., Tech. Rep., 1992.

[42] J. P. Reilly and G. D. Dockery, "Influence of evaporation ducts on radar sea return," in *IEE Proc. Radar and Signal Processing*, vol. 137, 1990, pp. 80–88.

[43] R. A. Pappert, R. A. Paulus, and F. D. Tappert, "Sea echo in tropospheric ducting environments," *Radio Sci.*, vol. 27, no. 2, pp. 189–209, 1992, doi:10.1029/91RS02962.

[44] J. R. Rowland, G. C. Konstanzer, M. R. Neves, R. E. Miller, J. H. Meyer, and J. R. Rottier, "Seawasp: refractivity characterization using shipboard sensors," in *Battlespace Atmospheric Conferene*, RDT&E Div., Nav. Command Control and Ocean Surv. Cent., San Diego, Calif., Dec. 1996, pp. 155–164.

[45] R. A. Helvey, "Radiosonde errors and spurious surface-based ducts," *Proc. IEE F*, vol. 130, no. 7, pp. 643–648, 1983.

[46] S. Mentes and Z. Kaymaz, "Investigation of surface duct conditions over Istanbul, Turkey," *J. Appl. Meteor. Climetol.*, vol. 46, pp. 318–337, 2007, doi:10.1175/JAM2452.1.

[47] H. Jeske, "State and limits of prediction methods for radar wave propagation conditions over the sea," in *Modern topics in Microwave Propagation and Air-Sea Interaction*, A. Zancla, Ed. D. Reidel Publishing, 1973, pp. 130–148.

[48] C. W. Fairall, E. F. Bradley, D. P. Rogers, J. B. Edson, and G. S. Young, "Bulk parametrization of air-sea fluxes for tropical ocean-global atmosphere coupled-ocean atmosphere response experiment," *J. Geophys. Res.*, vol. 101, no. C2, pp. 3747–3764, 1996, doi:10.1029/95JC03205.

[49] P. A. Frederickson, K. L. Davidson, C. R. Zeisse, and C. S. Bendall, "Estimating the refractive index structure parameter (C_n^2) over the ocean using bulk methods." *J. Appl. Meteor.*, vol. 39, pp. 1770–1783, 2000, doi: 10.1175/1520-0450-39.10.1770.

[50] D. Boyer, G. Gentry, J. Stapleton, and J. Cook, "Using remote refractivity sensing to predict tropospheric refractivity from measurements of propagation," in *Proc. AGARD SPP Symp. Remote Sensing: Valuable Source Inform.*, Toulouse, France, Apr. 1996, pp. 16.1–16.13.

[51] J. L. Krolik and J. Tabrikian, "Tropospheric refractivity estimation using radar clutter from the sea surface," in *Proc. Battlespace Atmospheric Conference, SSC-SD*, San Diego, CA, March 1997, pp. 635–642.

[52] J. Tabrikian and J. Krolik, "Theoretical performance limits on tropospheric refractivity estimation using point–to–point microwave measurements," *IEEE Trans. Antennas Propagat.*, vol. 47, no. 11, pp. 1727–1734, 1999, doi:10.1109/8.814953.

[53] A. G. Von Engeln, G. Nedoluha, and J. Teixeira, "An analysis of the frequency and distribution of ducting events in simulated radio occultation measurements based on ECMWF fields," *J. Geophys. Res.*, vol. 108, no. D21, 4669, 2003, doi:10.1029/2002JD003170.

[54] U. Wandinger, "Raman Lidar," in *Lidar*, ser. Springer Series in Optical Sciences, C. Weitkamp, Ed. Springer Berlin / Heidelberg, 2005, vol. 102, pp. 241–271.

[55] A. Willitsford and C. R. Philbrick, "Lidar description of the evaporation duct in ocean environments," in *SPIE*, vol. 5885, Bellingham, WA, September 2005, pp. 140–147.

[56] R. Douvenot, V. Fabbro, P. Gerstoft, C. Bourlier, and J. Saillard, "Real time refractivity from clutter using a best fit approach improved with physical information," *Radio Sci.*, vol. 45, RS1007, Feb. 2010, doi:10.1029/2009RS004137.

[57] A. E. Barrios, "Estimation of surface-based duct parameters from surface clutter using a ray trace approach," *Radio Sci.*, vol. 39, RS6013, 2004, doi:10.1029/2003RS002930.

[58] F. B. Jensen, W. A. Kuperman, M. B. Porter, and H. Schmidt, *Computational ocean acoustics*. Springer London, Limited, 2011.

[59] S. E. Dosso and J. Dettmer, "Bayesian matched-field geoacoustic inversion," *Inverse Problems*, vol. 27(5), 055009, 2011, doi:10.1088/0266-5611/27/5/055009.

[60] C. Yardim, Z. H. Michalopoulou, and P. Gerstoft, "An overview of sequential Bayesian filtering in ocean acoustics," *IEEE J. Ocean. Eng.*, vol. 36, no. 1, pp. 71–89, Jan. 2011, doi:10.1109/JOE.2010.2098810.

[61] D. E. Kerr, *Propagation of short radio waves*. McGraw-Hill, 1951.

[62] E. E. Gossard, "Clear weather meteorological effects on propagation at frequencies above 1 GHz," *Radio Sci.*, vol. 16, no. 5, pp. 589–608, Sep. 1981, doi:10.1029/RS016i005p00589.

[63] H. Dougherty and B. A. Hart, "Recent progress in duct propagation predictions," *IEEE Trans. Antennas Propagat.*, vol. 27, no. 4, pp. 542–548, 1979, doi:10.1109/TAP.1979.1142130.

[64] L. T. Rogers, "Effects of the variability of atmospheric refractivity on propagation estimates," *IEEE Trans. Antennas Propagat.*, vol. 44, no. 4, pp. 460–465, 1996, doi:10.1109/8.489297.

[65] C. L. Pekeris, "Accuracy of the earth flattening approximation in the theory of microwave propagation," *Phys. Rev.*, vol. 70, no. 7-8, pp. 518–522, Oct 1946, doi:10.1103/PhysRev.70.518.

[66] M. Katzin, R. W. Bauchman, and W. Binnian, "3- and 9-centimeter propagation in low ocean ducts," *Proc. IRE*, vol. 35, pp. 891–905, 1947.

[67] W. T. Liu, K. B. Katsaros, and J. A. Businger, "Bulk parameterization of air-sea exchanges of heat and water vapor including the molecular constraints at the interface," *J. Atmos. Sci.*, vol. 36, pp. 1722–1735, 1979, doi:10.1175/1520-0469(1979)036<1722:BPOASE>2.0.CO;2.

[68] R. A. Paulus, "Practical applications of an evaporation duct model," *Radio Sci.*, vol. 20, pp. 887–896, 1985, doi: 10.1029/RS020i004p00887.

[69] S. M. Babin, G. A. Young, and J. A. Carton, “A new model of the oceanic evaporation duct,” *J. Appl. Meteor.*, vol. 36, no. 3, pp. 193–204, 1997, doi:10.1175/1520-0450(1997)036<0193:ANMOTO>2.0.CO;2.

[70] G. L. Greenaert, “Notes and correspondence on the evaporation duct for inhomogeneous conditions in coastal regions,” *J. Appl. Meteor. Climetol.*, vol. 46, no. 4, pp. 538–543, Apr. 2007.

[71] I. M. Brooks, A. K. Goroch, and D. P. Rogers, “Observations of strong surface radar ducts over the Persian Gulf,” *J. Appl. Meteor.*, vol. 38, no. 9, pp. 1293–1310, Sep. 1999, doi:10.1175/1520-0450(1999)038<1293:OOSSRD>2.0.CO;2.

[72] P. A. Frederickson, K. L. Davidson, and A. K. Goroch, “Operational bulk evaporation duct model for MORIAH, ver. 1.2,” Nav. Postgrad. Sch., Monterey, Calif., Tech. Rep. NPS/MR-2000-002, 5 May 2000.

[73] J. P. Zhang, Z. S. Wu, Q. L. Zhu, and B. Wang, “A four-parameter M-profile model for the evaporation duct estimation from radar clutter,” *Progress In Electromagnetics Research*, vol. 114, pp. 353–368, 2011.

[74] R. A. Paulus, “Evaporation duct effects on sea clutter,” *Radio Sci.*, vol. 38, no. 11, pp. 1765–1771, 1990, doi:10.1109/8.102737.

[75] H. V. Hitney, “Refractive effects from VHF to EHF. Part A: Propagation mechanisms,” in *AGARD Lecture Series*, vol. LS-196, Sep. 1994, pp. 4A1–4A13.

[76] P. Gerstoft, D. F. Gingras, L. T. Rogers, and W. S. Hodgkiss, “Estimation of radio refractivity structure using matched–field array processing,” *IEEE Trans. Antennas Propagat.*, vol. 48, no. 3, pp. 345–356, Mar. 2000, doi:10.1109/8.841895.

[77] L. T. Rogers and R. A. Paulus, “Measured performance of evaporation duct models,” Naval Command, Command and Ocean Surviellance Center RDTE Div., Tech. Rep. 2989, Dec. 1996.

[78] L. T. Rogers, M. Jablecki, and P. Gerstoft, “Posterior distribution of a statistic propagation loss inferred from radar sea clutter,” *Radio Sci.*, vol. 40, RS6005, 2005, doi:10.1029/2004RS003112.

[79] P. Gerstoft, W. S. Hodgkiss, L. T. Rogers, and M. Jablecki, “Probability distribution of low-altitude propagation loss from radar sea clutter data,” *Radio Sci.*, vol. 39, RS6006, 2004, doi:10.1029/2004/RS003077.

[80] A. E. Barrios, “A terrain parabolic equation model for propagation in the troposphere,” *IEEE Trans. Antennas Propagat.*, vol. 42, no. 1, pp. 90–98, 1994, doi:10.1109/8.272306.

[81] E. L. Miller and A. S. Willsky, "A multiscale, statistically based inversion scheme for linearized inverse scattering problems," *IEEE Trans. Geosci. Remote Sens.*, vol. 34, no. 2, pp. 346–357, Mar. 1996, doi:10.1109/36.485112.

[82] ——, "Wavelet-based methods for the nonlinear inverse scattering problem using the extended Born approximation," *Radio Sci.*, vol. 31, no. 1, pp. 51–65, Jan.–Feb. 1996, doi:10.1029/95RS03130.

[83] Y. Hua and W. Liu, "Generalized Karhunen-Loeve transform," *IEEE Signal Process. Lett.*, vol. 5, no. 6, pp. 141–142, 1998.

[84] S. Kraut, R. Anderson, and J. Krolik, "A generalized Karhunen-Loeve basis for efficient estimation of tropospheric refractivity using radar clutter," *IEEE Trans. Sig. Proc.*, vol. 52, no. 1, pp. 48–59, Jan. 2004, doi:10.1109/TSP.2003.820297.

[85] N. Guinard, J. Ransone, D. Randall, C. Purves, and P. Watkins, "Propagation through an elevated duct: Tradewinds III," *IEEE Trans. Antennas Propagat.*, vol. 12, no. 4, pp. 479–490, Jul. 1964, doi:10.1109/TAP.1964.1138252.

[86] A. Kukushkin, *Radio wave propagation in the marine boundary layer*. Wiley, 2004.

[87] G. D. Dockery, "Method for modeling sea surface clutter in complicated propagation environments," in *IEE Proc. Radar and Signal Processing*, vol. 137, 1990, pp. 73–79.

[88] C. Yardim, P. Gerstoft, and W. S. Hodgkiss, "Estimation of radio refractivity from radar clutter using Bayesian Monte Carlo analysis," *IEEE Trans. Antennas Propagat.*, vol. 54, no. 4, pp. 1318–1327, 2006, doi: 10.1109/TAP.2006.872673.

[89] B. Wang, Z. S. Wu, A. Zhao, and H. G. Wang, "Retrieving evaporation duct heights from radar sea clutter using particle swarm optimization," *Progress In Electromagnetics Research*, vol. 9, pp. 79–91, 2009, doi:10.2528/PIERM09090403.

[90] R. Douvenot and V. Fabbro, "On the knowledge of radar coverage at sea using real time refractivity from clutter," *IET Radar Sonar Navig.*, vol. 4, no. 2, pp. 293–301, doi:10.1049/iet–rsn.2009.0073, 2010.

[91] X. F. Zhao, S. X. Huang, and H. D. Du, "Theoretical analysis and numerical experiments of variational adjoint approach for refractivity estimation," *Radio Sci.*, vol. 46, RS1006, Jan. 2011, doi:10.1029/2010RS004417.

[92] L. V. Blake, *Radar Range Performance Analysis*. Lexington, MA: Lexington Books, 1980.

[93] H. V. Hitney and J. H. Richter, "Integrated Refractive Effects Prediction System (IREPS)," *Nav. Eng. J.*, vol. 88, no. 2, pp. 257–262, 1976.

[94] K. G. Budden, *The Wave-Guide Mode Theory of Wave Propagation*. Englewood Cliffs, NJ: Prentice-Hall, 1961.

[95] M. A. Leontovich and V. A. Fock, "Solution of the problem of electromagnetic wave propagation along the earth's surface by the method of parabolic equation," *Acad. Sci. USSR J. Phys.*, vol. 10, pp. 13–23, 1946.

[96] R. H. Hardin and F. D. Tappert, "Application of the split-step Fourier method to the numerical solution of nonlinear and variable coefficient wave equations," *SIAM Rev. 15*, vol. 423, 1973.

[97] H. W. Ko, J. W. Sari, and J. P. Skura, "Anomalous microwave propagation through atmospheric ducts," Johns Hopkins APL Tech. Dig. 4(2), 12–26, 1983.

[98] J. P. Skura, C. E. Schemm, H. W. Ko, and L. P. Manzi, "Radar coverage predictions through time- and range-dependent refractive atmosphere with planetary boundary layer and electromagnetic parabolic equation models," in *IEEE Radar Conference*, May 1990, pp. 370–378.

[99] M. D. Feit and J. A. Fleck, "Light propagation in graded-index fibers," *Appl. Opt.*, vol. 17, pp. 3990–3998, 1978, doi:10.1364/AO.17.003990.

[100] D. J. Thomson and N. R. Chapman, "A wide-angle split-step algorithm for the parabolic equation," *J. Acoust. Soc. Am.*, vol. 74, no. 6, pp. 1848–1854, Dec. 1983, doi:10.1121/1.390272.

[101] J. R. Kuttler, "Differences between the narrow-angle and wide-angle propagators in the split-step Fourier solution of the parabolic wave equation," *IEEE Trans. Antennas Propagat.*, vol. 47, no. 7, pp. 1131–1140, July 1999, doi: 10.1109/8.785743.

[102] J. R. Kuttler and R. Janaswamy, "Improved Fourier transform methods for solving the parabolic wave equation," *Radio Sci.*, vol. 37, no. 2, pp. 1021–1031, 2002, doi: 10.1029/2001RS002488.

[103] A. E. Barrios, "Parabolic equation modeling in horizontally inhomogeneous environments," *IEEE Trans. Antennas Propagat.*, vol. 40, no. 7, pp. 791–797, July 1992, doi:10.1109/8.155744.

[104] ——, "Considerations in the development of the advanced propagation model (APM) for U.S. Navy applications," in *International Conf. on Radar*, Adelaide, Australia, Sep. 2003.

[105] A. R. Miller, R. M. Brown, and E. Vegh, "New derivation for the rough surface reflection coefficient and for the distribution of the sea-wave elevations," *Proc. Inst. Elect. Eng.*, vol. 131, no. 2, pt.H, pp. 114–116, Apr. 1984, doi:10.1049/ip-h-1.1984.0022.

[106] O. M. Phillips, "Spectral and statistical properties of the equilibrium range in wind-generated gravity waves," *J. Flui. Mech.*, vol. 156, pp. 505–531, 1985, doi:10.1017/S0022112085002221.

[107] ITU reports, "Report 1008-1, Reflection from the surface of the Earth," in *Recommendations and reports of the CCIR, Propagation in nonionized media*, vol. 5, 1990. [Online]. Available: http://www.itu.int/pub/R-REP-P.1008-1-1990

[108] R. Janaswamy, "Radio wave propagation over a nonconstant immittance plane," *Radio Sci.*, vol. 36, pp. 387–405, May-June 2001, doi:10.1029/2000RS002338.

[109] G. C. Konstanzer, J. Z. Gehman, M. H. Newkirk, and G. D. Dockery, "Calculation of the surface incident field using TEMPER for land and sea clutter modeling," *Proc. on Low Grazing Angle Clutter: Its Characterization, Measurement and Application, RTO-MP-60*, pp. 14–1–14–2, 2000.

[110] F. E. Nathanson, J. P. Reilly, and M. N. Cohen, *Radar design principles: Signal processing and the environment*, 2nd ed. McGraw-Hill, 1991.

[111] D. K. Barton, *Modern Radar System Analysis*. Artech House, 1988.

[112] M. Horst, F. Dyer, and M. Tuley, "Radar sea clutter model," in *Int. IEEE AP/S URSI Symposium*, vol. Proc. Part 2 (A80-15812 04-32). London, England: London Institute of electrical engineers, Nov. 1978, pp. 6–10.

[113] C. Fletcher, "Clutter subroutine," Technology Service Corp., Silver Spring, MD, USA, Memorandum TSC-W84-01/cad, Aug 1978.

[114] H. Sittrop, "Characteristics of clutter and target at X- and Ku- band," in *AGARD Conf. Proc.*, ser. New Techniques and Systems in Radar, no. 197, Hague, Netherlands, June 1977, pp. 28.1–28.27.

[115] V. Gregers-Hansen and R. Mital, "An empirical sea clutter model for low grazing angles," in *IEEE Radar Conference*. Pasadena, CA, May 2009, pp. 1–5.

[116] R. Douvenot, V. Fabbro, P. Gerstoft, C. Bourlier, and J. Saillard, "A duct mapping method using least square support vector machines," *Radio Sci.*, vol. 53, RS6005, 2008, doi:10.1029/2008RS003842.

[117] J. P. Zhang, Z. S. Wu, and B. Wang, "An adaptive objective function for evaporation duct estimation from radar sea echo," *Chin. Phys. Lett.*, vol. 28, no. 3, 034301, 2011, doi:10.1088/0256-307X/28/3/034301.

[118] D. F. Gingras, P. Gerstoft, and N. L. Gerr, "Electromagnetic matched field processing: basic concepts and tropospheric simulations," *IEEE Trans. Antennas Propagat.*, vol. 42, no. 10, pp. 1536–1545, Oct. 1997, doi: 10.1109/8.633863.

[119] L. R. Rabiner, "A tutorial on hidden Markov models and selected applications in speech recognition," *Proc. IEEE*, vol. 77, no. 2, pp. 257–286, Feb. 1989, doi:10.1109/5.18626.

[120] S. M. Kay, *Fundamentals of statistical signal processing, volume I: Estimation theory*. Englewood Cliffs, NJ: Prentice Hall, 1993.

[121] D. J. C. MacKay, *Information Theory, Inference and Learning Algorithms*. Cambridge, United Kingdom: Cambridge University Press, 2003.

[122] J. J. K. Ó Ruanaidh and W. J. Fitzgerald, *Numerical Bayesian Methods Applied to Signal Processing*, ser. Statistics and Computing Series. New York: Springer–Verlag, 1996.

[123] N. Metropolis, A. W. Rosenbluth, M. N. Rosenbluth, A. H. Teller, and E. Teller, "Equation of state calculations by fast computing machines," *J. of Chemical Physics*, vol. 21, pp. 1087–1092, 1953, doi:10.1063/1.1699114.

[124] S. Geman and D. Geman, "Stochastic relaxation, Gibbs distributions, and the Bayesian restoration of images," *IEEE Trans. Pattern Anal. Machine Intell.*, vol. 6, pp. 721–741, 1984, doi:10.1080/02664769300000058.

[125] M. Sambridge, "Geophysical inversion with a neighborhood algorithm - I. searching a parameter space," *Geophys. J. Int.*, vol. 138, pp. 479–494, 1999.

[126] ——, "Geophysical inversion with a neighborhood algorithm - II. appraising the ensemble," *Geophys. J. Int.*, vol. 138, pp. 727–746, 1999.

[127] S. Julier, J. Uhlmann, and H. F. Durrant-White, "A new method for nonlinear transformation of means and covariances in filters and estimators," *IEEE Trans. Automat. Control*, vol. 45, pp. 477–482, 2000, doi:10.1109/9.847726.

[128] E. A. Wan and R. van der Merve, "The unscented Kalman filter", in S. Haykin, *Kalman Filtering and Neural Networks*. New York: John Wiley & Sons, 2001.

[129] N. J. Gordon, D. J. Salmond, and A. F. M. Smith, "Novel approach to nonlinear/non-Gaussian Bayesian state estimation," *IEE Proc. F, Radar and Signal Processing*, vol. 140, no. 2, pp. 107–113, 1993, doi:10.1049/ip-f-2.1993.0015.

[130] P. Gerstoft, L. T. Rogers, W. S. Hodgkiss, and L. J. Wagner, "Refractivity estimation using multiple elevation angles," *IEEE J. Ocean. Eng.*, vol. 28, pp. 513–525, July 2003, doi:10.1109/JOE.2003.816680.

[131] P. J. Huber, "Robust regression: Asymptotics, conjectures, and Monte Carlo," *Ann. Statist.*, vol. 1, no. 5, pp. 799–821, 1973.

[132] A. Guitton and W. W. Symes, "Robust inversion of seismic data using the Huber norm," *Geophysics*, vol. 68, no. 4, pp. 1310–1319, July 2003, doi:10.1190/1.1598124.

[133] T. Ha, W. Chung, and C. Shin, "Waveform inversion using a back propagation algorithm and a Huber function norm," *Geophysics*, vol. 74, no. 3, pp. R15–R24, 2009.

[134] X. F. Zhao and S. X. Huang, "Refractivity estimations from an angle of arrival spectrum," *Chin. Phys. B*, vol. 20, no. 2, 029201, 2011, doi:10.1088/1674-1056/20/2/029201.

[135] R. E. Marshall, W. D. Thornton, G. LeFurjah, and S. Casey, "Modeling and simulation of notional future radar in non-standard propagation environments facilitated by mesoscale numerical weather prediction modeling," *Naval Engineers Journal*, vol. 120, no. 4, pp. 55–66, 2008, doi:10.1111/j.1559-3584.2008.00165.x.

[136] G. LeFurjah, R. Marshall, T. Casey, T. Haack, and D. De Forest Boyer, "Synthesis of mesoscale numerical weather prediction and empirical site-specific radar clutter models," *IET Radar Sonar Navig.*, vol. 4, no. 6, pp. 747–754, 2010.

[137] S. U. Pillai and B. H. Kwon, "Forward/backward spatial smoothing techniques for coherent signal identification," *IEEE Trans. Acoust Speech Signal Process*, vol. 37, no. 1, pp. 8–15, Jan. 1989, doi:10.1109/29.17496.

[138] J. P. Reilly and G. D. Dockery, "Calculation of radar sea return with consideration of propagation conditions," NATO, AAW Technical Report NNW-88-141, December 1988.

[139] H. L. VanTrees, *Optimum array processing*. New York: John Wiley and Sons, 2002.

[140] C. G. Someda, *Electromagnetic Waves*, 2nd ed. Taylor and Francis Group, 2006.

[141] D. E. Barrick, "Grazing behavior of scatter and propagation above any rough surface," *IEEE Trans. Antennas Propagat.*, vol. 46, no. 1, pp. 73–83, 1998, doi: 10.1109/8.655453.

[142] M. Dzieciuch, P. Worcester, and W. Munk, "Turning point filters: analysis of sound propagation on a gyre-scale," *J. Acoust. Soc. Am.*, vol. 110, no. 1, pp. 135–149, 2001, doi:10.1121/1.1377869.

[143] H. M. Lee and Y. Y. Han, "M-layer: NPS version," *IEEE Trans. Magnetics*, vol. 29, no. 2, pp. 1363–1367, 1993.

[144] M. W. Long, *Radar reflectivity of land and sea*, 3rd ed. Norwood, Mass.: Artech House, 2000.

[145] K. D. Ward, R. J. A. Tough, and S. Watts, *Sea clutter: scattering, the K distribution and radar performance*. London: Inst. of Eng. and Technol., 2005, vol. 2005.

[146] T. T. Warner, *Numerical weather and climate prediction*. Cambridge University press, 2011.

[147] X. Zhao and S. Huang, "Estimation of atmospheric duct structure using radar sea clutter," *J. Atmos. Sci.*, vol. 69, pp. 2808–2818, Sep. 2012.

[148] P. Frederickson, "Software design description for the Navy Atmospheric Vertical Surface Layer Model (NAVSLaM)," Naval Oceanographic Office, Tech. Rep., 2010.

[149] C. W. Fairall, E. F. Bradley, J. E. Hare, A. A. Grachev, and J. B. Edson, "Bulk parametrization of air-sea fluxes: Updates and verification for the COARE algorithm," *J. Atmos. Ocean. Technol.*, vol. 16, pp. 571–591, 2003.

[150] A. E. Barrios, K. Anderson, and G. Lindem, "Low altitude propagation effects–a validation study of the Advanced Propagation Model (APM) for mobile radio applications," *IEEE Trans. Antennas Propagat.*, vol. 54, no. 10, pp. 2869–2877, Oct. 2006, doi:10.1109/TAP.2006.882163.

[151] M. Dodgett, "An atmospheric sensitivity and validation study of the variable terrain radio parabolic equation model," Master's thesis, Air Force Institute of Technology, 1997.

[152] T. N. Palmer, "Extended-range atmospheric prediction and the lorenz model," *Bull. Amer. Meteor. Soc.*, vol. 74, pp. 49–65, 1993.

[153] A. W. Robertson, U. Lall, S. E. Zebiak, and L. Goddard, "Improved combination of multiple atmospheric GCM ensembles for seasonal prediction," *Mon. Wea. Rev.*, vol. 132, pp. 2732–2744, 2004.

[154] D. B. Stephenson, C. A. S. Coelho, F. J. Doblas-Ryes, and M. Balmaseda, "Forecast assimilation: a unified framework for the combination of multi-model weather and climate predictions," *Tellus*, vol. 57A, pp. 253–264, 2005.

[155] R. M. Hodur, X. Hong, J. D. Doyle, J. Pullen, J. Cummings, P. Martin, and M. A. Rennick, "The Coupled Ocean/ Atmosphere Mesoscale Prediction System (COAMPS)," *Oceanography*, vol. 15, no. 1, pp. 88–98, 2001.

[156] C. H. Bishop and Z. Toth, "Ensemble transformation and adaptive observations," *J. Atmos. Sci.*, vol. 56, pp. 1748–1765, 1999.

[157] J. G. McLay, C. H. Bishop, and C. A. Reynolds, "Evaluation of the ensemble transform analysis perturbation scheme at NRL," *Mon. Wea. Rev.*, vol. 136, pp. 1093–1108, 2008, doi: 10.1175/2007MWR2010.1.

[158] E. Kalnay, *Atmospheric modeling, data assimilation and predictability*. Cambridge University Press, 2003.

[159] W. C. Thacker and O. E. Esenkov, "Assimilating XBT data into HYCOM," *J. Atmos. Ocean. Tech.*, vol. 19, pp. 709–724, 2002.

[160] P. Lermusiaux, J. Xu, C. F. Chen, S. Jan, L. Y. Chiu, and Y. Yang, "Coupled ocean–acoustic prediction of transmission loss in a continental shelfbreak region: Predictive skill, uncertainty quantification, and dynamical sensitivities," *IEEE J. Ocean. Eng.*, vol. 35, no. 4, pp. 895–916, 2011.